

Tightly Focused Spot Shaping and its Applications in Optical Imaging and Trapping

Meng, P.

DOI

[10.4233/uuid:33c7fc94-50cc-4b3f-be18-5439a9e29b43](https://doi.org/10.4233/uuid:33c7fc94-50cc-4b3f-be18-5439a9e29b43)

Publication date

2020

Document Version

Final published version

Citation (APA)

Meng, P. (2020). *Tightly Focused Spot Shaping and its Applications in Optical Imaging and Trapping*. [Dissertation (TU Delft), Delft University of Technology]. <https://doi.org/10.4233/uuid:33c7fc94-50cc-4b3f-be18-5439a9e29b43>

Important note

To cite this publication, please use the final published version (if applicable). Please check the document version above.

Copyright

Other than for strictly personal use, it is not permitted to download, forward or distribute the text or part of it, without the consent of the author(s) and/or copyright holder(s), unless the work is under an open content license such as Creative Commons.

Takedown policy

Please contact us and provide details if you believe this document breaches copyrights. We will remove access to the work immediately and investigate your claim.

Tightly Focused Spot Shaping and its Applications in Optical Imaging and Trapping

Tightly Focused Spot Shaping and its Applications in Optical Imaging and Trapping

Dissertation

ter verkrijging van de graad van doctor
aan de Technische Universiteit Delft,
op gezag van de Rector Magnificus prof.dr.ir. T.H.J.J. van der Hagen,
voorzitter van het College voor Promoties,
in het openbaar te verdedigen op donderdag 1 oktober 2020 om 12:30 uur

door

Peiwen MENG

Master of Engineering in Instrument Science and Technology,
Nanjing Forestry University, Nanjing, China,
geboren te Zhenjiang, China.

Dit proefschrift is goedgekeurd door de

promotor: Prof. dr. H.P. Urbach

promotor: Dr. ir. S.F. Pereira

Samenstelling promotiecommissie:

Rector Magnificus,
Prof. dr. H.P. Urbach,
Dr. ir. S.F. Pereira,

voorzitter
Technische Universiteit Delft
Technische Universiteit Delft

Independent members:

Prof. dr. G. Vdovin,
Prof. dr. W.M.J.M. Coene,
Prof. dr. A.P. Mosk,
Dr. A. Erdmann,

Technische Universiteit Delft
Technische Universiteit Delft
Universiteit Utrecht
Fraunhofer Institute for Integrated Systems
and Device Technology IISB

The work in this dissertation was conducted at Optics Research Group of the Department of Imaging Physics, Faculty of Applied Sciences, Delft University of Technology and the PhD candidate was financially supported by the scholarship from China Scholarship Council (201508320235).



ImPhys



 Optics Research Group

Keywords: super-resolution imaging, pupil engineering, optical trapping, angular momenta, confocal microscopy

Printed by: Ridderprint BV

Front & Back: Art and photonics

Copyright © 2020 by Peiwen Meng

ISBN 978-94-6416-164-9

An electronic version of this dissertation is available at

<http://repository.tudelft.nl/>.

This thesis is dedicated to my dear parents.

Contents

Summary	ix
Samenvatting	xi
1 Introduction	1
1.1 The point spread function	2
1.2 Confocal microscopy	3
1.3 Thesis Structure	4
References	5
2 Theoretical analysis on confocal imaging with radially polarized light	9
2.1 Introduction	10
2.2 Dipole excitation using a focused spot	11
2.2.1 Vectorial Diffraction Integral	11
2.2.2 Focal field of linearly and radially polarized light	13
2.2.3 Focused beam shaping	15
2.3 Dipole imaging with a polarization convertor	16
2.3.1 Imaging without polarization convertor	16
2.3.2 Imaging with polarization convertor	18
2.4 Numerical results and discussions	20
2.5 Conclusion	25
References	26
3 Experimental demonstration of resolution enhancement with modulated radially polarized light	31
3.1 Introduction	32
3.2 Experimental set-up	32
3.2.1 General description	32
3.2.2 Amplitude modulation	33
3.2.3 Polarization convertor	35
3.2.4 Detection	37
3.2.5 LabView program	37
3.3 Experimental results and discussions	37
3.4 Conclusion	42
References	43

4	Super-resolution effect due to a thin dielectric slab for imaging with radially polarized light	47
4.1	Introduction	48
4.2	Axial resolution	48
4.3	Lateral resolution.	52
4.3.1	Evanescence wave and super-resolution.	52
4.3.2	Single dipole model.	55
4.4	Numerical results and discussions	59
4.4.1	Reflection coefficient	59
4.4.2	Near field.	59
4.4.3	Imaging	60
4.5	Experimental validation	62
4.6	Conclusion	63
	References.	64
5	Angular momentum properties of cylindrical vector vortex beams	67
5.1	Introduction	68
5.2	Local SAM of focal field for CVV beams	69
5.2.1	Properties of the symmetrical CVV beams	69
5.2.2	Properties of the asymmetrical CVV beams	75
5.3	Optical force and torque on nanoparticles	82
5.3.1	Expressions for optical force and torque	82
5.3.2	Particle's motion with symmetrical CVV beams	83
5.3.3	Particle's motion with asymmetrical CVV beams	85
5.4	Conclusion	89
	References.	90
6	Conclusion and outlook	95
6.1	Conclusion	95
6.2	Outlook	96
	References.	97
	Acknowledgements	99
A	Derivation of the focal fields of given power with a maximum longitudinal electric component	101
	References.	103
B	LabView program	105
C	Full derivation of the reflective far field	107
	Curriculum Vitæ	111
	List of Publications	113

Summary

The Rayleigh criterion explains the diffraction limit and provides guidance for improving the performance of an imaging system namely by decreasing the wavelength of the illumination and/or increasing the aperture (NA) of the objective lens. If the wavelength and NA are set, is it possible to improve the spatial resolution further? This question motivates the research work of this thesis.

Polarization is an important property of light and it can not be ignored in a tightly focusing system. It is demonstrated both theoretically and experimentally that radially polarized light can produce a sharper focal spot in a high NA focusing system because of the tight longitudinal field component. Based on this, in this thesis, we start our investigation on the unique focusing properties of the radially polarized beam with the vectorial diffraction theory. We show that the amplitude of the focal field can be shaped by engineering the pupil field of the radially polarized beam. The shaped focal spot is smaller than the unmodulated one, which can be used to improve the resolution of optical systems. Here, we consider a confocal scanning imaging system, offering several advantages over conventional widefield microscopy. In the simulation, longitudinal electric dipoles are regarded as the objects to make the full use of the optimized longitudinal component. An experimental proof is also given, showing that higher spatial resolution can be achieved when the modulated radially polarized light is applied in the confocal imaging set-up as compared to the non-modulated case. Radially polarized light can be obtained with a liquid crystal based polarization convertor, starting with a linearly polarized beam. Amplitude modulation of the pupil such as the annular pupil field and the designed pupil field where the amplitude increases gradually with the radius can be realized with a spatial light modulator (SLM).

The substrate is essential for supporting the sample to be imaged. Usually, the material of the substrate is glass. In the near field, when the object interacts with the light field, it may produce evanescent waves which decays very quickly and has little influence on the imaging. However, the evanescent wave carries higher spatial frequency than the propagating wave. A well designed substrate with a thin TiO_2 layer on top can enhance the evanescent wave in the near field. The enhanced field transfers to a propagating wave with the help of the object deposited on the substrate and it can be detected in the far field. The principle can be explained with a dipole model, and simulated using nanospheres. It is demonstrated that the designed structure helps to improve the imaging quality including contrast and resolution. In addition, such sample model can be combined with other imaging techniques, e.g. confocal scanning microscopy, widefield imaging system, etc.

Besides amplitude and polarization, focal fields can also be shaped in phase. Unlike the specific radially or azimuthally polarized vector beam, the cylindrical vector beam is a more general form. The focusing properties and the spin-orbit interac-

tions of cylindrical vector vortex beams in high NA focusing systems are theoretically studied. An absorptive nanosphere can be trapped at the hot-spot of the focused field, even when the field has its axial symmetry broken. The analysis on the influence of parameters such as the initial phase of the vortex beam, the topological charge, or the size and the material of the trapping sphere on the interplay between spin and angular momentum may be helpful for optical trapping, particle transport and super-resolution.

Samenvatting

Het Rayleigh criterium verklaart de diffractielimiet en geeft houvast voor het verbeteren van een beeldvormingssysteem, namelijk door de golflengte van de belichting te verkleinen, en/of de apertuur (NA) van het objectief te vergroten. Als de golflengte en NA vast staan, is het mogelijk de spatiële resolutie verder te verbeteren? Deze vraag motiveert het onderzoek in dit proefschrift.

Polarisatie is een belangrijke eigenschap van licht en kan niet genegeerd worden in een strak focuserend systeem. Het is zowel theoretisch als experimenteel aangetoond dat radiaal gepolariseerd licht een scherpere focale spot kan produceren in een hoog-NA focuserend systeem vanwege de strakke longitudinale veldcomponent. Hierop voortbouwend beginnen we in dit proefschrift ons onderzoek naar de unieke focuseringseigenschappen van de radiaal gepolariseerde bundel met de vectoriële diffractietheorie. We tonen aan dat de amplitude van het focale veld kan worden gevormd door het pupilveld van de radiaal gepolariseerde bundel te bewerken. De gevormde focale spot is kleiner dan de ongemoduleerde spot, en deze kan worden gebruikt om de resolutie van optische beeldvormingssystemen te verbeteren. Hier beschouwen we een confocaal scannend beeldvormingssysteem, wat verscheidene voordelen biedt boven conventionele breedveld microscopie. In de simulatie worden longitudinale elektrische dipolen beschouwd als de objecten om optimaal gebruik te maken van de geoptimaliseerde longitudinale component. Een experimenteel bewijs wordt ook gegeven, dat laat zien dat hogere spatiële resolutie behaald kan worden wanneer het gemoduleerde radiaal gepolariseerd licht toegepast wordt in de confocale beeldvormingsopstelling vergeleken met het ongemoduleerde geval. Radiaal gepolariseerd licht kan verkregen worden met een op vloeibaar kristallen gebaseerde polarisatie-omzetter, beginnend met een lineair gepolariseerde bundel. Amplitudemodulatie van de pupil zoals het annulaire pupilveld en het ontworpen pupilveld waar de amplitude geleidelijk toeneemt met de straal kan worden gerealiseerd met een spatiële lichtmodulator (SLM).

Het substraat is essentieel voor het ondersteunen van het af te beelden monster. Meestal is het materiaal van het substraat glas. In het nabije veld, wanneer het object interageert met het lichtveld, kan het evanescente golven produceren die zeer snel afnemen en weinig invloed hebben op de beeldvorming. De evanescente golf draagt echter een hogere spatiële frequentie dan de propagerende golf. Een goed ontworpen substraat met een dunne TiO_2 laag erbovenop kan de evanescente golf in het nabije veld versterken. Het versterkte veld wordt omgezet in een propagerende golf met behulp van het object dat is afgezet op het substraat en het kan worden waargenomen in het verre veld. Het principe kan verklaard worden met een dipoolmodel, en gesimuleerd worden met nanosferen. Het is aangetoond dat de ontworpen structuur helpt om beeldkwaliteit te verbeteren, inclusief contrast en resolutie. Bovendien kan zo'n voorbeeldmodel gecombineerd worden met andere

afbeeldingstechnieken, bijvoorbeeld confocale scanmicroscopie, breedveld afbeeldingssysteem, etc.

Naast amplitude en polarisatie kunnen focale velden ook in de fase gevormd worden. In tegenstelling tot de specifieke radiaal of azimuthaal gepolariseerde vectorbundel, is de cilindrische vectorbundel een algemenere vorm. De focuserende eigenschappen en de spin-baan interacties van cilindrische vector vortex bundels in hoog-NA focuseringsystemen zijn theoretisch bestudeerd. Een absorberende nanosfeer kan gevangen worden op de hotspot van het gefocuseerde veld, zelfs wanneer de axiale symmetrie van het veld verbroken is. De analyse van de invloed van parameters zoals de initiële fase van de vortex bundel, de topologische lading, of de grootte en het materiaal van de vangbol op het samenspel tussen het spin en impulsmoment kan nuttig zijn voor optisch trapping, deeltjestransport, en superresolutie.

Abbreviations

IC	Integrated Circuit
DUV	Deep Ultraviolet
EUV	Extreme Ultraviolet
NA	Numerical Aperture
DOF	Depth of Focus
PMT	Photomultiplier Tubes
CLSM	Confocal Laser Scanning Microscopy
STED	Stimulated Emission Depletion
PALM	Photoactivated Localization Microscopy
STORM	Stochastic Optical Reconstruction Microscopy
BOE	Binary Optics
PSF	Point Spread Function
FWHM	Full Width at Half Maximum
HWHM	Half Width at Half Maximum
BS	Beam Splitter
SLM	Spatial Light Modulator
RP	Radially Polarized
LC	Liquid Crystal
LCoS	Liquid Crystal on Silicon
CCD	Coupled Charge Device
TiO₂	Titanium Dioxide
3D	Three Dimensional
FDTD	Finite Difference Time Domain
SNR	Signal to Noise Ratio
2D	Two Dimensional
NSOM	Near Field Scanning Optical Microscopy
Pol.con	Polarization Convertor
NP	Nanoparticle
PS	Polystyrene
PSL	Polystyrene Latex
PMMA	Methacrylate
PE	Polyethylene
AM	Angular Momenta
CVV	Cylindrical Vortex Vector
OV	Optical Vortices
SAM	Spin Angular Momentum
OAM	Orbital Angular Momentum

RPV	Radially Polarized Vortex
APV	Azimuthally Polarized Vortex
RH	Right Handed
LH	Left Handed
CFS	Coherent Fourier Scatterometry
PR	Photoresist
InSb	Indium Antimonide
SiO₂	Silicon Dioxide
SnO₂	Tin(IV) Oxide
ZnO	Zinc Oxide
Si₃N₄	Silicon Nitride

1

Introduction

1.1. The point spread function

The common way to characterize the resolving capability of an imaging system is to consider the image of a point source with a finite size, which can be defined as point spread function (PSF). The standard derivation of the PSF is based on the classical theory of scalar theory and the paraxial approximation [1–3]. For uniform filling (plane wave) of the entrance pupil, the image is the inverse Fourier transform of the pupil function. The resulting intensity for an ideal circular aperture is written as:

$$I = \left| \frac{J_1(2\pi\rho)}{\pi\rho} \right|^2, \quad (1.1)$$

where J_1 is the Bessel function of the first kind, and ρ is the radial distance from the center of the image normalized by multiplying by $\frac{\rho}{\lambda}$. Here λ is the wavelength of the illumination and NA is the numerical aperture. The intensity in Eq. 1.1 is the PSF of the optical system. The PSF (also called the Airy disk, after George Biddle Airy) is a widely used metric of imaging quality in optical design and manufacturing. The narrower the PSF, the better the spatial resolution will be.

Each point source can be identified on the basis of its PSF having certain charac-

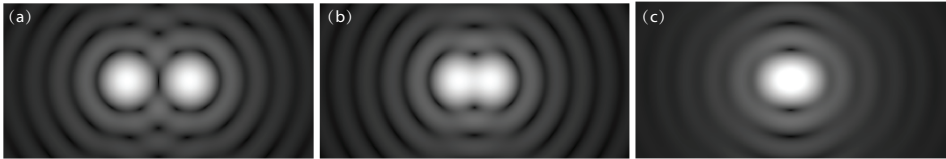


Figure 1.1: Profiles for describing spatial resolution. (a) Two points are well resolved, (b) Two points are separated by the Rayleigh limit and barely resolved, (c) Two points overlap.

teristic width. If two point sources are getting closer and closer in the object plane, their PSFs will start to overlap and as consequence that they will collapse to one PSF, where they are not distinguishable in the image plane, see Fig. 1.1. This process defines the spatial resolution, which depends on the minimum distinguishable distance between two adjacent object points. The condition of being resolved or not can be judged with Rayleigh criterion, which is given by

$$d = 0.61 \frac{\lambda}{\text{NA}}, \quad (1.2)$$

By this criterion, two closely spaced object points are defined as being resolved when the central diffraction spot (Airy disk) of one point coincides with the first diffraction minimum of the other point in the image plane. The Rayleigh resolution limit pertains to two luminous points in a dark field or to objects illuminated by incoherent light.

For an optical imaging system, Abbe's formulation [4] states the diffraction limit

given by:

$$D = \frac{\lambda}{2nNA}, \quad (1.3)$$

Abbe's resolution limit considers the paraxial PSF of two point sources with axes perpendicular to the optical axis. However, when the point sources are aligned along the optical axis and they emit coherently, the combined PSF will be different, and one must redefine the criterion for resolution [5].

Regardless of the resolution defined by the Rayleigh criterion or the Abbe's formulation, one can see that spatial resolution is determined by the wavelength of illumination and the NA of the objective lens. Once the NA increases, tighter focused spot can be formed so that higher spatial resolution can be achieved, and the scalar theory should be replaced by the vectorial diffraction theory. For further shrinking focal spot sizes, the light beam that is incident on the lens can be modulated by different amplitudes, phase distributions as well as polarizations, which is known as beam shaping.

1.2. Confocal microscopy

The invention of confocal microscopy is attributed to Marvin Minsky, who produced a working microscope in 1955 [6]. A theoretical analysis of confocal and laser-scanning microscopes was published in 1977 [7]. It was the first publication using the term "confocal microscope" and used epi-laser-illumination, stage scanning and photomultiplier tubes (PMT) as detectors [8]. Confocal microscopes have several advantages as compared to normal microscopes such as the possibility of optical sectioning and resolution improvement, and have become quite popular in biological applications [9]. Computer controlled confocal microscopy has been introduced in 1983 [10], and after that, commercial confocal laser scanning microscopy (CLSM) was developed [11, 12]. Nowadays, the confocal imaging system has been widely used in biological science and medical areas, quantum optics as well as nano-crystal imaging and spectroscopy.

In wide field microscopy, all parts of the sample are excited at the same time and the signal is detected including a large amount of unfocused (surrounding) light. Confocal microscopy has better lateral and axial resolution, because the illumination is a focused laser beam and at the detector on the image plane, a small pinhole is added. The former gives a small illumination spot while the latter helps to remove the out-of-focus light. Therefore, the total PSF of the confocal imaging system can be regarded as the product of an excitation PSF and a detection PSF as follows

$$\text{PSF}_{total} \approx \text{PSF}_{illumination} \times \text{PSF}_{detection}. \quad (1.4)$$

The benefit of confocal microscopy lies mostly in the axial sectioning capabilities in dense samples. Thus over the past years, different variations of confocal microscope have been developed, especially combining with the fluorescent imaging. The main purpose is to create 3D images of high resolution. The work on the improving the performance of the optical system focuses on optimizing the pinhole

size [13] or increasing the scanning efficiency with pinhole array, spinning-disk and micro-lenses. However, the increase in the transverse resolution achieved by confocal microscopy is marginal, often only a small percentage. Once the numerical aperture and wavelength are fixed, further improvement of the $PSF_{illumination}$ can be realized with pupil engineering, i.e., by shaping the amplitude, phase and polarization of the illumination.

1.3. Thesis Structure

Light is a manifestation of electromagnetic force, while matter is made up of charged particles due to the nature of atoms. The study of the interaction between light and matter is the heart of optical physics and has further being developed with the generation of structured optical fields as well as new materials [14, 15]. Modulation of polarization, phase and amplitude of the electric field can be realized thanks to the development of the techniques, including spatial light modulators (SLM) [16–18], meta-surfaces [19–21], q-plates [22, 23], cylindrical lenses [24] and so on. The produced optical field gives us a new perspective in exploring the physics of the light and matter interactions and also brings new applications. For instance, a tightly focused radially polarized spot can be used to detect the orientation of fluorescent molecules [25] or achieve super-resolution in microscopy [26, 27]. Another example is optical trapping with focused light, which originates from forces induced by electromagnetic fields; it has been used as a powerful scientific tool to study physical, chemical and biological characteristics of sub-wavelength objects [28, 29].

In this thesis, we show designs to obtain sharper focal spots for the confocal system, optimization of structures on samples to improve resolution, and we also explore the spin-orbit interactions for optical manipulation. The investigation includes theoretical modeling, numerical simulation and experimental validation. The thesis is composed of the following chapters:

Chapter 2: Theoretical analysis on confocal imaging with radially polarized light. We introduce the vectorial theory to calculate the focal field in the high NA system, where it has been demonstrated that radially polarized light combined with amplitude modulation results in a smaller focal spot than that of the conventional (non-modulated) radially polarized light. The principle of confocal imaging system is theoretically studied from the illumination to the imaging plane with the longitudinal electric dipole as the sample at the objective plane. With the optimized illumination, a distinguishable distance between two objects of 0.36λ is achieved, which is beyond the diffraction limit and makes super-resolution possible for non-fluorescent samples.

Chapter 3: Experimental demonstration of resolution enhancement with modulated radially polarized light. This chapter confirms the theoretical prediction in chapter 2 with a confocal imaging set-up. The radially polarized light is produced with a polarization convertor and modulated with a reflective SLM. Discussions on the convertor and the sample preparation are included. The imaging quality is quantified with visibility and analysis of the derivative of the image profiles. The results show that 0.358λ is the smallest distinguishable distance in a confocal sys-

tem with $NA=0.9$, which agrees well with the theoretical results.

Chapter 4: Super-resolution effect due to a thin dielectric slab for imaging with radially polarized light. Evanescent wave carries high spatial frequency information but decays rapidly and can not propagate to the far field. In this chapter, we show that by designing a thin TiO_2 layer on the top of the glass substrate, the evanescent wave in the near field can be enhanced. The evanescent wave re-excites the sample which transfers it to propagating wave that is detectable in the far field. Numerical analysis validates the idea and a simple experiment is conducted to show the resolution improvement. The proposed method is easy to realize compared with other special structures and the designed model of the sample can be combined with other microscopy techniques.

Chapter 5: Angular momentum properties of cylindrical vector vortex beams. The previous work excludes the influence of the phase of the light in focus, since the obtained image is at focal plane in confocal microscopy. In this chapter, we discuss the tightly focusing properties of symmetrical and asymmetrical cylindrical vector vortex beams using Richards-Wolf vector theory. Because of the vortex phase, the light has orbital angular momentum (OAM). The interaction and transfer between spin and orbital angular momentum, and the optical force and torque of an absorptive nanosphere in the vortex beam are studied. The influence of parameters like initial phase's angle, topological charge, polarization state on the motion of the nanosphere provides guidance for the optical manipulation or optical trapping.

Chapter 6: Conclusion and outlook. A summary of the thesis and discussion for the potential future work are presented.

References

- [1] M. Born and E. Wolf, *Principles of optics: electromagnetic theory of propagation, interference and diffraction of light* (Elsevier, 2013).
- [2] E. Hecht *et al.*, *Optics* (Addison Wesley San Francisco, 2002).
- [3] C. Mack, *Fundamental principles of optical lithography: the science of micro-fabrication* (John Wiley & Sons, 2008).
- [4] E. Abbe, *Beiträge zur theorie des mikroskops und der mikroskopischen wahrnehmung*, *Archiv für mikroskopische Anatomie* **9**, 413 (1873).
- [5] L. Novotny and B. Hecht, *Principles of nano-optics* (Cambridge university press, 2012).
- [6] M. Minsky, *Memoir on inventing the confocal scanning microscope*, *Scanning* **10**, 128 (1988).
- [7] C. Sheppard and A. Choudhury, *Image formation in the scanning microscope*, *Optica Acta: International Journal of Optics* **24**, 1051 (1977).
- [8] S. Inoué, *Foundations of confocal scanned imaging in light microscopy*, in *Handbook of biological confocal microscopy* (Springer, 2006).

- [9] W. Amos and J. White, *How the confocal laser scanning microscope entered biological research*, *Biology of the Cell* **95**, 335 (2003).
- [10] I. J. Cox and C. J. R. Sheppard, *Scanning optical microscope incorporating a digital framestore and microcomputer*, *Appl. Opt.* **22**, 1474 (1983).
- [11] J. White, W. Amos, and M. Fordham, *An evaluation of confocal versus conventional imaging of biological structures by fluorescence light microscopy*. *The Journal of cell biology* **105**, 41 (1987).
- [12] K. Carlsson, P. E. Danielsson, R. Lenz, A. Liljeborg, L. Majlöf, and N. Åslund, *Three-dimensional microscopy using a confocal laser scanning microscope*, *Optics Letters* **10**, 53 (1985).
- [13] P. Török, P. D. Higdon, and T. Wilson, *Theory for confocal and conventional microscopes imaging small dielectric scatterers*, *Journal of Modern Optics* **45**, 1681 (1998).
- [14] H. Rubinsztein-Dunlop, A. Forbes, M. V. Berry, M. R. Dennis, D. L. Andrews, M. Mansuripur, C. Denz, C. Alpmann, P. Banzer, T. Bauer, *et al.*, *Roadmap on structured light*, *Journal of Optics* **19**, 013001 (2016).
- [15] M. Woerdemann, C. Alpmann, M. Esseling, and C. Denz, *Advanced optical trapping by complex beam shaping*, *Laser & Photonics Reviews* **7**, 839 (2013).
- [16] R. A. Suarez, A. A. Neves, and M. R. Gesualdi, *Generation and characterization of an array of airy-vortex beams*, *Optics Communications* **458**, 124846 (2020).
- [17] N. Matsumoto, T. Ando, T. Inoue, Y. Ohtake, N. Fukuchi, and T. Hara, *Generation of high-quality higher-order laguerre-gaussian beams using liquid-crystal-on-silicon spatial light modulators*, *J. Opt. Soc. Am. A* **25**, 1642 (2008).
- [18] A. S. Ostrovsky, C. Rickenstorff-Parrao, and V. Arrizón, *Generation of the "perfect" optical vortex using a liquid-crystal spatial light modulator*, *Optics Letters* **38**, 534 (2013).
- [19] P. Yu, S. Chen, J. Li, H. Cheng, Z. Li, W. Liu, B. Xie, Z. Liu, and J. Tian, *Generation of vector beams with arbitrary spatial variation of phase and linear polarization using plasmonic metasurfaces*, *Optics Letters* **40**, 3229 (2015).
- [20] X. Ma, M. Pu, X. Li, C. Huang, Y. Wang, W. Pan, B. Zhao, J. Cui, C. Wang, Z. Zhao, *et al.*, *A planar chiral meta-surface for optical vortex generation and focusing*, *Scientific Reports* **5**, 10365 (2015).
- [21] F. Yue, D. Wen, J. Xin, B. D. Gerardot, J. Li, and X. Chen, *Vector vortex beam generation with a single plasmonic metasurface*, *ACS photonics* **3**, 1558 (2016).
- [22] P. Chen, W. Ji, Y. Wei, W. Hu, V. Chigrinov, and Y. Lu, *Generation of arbitrary vector beams with liquid crystal polarization converters and vector-photoaligned q-plates*, *Appl. Phys. Lett.* **107**, 241102 (2015).

- [23] F. Cardano, E. Karimi, S. Slussarenko, L. Marrucci, C. de Lisio, and E. Santamato, *Polarization pattern of vector vortex beams generated by q-plates with different topological charges*, *Appl. Opt.* **51**, C1 (2012).
- [24] M. Reicherter, T. Haist, E. U. Wagemann, and H. J. Tiziani, *Optical particle trapping with computer-generated holograms written on a liquid-crystal display*, *Optics Letters* **24**, 608 (1999).
- [25] T. Züchner, A. V. Failla, and A. J. Meixner, *Light microscopy with doughnut modes: a concept to detect, characterize, and manipulate individual nanoobjects*, *Angewandte Chemie International Edition* **50**, 5274 (2011).
- [26] F. Balzarotti, Y. Eilers, K. C. Gwosch, A. H. Gynnå, V. Westphal, F. D. Stefani, J. Elf, and S. W. Hell, *Nanometer resolution imaging and tracking of fluorescent molecules with minimal photon fluxes*, *Science* **355**, 606 (2017).
- [27] L. Thibon, L. E. Lorenzo, M. Piché, and Y. D. Koninck, *Resolution enhancement in confocal microscopy using bessel-gauss beams*, *Optics Express* **25**, 2162 (2017).
- [28] A. Ashkin, *Acceleration and trapping of particles by radiation pressure*, *Phys. Rev. Lett.* **24**, 156 (1970).
- [29] K. C. Neuman and S. M. Block, *Optical trapping*, *Review of Scientific Instruments* **75**, 2787 (2004).

2

Theoretical analysis on confocal imaging with radially polarized light

Rigorous vectorial focusing theory is used to study the imaging of small adjacent particles with a confocal laser scanning system. We consider radially polarized illumination with an optimized amplitude distribution and an annular amplitude distribution at the lens to obtain a narrower distribution of the longitudinal component of the field in focus. A polarization convertor at the detector side is added to transform radial polarization to linear polarization in order to make the signal detectable with a single mode fiber.

2.1. Introduction

Many super-resolution microscopes such as STED [2], PALM [3], and STORM [4] have become very important in science and applications because of their high quality images. While the applications of these super-resolution microscopy are attractive, there are some disadvantages like extremely expensive systems, time-consuming data acquisition and choices of fluorescent dyes, which limit the techniques in some cases. Although the lateral resolution of conventional confocal imaging systems is limited because of the diffraction limit, confocal microscopy has a wide range of applications in the biological and medical sciences [5–7], as well as nano-crystal imaging and spectroscopy [8, 9]. Thus, the development of a cheap and simplified confocal system combined with super-resolution imaging is very attractive.

The total point spread function (PSF) of the confocal system is determined by both the excitation PSF and the detection PSF, where the former is related to the focused illumination and the latter depends on the small pinhole or a fiber in the detector plane [10]. A very small pinhole which can remove the out of focus information plays an important role in improving both the axial and lateral resolutions in confocal microscopy. Wilson [11] compares the images theoretically and experimentally of scatterers using conventional and confocal microscopes. However, only linearly and circularly polarized beams are considered there. Cylindrical vector beams are well-established tools in optics because of the applicability of radially polarized beams in several areas. For example, using radially polarized light, the longitudinal electric component of the illuminating focused spot can be made small [12–14]. Provided the sample interacts only with the longitudinal component, higher resolution can be obtained. For a high numerical aperture (NA) system, and a radially polarized pupil field, the longitudinal component can be enhanced compared to the transverse component by using an annular aperture in the pupil of the focusing objective. The latter also results in a tighter focusing spot size of the longitudinal component in the focal plane [15–17], although this is at the expense of stronger side lobes which will reduce the imaging quality. However, annular apertures do not give the largest longitudinal component in focus. Other pupil filter functions, for example, a BOE [18–21], a parabolic mirror and a flat diffractive lens [22] are proposed to achieve sharper focal spot sizes and as a consequence, higher resolution. By shaping the radially polarized pupil field such that the amplitude increases monotonically in a specific way as function of the pupil radius, the full-width-at-half-maximum (FWHM) of the intensity of longitudinal component reaches a value that is 15% to 30% lower than that of the spot of a focused linear polarized pupil field [23]. Spot-size reduction by means of focusing the optimized radially polarized light is shown experimentally according to theoretical productions [24]. However, in a confocal configuration, when strong longitudinal field excites a longitudinal sensitive sample, for example, a dipole is oriented parallel to the optical axis, the consequence is that its image with low NA that is formed at the pinhole side has a zero at the center [25]. In order to make the signal detectable, a polarization convertor placed in the path of detection plane is proposed to engineer the detection PSF from a doughnut shape to one with maximum in the center

[26]. In the reference [27], good imaging results are achieved with the confocal microscope together with a polarization convertor experimentally. However, the theoretical analysis of the entire system is not complete.

In this chapter, we present a fully rigorous vectorial theory to describe the whole confocal imaging process in a high NA system with spatially shaped radially polarized illumination. The optimized pupil field which maximizes the longitudinal electric field component in the focal point [23] is compared with the linearly polarized and traditional radially polarized pupil field to validate that the former one gives higher lateral resolution. The annular pupil field with radially polarized illumination is also considered. We use two longitudinally oriented electric dipoles at variable distances as test object. Other orientations can be easily considered. A suitable pinhole size is chosen before the detector plane to enhance the system performance, and a polarization convertor is inserted in the collimated optical path before the pinhole to transform the radially polarized light scattered by the object back to linearly polarized light to optimize the power of the light after the pinhole.

2.2. Dipole excitation using a focused spot

Rigorous analysis of vectorial image formation in the confocal system can be found in [10]. In this chapter we consider different polarizations and optimized pupil field for the illumination. Fig. 2.1(a) shows the configuration of the confocal imaging system. In order to make the whole analytical process clear, we consider first the focusing spot which illuminates the sample. This focused spot excites electric dipoles in the sample which are then imaged on the detector. The imaging of the excited dipoles is studied in subsequent sections.

2.2.1. Vectorial Diffraction Integral

In scalar diffraction theory the focal field of a lens is considered without taking into account the vectorial nature of the light field. However, the scalar method is not valid for optical systems of high NA and vectorial theory is needed to describe the field near the focal plane. Originating from Ignatovsky's diffraction theory [28], later studied in details in [29, 30], the solution is referred as the vectorial Richard-Wolf integral.

All optical fields here are time harmonic with time dependence given by the factor $\exp(-i\omega t)$, where $\omega > 0$ is the frequency. This factor is omitted from all formulas below. Consider an incoming beam that is propagating parallel to the optical axis and is focused by a high NA objective lens L_1 as shown in Fig. 2.1(b). We choose a coordinate system (x, y, z) with z -axis coinciding with the optical axis and origin at the Gaussian focal point of lens L_1 and such that the illuminating beam propagates in the positive z -direction. When focused in a homogeneous medium with real refractive index n , the electric and magnetic fields in the focal region of lens L_1 can

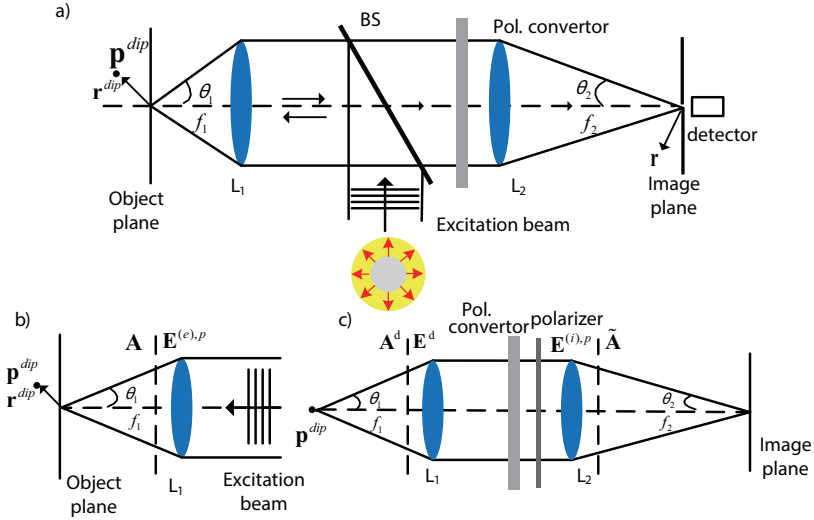


Figure 2.1: Schematic of the confocal microscope. A beam splitter (BS) divides the excitation path and detection path into two arms. A laser beam is focused onto the sample by a high NA objective lens L_1 . The light scattered by the sample is collected by the same objective lens and focused by a small NA lens onto a pinhole in front of a detector. a) The complete confocal microscopy system, b) Focusing and dipole excitation, c) Imaging and polarization conversion.

be expanded into plane waves:

$$\begin{aligned}
 \mathbf{E}^e(\mathbf{r}) &= \frac{1}{4\pi^2} \iint_{k_{\perp} \leq k_0 \text{NA}_1} \mathbf{A}(\mathbf{k}_{\perp}) \exp(i\mathbf{k} \cdot \mathbf{r}) d^2 k_{\perp}, \\
 \mathbf{H}^e(\mathbf{r}) &= \frac{1}{4\pi^2} \frac{1}{\omega \mu_0} \iint_{k_{\perp} \leq k_0 \text{NA}_1} \mathbf{k} \times \mathbf{A}(\mathbf{k}_{\perp}) \exp(i\mathbf{k} \cdot \mathbf{r}) d^2 k_{\perp},
 \end{aligned} \tag{2.1}$$

where $\mathbf{A}(\mathbf{k}_{\perp})$ is the vector amplitude of the plane wave with the wave vector $\mathbf{k} = (k_x, k_y, k_z)$, $\mathbf{k}_{\perp} = (k_x, k_y)$ is the part of the wave vector perpendicular to the optical axis, with $k_{\perp} = \sqrt{k_x^2 + k_y^2}$ its length, $k_z = \sqrt{k^2 - k_{\perp}^2}$, where $k = k_0 n$ with $k_0 = 2\pi/\lambda_0$ with λ_0 the wavelength in vacuum. Note that the transverse wavenumber k_{\perp} satisfies: $0 \leq k_{\perp} \leq k_0 \text{NA}_1$, where $\text{NA}_1 = n \sin \theta_{\max}^{(1)}$ with $\theta_{\max}^{(1)}$ the maximum angle between the wave vectors and the positive z direction. Without loss of generality, we consider the optical system is placed in vacuum so that the refractive index is $n = 1$ in both object and image space.

To define the polarizations of the plane waves, we define a positively oriented

orthonormal basis $\hat{\mathbf{k}}, \hat{\mathbf{p}}, \hat{\mathbf{s}}$ in reciprocal \mathbf{k} -space by:

$$\begin{aligned}\hat{\mathbf{k}} &= \frac{k_x}{k} \hat{\mathbf{x}} + \frac{k_y}{k} \hat{\mathbf{y}} + \frac{k_z}{k} \hat{\mathbf{z}}, \\ \hat{\mathbf{p}}(\mathbf{k}_\perp) &= \frac{k_x k_z \hat{\mathbf{x}} + k_y k_z \hat{\mathbf{y}} - k_\perp^2 \hat{\mathbf{z}}}{k k_\perp}, \\ \hat{\mathbf{s}}(\mathbf{k}_\perp) &= \frac{-k_y \hat{\mathbf{x}} + k_x \hat{\mathbf{y}}}{k_\perp},\end{aligned}\quad (2.2)$$

Since the electric field is free of divergence, the vector amplitude \mathbf{A} can be written as:

$$\mathbf{A}(\mathbf{k}_\perp) = A_p(\mathbf{k}_\perp) \hat{\mathbf{p}}(\mathbf{k}_\perp) + A_s(\mathbf{k}_\perp) \hat{\mathbf{s}}(\mathbf{k}_\perp), \quad (2.3)$$

where A_p and A_s are the components of \mathbf{A} on the basis of $\hat{\mathbf{p}}$ and $\hat{\mathbf{s}}$, respectively. The electromagnetic field in focus can be therefore rewritten as:

$$\begin{aligned}\mathbf{E}^e(\mathbf{r}) &= \frac{1}{4\pi^2} \iint_{k_\perp \leq k_0 NA_1} (A_p \hat{\mathbf{p}} + A_s \hat{\mathbf{s}}) e^{i\mathbf{k}\cdot\mathbf{r}} d^2 k_\perp, \\ \mathbf{H}^e(\mathbf{r}) &= \frac{1}{4\pi^2} \frac{1}{\omega \mu_0} \iint_{k_\perp \leq k_0 NA_1} (-A_s \hat{\mathbf{p}} + A_p \hat{\mathbf{s}}) e^{i\mathbf{k}\cdot\mathbf{r}} d^2 k_\perp.\end{aligned}\quad (2.4)$$

According to the vectorial diffraction theory [28–30], the plane wave amplitudes A_p, A_s are linked to the radial and azimuthal components of the pupil field by:

$$A_p(\mathbf{k}_\perp) = \frac{2\pi i f_1}{\sqrt{k k_z}} E_{\rho}^{e,p}(\rho_p, \varphi_p), \quad A_s(\mathbf{k}_\perp) = \frac{2\pi i f_1}{\sqrt{k k_z}} E_{\varphi}^{e,p}(\rho_p, \varphi_p), \quad (2.5)$$

where, f_1 is the focal distance of the objective lens L_1 and ρ_p, φ_p are polar pupil coordinates defined by:

$$\rho_p = f_1 \frac{k_\perp}{k_0 n}, \quad \rho_p \cos \varphi_p = -f_1 \frac{k_x}{k_0 n}, \quad \rho_p \sin \varphi_p = -f_1 \frac{k_y}{k_0 n}, \quad (2.6)$$

Note that

$$\cos \varphi_p = -k_x/k_\perp, \quad \sin \varphi_p = -k_y/k_\perp. \quad (2.7)$$

2.2.2. Focal field of linearly and radially polarized light

When the pupil field is in all points of the pupil linearly polarized parallel to the x -direction, we have:

$$E_{\rho}^{e,p}(\rho_p, \varphi_p) = g(\rho_p) \cos \varphi_p, \quad E_{\varphi}^{e,p}(\rho_p, \varphi_p) = g(\rho_p) \sin \varphi_p, \quad (2.8)$$

where $g(\rho_p)$ is the amplitude which may be a function of the radius. Using Eq. 2.7, we get:

$$A_p(\mathbf{k}_\perp) = \frac{-2\pi i f_1 k_x}{\sqrt{k k_z k_\perp}} g(k_\perp), \quad A_s(\mathbf{k}_\perp) = \frac{-2\pi i f_1 k_y}{\sqrt{k k_z k_\perp}} g(k_\perp), \quad (2.9)$$

where for brevity, we have written $g(k_{\perp})$ instead of $g(f_1 k_{\perp}/k)$.

We substitute Eq. 2.9 into Eq. 2.4 and use the following integrals [31]:

$$\begin{aligned} \int_0^{2\pi} \cos n\phi e^{ix \cos(\phi-\varphi)} d\phi &= 2\pi i^n J_n(x) \cos n\varphi, \\ \int_0^{2\pi} \sin n\phi e^{ix \cos(\phi-\varphi)} d\phi &= 2\pi i^n J_n(x) \sin n\varphi, \end{aligned} \quad (2.10)$$

where $J_n(x)$ is the Bessel function of n th order. By using cylindrical coordinates in the focal region, we then obtain for the electric field in the focal region:

$$\mathbf{E}^e(\rho, \varphi, z) = \frac{-if_1}{2k^{3/2}} \begin{pmatrix} -I_{00}(\rho, z) - I_{02}(\rho, z) \cos 2\varphi \\ -I_{02}(\rho, z) \sin 2\varphi \\ 2iI_{01}(\rho, z) \cos \varphi \end{pmatrix}, \quad (2.11)$$

where

$$I_{00}(\rho, z) = \int_0^{k_0 \text{NA}_1} g(k_{\perp}) (k + k_z) J_0(k_{\perp} \rho) \frac{k_{\perp}}{\sqrt{k_z}} e^{ik_z z} dk_{\perp}, \quad (2.12)$$

$$I_{01}(\rho, z) = \int_0^{k_0 \text{NA}_1} g(k_{\perp}) k_{\perp} J_1(k_{\perp} \rho) \frac{k_{\perp}}{\sqrt{k_z}} e^{ik_z z} dk_{\perp}, \quad (2.13)$$

$$I_{02}(\rho, z) = \int_0^{k_0 \text{NA}_1} g(k_{\perp}) (k - k_z) J_2(k_{\perp} \rho) \frac{k_{\perp}}{\sqrt{k_z}} e^{ik_z z} dk_{\perp}. \quad (2.14)$$

A polarized pupil field can be written as a linear combination of the radially and azimuthally polarized parts. For a pupil field which is in all points of the pupil polarized in the radial direction, the radial and azimuthal components of the electric pupil field are given by:

$$E_{\rho}^{e,p}(\rho_p, \varphi_p) = g(\rho_p), \quad E_{\varphi}^{e,p}(\rho_p, \varphi_p) = 0, \quad (2.15)$$

where the amplitude g is a function of the pupil radius. By using Eq. 2.5, we get for the p- and s-components of the electric field of the plane waves in the focal region:

$$A_p(\mathbf{k}_{\perp}) = \frac{2\pi i f_1}{\sqrt{k k_z}} g(k_{\perp}), \quad A_s(\mathbf{k}_{\perp}) = 0, \quad (2.16)$$

where (as above) we have written $g(k_{\perp})$ instead of the formally more correct $g(f_1 k_{\perp}/k)$. Then with Eq. 2.4 and the integrals of Eq. 2.10, the electric field in the focal region becomes in terms of cylindrical coordinates:

$$\mathbf{E}^e(\rho, \varphi, z) = \frac{-f_1}{k^{3/2}} \begin{pmatrix} I_{11}(\rho, z) \cos \varphi \\ I_{11}(\rho, z) \sin \varphi \\ iI_{10}(\rho, z) \end{pmatrix}, \quad (2.17)$$

where

$$I_{10}(\rho, z) = \int_0^{k_0 \text{NA}_1} g(k_\perp) k_\perp J_0(k_\perp \rho) \frac{k_\perp}{\sqrt{k_z}} e^{ik_z z} dk_\perp, \quad (2.18)$$

$$I_{11}(\rho, z) = \int_0^{k_0 \text{NA}_1} g(k_\perp) k_z J_1(k_\perp \rho) \frac{k_\perp}{\sqrt{k_z}} e^{ik_z z} dk_\perp. \quad (2.19)$$

2.2.3. Focused beam shaping

Focal field shaping by engineering the polarization, amplitude and phase on the exit pupil of an optical system [13, 32, 33], especially with the help of spatial light modulators (SLM) [34–36] and q-plates [37–39], has attracted a lot of attention in recent years. Optimal focal field shaping has many applications. For instance, tight focusing behavior of polarized beams has been investigated to achieve sharp resolution [40, 41].

We discuss now two optimized radially polarized pupil fields. The first is the pupil field derived in [23] which gives the largest possible longitudinal (i.e. z -component) of the electric field components in the focal point, for a given power P_0 in the pupil of the lens. The optimum pupil field is found to be radially polarized and its amplitude increases monotonically with distance to the optical axis. This solution makes the FWHM of the longitudinal component of the focused electric field 15%–30% narrower than that of the classical Airy spot depending on the NA. It was shown that the amplitude of this optimum pupil field is given by:

$$g(k_\perp) = -\frac{k_\perp^{3/2} k^{1/2}}{2\pi i f_1 k_z \Lambda}, \quad (2.20)$$

where

$$\Lambda = \left(\frac{\pi}{P_0}\right)^{1/2} \frac{n^{1/2}}{\lambda_0} \left(\frac{\epsilon_0}{\mu_0}\right)^{1/4} \left(\frac{2}{3} - \sqrt{1 - (\text{NA}_1/n)^2} + \frac{1}{3} \sqrt{(1 - (\text{NA}_1/n)^2)^3}\right)^{1/2}, \quad (2.21)$$

Further details of the calculations of modulating the amplitude of radially polarized light in the pupil are given in Appendix A. By substituting Eq. 2.20, Eqs. 2.18 and 2.19 become:

$$I_{10}(\rho, z) = -\frac{k^{1/2}}{2\pi i f_1 \Lambda} \int_0^{k_0 \text{NA}_1} J_0(k_\perp \rho) \frac{k_\perp^{7/2}}{k_z^{3/2}} e^{ik_z z} dk_\perp, \quad (2.22)$$

$$I_{11}(\rho, z) = -\frac{k^{1/2}}{2\pi i f_1 \Lambda} \int_0^{k_0 \text{NA}_1} J_1(k_\perp \rho) \frac{k_\perp^{5/2}}{k_z^{3/2}} e^{ik_z z} dk_\perp. \quad (2.23)$$

The second way for the amplitude g of the radially polarized pupil field which gives a narrow longitudinal component in the focal plane corresponds to an annular pupil:

$$g(\rho_p) = \begin{cases} 1 & a - \Delta\rho_p < \rho_p \leq a \\ 0 & \text{otherwise} \end{cases}, \quad (2.24)$$

where a is the radius of the pupil of the lens L_1 and $\Delta\rho_p$ is the width of the annular ring. Then the focal field is obtained by substituting Eq. 2.24 for g in Eqs. 2.17-2.19.

2.3. Dipole imaging with a polarization convertor

Figure 2.1(c) shows the imaging part of the optical system. In the Born approximation, the focused field \mathbf{E}^i excites a dipole density $\mathbf{P}^d(\mathbf{r}_d)$ at the position $\mathbf{r}_d = (x_d, y_d, z = 0)$, where the $z = 0$ plane is, as before, assumed to coincide with the focal plane of lens L_1 . The dipole vector is given by:

$$\mathbf{P}^d = \vec{\alpha}\mathbf{E}^e(\mathbf{r}_d), \quad (2.25)$$

where $\vec{\alpha}$ is the electric polarizability. It in general is a tensor, and we assume that the elements of the tensor have principal axis that are parallel to the x, y, z -axis, i.e

$$\vec{\alpha} = \begin{pmatrix} \alpha_{xx} & 0 & 0 \\ 0 & \alpha_{yy} & 0 \\ 0 & 0 & \alpha_{zz} \end{pmatrix}. \quad (2.26)$$

Let \mathbf{E}^d be the electric field radiated by this dipole. Its plane wave amplitudes in the entrance pupil of lens L_1 , i.e. for $z = f_1$, are given by [42]:

$$A^d(\mathbf{k}_\perp) = -\frac{e^{ik_z f_1}}{2i\epsilon_0 n^2 k_z} \mathbf{k} \times (\mathbf{k} \times \mathbf{P}^d), \quad (2.27)$$

Hence,

$$A_p^d(\mathbf{k}_\perp) = \frac{e^{ik_z f_1}}{2i\epsilon_0 n^2 k_z} k^2 \mathbf{P}^d \cdot \hat{\mathbf{p}}, \quad A_s^d(\mathbf{k}_\perp) = \frac{e^{ik_z f_1}}{2i\epsilon_0 n^2 k_z} k^2 \mathbf{P}^d \cdot \hat{\mathbf{s}}. \quad (2.28)$$

Although there exists longitudinal component of the field in the detector plane, it cannot be easily measured by the detector. Therefore, we only detect the transverse component. However, at the center of the detector the transverse component is very weak because of the donut shape when the illumination is radially polarized. In order to make the signal detectable, a polarization convertor [27] is added between the collimator lens and the detector, which transforms the radially polarized light into x -polarized light before being refocused by the detector. To see the difference, we consider the imaging process both with and without polarization convertors.

2.3.1. Imaging without polarization convertor

For the case without polarization convertor, the radial and azimuthal components of the pupil field can be expressed by using Eq. 2.5 and 2.6,

$$E_{\rho}^{d,p}(\rho_p, \varphi_p) = \frac{\sqrt{kk_z}}{2\pi i f_1} A_p^d(\mathbf{k}_\perp), \quad E_{\varphi}^{d,p}(\rho_p, \varphi_p) = \frac{\sqrt{kk_z}}{2\pi i f_1} A_s^d(\mathbf{k}_\perp), \quad (2.29)$$

The refocusing by the second lens L_2 with focal length f_2 yields plane wave amplitudes in image space which are given by

$$\begin{aligned}\tilde{A}_p^d(\tilde{\mathbf{k}}_\perp) &= \frac{2\pi i f_2}{\sqrt{k\tilde{k}_z}} E_\rho^{d,p}(\rho_p, \varphi_p) = \frac{f_2}{f_1} \sqrt{\frac{k_z}{\tilde{k}_z}} \frac{e^{ik_z f_1}}{2i\epsilon_0 n^2 k_z} k^2 \mathbf{P}^d \cdot \hat{\mathbf{p}}, \\ \tilde{A}_s^d(\tilde{\mathbf{k}}_\perp) &= \frac{2\pi i f_2}{\sqrt{k\tilde{k}_z}} E_\varphi^{d,p}(\rho_p, \varphi_p) = \frac{f_2}{f_1} \sqrt{\frac{k_z}{\tilde{k}_z}} \frac{e^{ik_z f_1}}{2i\epsilon_0 n^2 k_z} k^2 \mathbf{P}^d \cdot \hat{\mathbf{s}},\end{aligned}\quad (2.30)$$

with

$$\rho_p = f_2 \frac{\tilde{k}_\perp}{k}, \quad \rho_p \cos \varphi_p = -f_2 \frac{\tilde{k}_x}{k}, \quad \rho_p \sin \varphi_p = -f_2 \frac{\tilde{k}_y}{k}, \quad (2.31)$$

where the wavenumber $k = \tilde{k}$, as the two lenses are in the same medium.

Since the NA_2 of the lens L_2 before the detector is smaller than that of the objective lens L_1 , the focal distances of the two lenses are different. This implies the following relationship between the wave vectors of corresponding plane waves on the object side of lens L_1 and the image side of lens L_2 :

$$k_\perp = \frac{f_2}{f_1} \tilde{k}_\perp, \quad k_z = \sqrt{k^2 - (f_2/f_1)^2 \tilde{k}_\perp^2}. \quad (2.32)$$

By substituting Eq. 2.30 into Eq. 2.4, the electric field in image space becomes:

$$\begin{aligned}\mathbf{E}^{(i)}(\mathbf{r}) &= \frac{1}{4\pi^2} \left[\iint_{\tilde{k}_\perp \leq k_0 \text{NA}_2} (\tilde{A}_p^d(\tilde{\mathbf{k}}_\perp) \hat{\mathbf{p}}(\tilde{\mathbf{k}}_\perp) + \tilde{A}_s^d(\tilde{\mathbf{k}}_\perp) \hat{\mathbf{s}}(\tilde{\mathbf{k}}_\perp)) e^{i\tilde{\mathbf{k}} \cdot \mathbf{r}} d^2 \tilde{k}_\perp \right] \cdot \mathbf{P}^d \\ &= \frac{k^2 f_2}{4\pi i \epsilon_0 n^2 f_1} \left[\iint_{\tilde{k}_\perp \leq k_0 \text{NA}_2} \frac{1}{\sqrt{k_z \tilde{k}_z}} \left(\hat{\mathbf{p}}(\tilde{\mathbf{k}}_\perp) \otimes \hat{\mathbf{p}}\left(\frac{f_2}{f_1} \tilde{\mathbf{k}}_\perp\right) + \hat{\mathbf{s}}(\tilde{\mathbf{k}}_\perp) \otimes \hat{\mathbf{s}}\left(\frac{f_2}{f_1} \tilde{\mathbf{k}}_\perp\right) \right) \right. \\ &\quad \left. \cdot e^{ik_z f_1} e^{i\tilde{\mathbf{k}} \cdot \mathbf{r}} d^2 \tilde{k}_\perp \right] \cdot \mathbf{P}^d,\end{aligned}\quad (2.33)$$

where

$$\begin{aligned}\hat{\mathbf{p}}(\tilde{\mathbf{k}}_\perp) &= \frac{1}{k^2 \tilde{k}_\perp} \begin{pmatrix} \tilde{k}_x \tilde{k}_z \\ \tilde{k}_y \tilde{k}_z \\ -\tilde{k}_\perp^2 \end{pmatrix}, & \hat{\mathbf{p}}\left(\frac{f_2}{f_1} \tilde{\mathbf{k}}_\perp\right) &= \frac{1}{k^2 \tilde{k}_\perp} \begin{pmatrix} \tilde{k}_x k_z \\ \tilde{k}_y k_z \\ -\frac{f_2}{f_1} \tilde{k}_\perp^2 \end{pmatrix}, \\ \hat{\mathbf{s}}(\tilde{\mathbf{k}}_\perp) &= \hat{\mathbf{s}}\left(\frac{f_2}{f_1} \tilde{\mathbf{k}}_\perp\right) = \frac{1}{k^2 \tilde{k}_\perp} \begin{pmatrix} -\tilde{k}_y \\ \tilde{k}_x \\ 0 \end{pmatrix},\end{aligned}\quad (2.34)$$

Using polar coordinates, the field in the image space can be written as:

$$\begin{aligned}
 E_x^{(i)}(\rho, \varphi, z) &= \frac{-f_2}{2\epsilon_0 n^2 f_1} \left[(K_{00}^0 + K_{zz}^0) \mathbf{p}_x^{dip} - 2iK_{\perp z}^1 \cos \varphi \mathbf{p}_z^{dip} + (K_{00}^2 - K_{zz}^2) \right. \\
 &\quad \left. \cdot (\cos 2\varphi \mathbf{p}_x^{dip} + \sin 2\varphi \mathbf{p}_y^{dip}) \right], \\
 E_y^{(i)}(\rho, \varphi, z) &= \frac{-f_2}{2\epsilon_0 n^2 f_1} \left[(K_{00}^0 + K_{zz}^0) \mathbf{p}_y^{dip} - 2iK_{\perp z}^1 \sin \varphi \mathbf{p}_z^{dip} + (K_{00}^2 - K_{zz}^2) \right. \\
 &\quad \left. \cdot (\sin 2\varphi \mathbf{p}_x^{dip} - \cos 2\varphi \mathbf{p}_y^{dip}) \right], \\
 E_z^{(i)}(\rho, \varphi, z) &= \frac{-f_2}{2\epsilon_0 n^2 f_1} \left[2K_{\perp\perp}^0 \mathbf{p}_z^{dip} - 2iK_{zz}^1 (\cos \varphi \mathbf{p}_x^{dip} + \sin \varphi \mathbf{p}_y^{dip}) \right],
 \end{aligned} \quad (2.35)$$

where

$$\begin{aligned}
 K_{00}^n(\rho, z) &= \int_0^{k_0 \text{NA}_2} \left(\frac{\tilde{k}_z}{k} \right)^{1/2} \frac{\tilde{k}_\perp}{k \sqrt{k^2 - (f_2/f_1)^2 \tilde{k}_\perp^2}} J_n(\tilde{k}_\perp \rho) e^{i\tilde{k}_z z} \cdot e^{iz \sqrt{k^2 - (f_2/f_1)^2 \tilde{k}_\perp^2}} d\tilde{k}_\perp, \\
 K_{\perp\perp}^n(\rho, z) &= \int_0^{k_0 \text{NA}_2} \left(\frac{\tilde{k}_z}{k} \right)^{1/2} \frac{\tilde{k}_\perp}{k \sqrt{k^2 - (f_2/f_1)^2 \tilde{k}_\perp^2}} q_{\perp\perp}(\tilde{k}_\perp) J_n(\tilde{k}_\perp \rho) e^{i\tilde{k}_z z} \cdot e^{iz \sqrt{k^2 - (f_2/f_1)^2 \tilde{k}_\perp^2}} d\tilde{k}_\perp, \\
 K_{\perp z}^n(\rho, z) &= \int_0^{k_0 \text{NA}_2} \left(\frac{\tilde{k}_z}{k} \right)^{1/2} \frac{\tilde{k}_\perp}{k \sqrt{k^2 - (f_2/f_1)^2 \tilde{k}_\perp^2}} q_{\perp z}(\tilde{k}_\perp) J_n(\tilde{k}_\perp \rho) e^{i\tilde{k}_z z} \cdot e^{iz \sqrt{k^2 - (f_2/f_1)^2 \tilde{k}_\perp^2}} d\tilde{k}_\perp, \\
 K_{zz}^n(\rho, z) &= \int_0^{k_0 \text{NA}_2} \left(\frac{\tilde{k}_z}{k} \right)^{1/2} \frac{\tilde{k}_\perp}{k \sqrt{k^2 - (f_2/f_1)^2 \tilde{k}_\perp^2}} q_{zz}(\tilde{k}_\perp) J_n(\tilde{k}_\perp \rho) e^{i\tilde{k}_z z} \cdot e^{iz \sqrt{k^2 - (f_2/f_1)^2 \tilde{k}_\perp^2}} d\tilde{k}_\perp,
 \end{aligned} \quad (2.36)$$

with $\tilde{k}_\perp = \sqrt{\tilde{k}_x^2 + \tilde{k}_y^2}$, $\tilde{k}_z = \sqrt{k^2 - \tilde{k}_\perp^2}$, and

$$q_{\perp\perp}(\tilde{k}_\perp) = \frac{k_\perp \tilde{k}_\perp}{k^2}, \quad q_{\perp z}(\tilde{k}_\perp) = \frac{k_\perp \tilde{k}_z}{k^2}, \quad q_{zz}(\tilde{k}_\perp) = \frac{k_z \tilde{k}_z}{k^2}. \quad (2.37)$$

We introduced the term $\left(\frac{\tilde{k}_z}{k} \right)^{1/2}$ to account for an aplanatic lens.

2.3.2. Imaging with polarization convertor

As for the purpose of easy detection of the final signal, we apply a polarization convertor to transform the polarization of the light from radial to linear x before it goes to the detector. And a x polarizer is put before the detector to remove non-linear x polarized light as seen in Fig. 2.1(c). Then, the field in image space after

the convertor and the polarizer becomes

$$\mathbf{E}^{(i),p}(\rho_p, \varphi_p) = E_\rho^{d,p}(\rho_p, \varphi_p) \hat{\mathbf{x}}, \quad (2.38)$$

Due to the convertor, the radial and azimuthal components of the field in the entrance pupil of the second lens become:

$$E_\rho^{(i),p}(\rho_p, \varphi_p) = E_\rho^{d,p}(\rho_p, \varphi_p) \cos \phi, \quad E_\varphi^{(i),p}(\rho_p, \varphi_p) = -E_\rho^{d,p}(\rho_p, \varphi_p) \sin \phi, \quad (2.39)$$

The vector amplitudes of the plane waves in image space corresponding to the pupil field have p- and s- components are given by:

$$\tilde{A}_p(\tilde{\mathbf{k}}_\perp) = \frac{2\pi i f_2}{\sqrt{\tilde{k}_x \tilde{k}_z}} E_\rho^{(i),p}(\rho_p, \varphi_p), \quad \tilde{A}_s(\tilde{\mathbf{k}}_\perp) = \frac{2\pi i f_2}{\sqrt{\tilde{k}_x \tilde{k}_z}} E_\varphi^{(i),p}(\rho_p, \varphi_p), \quad (2.40)$$

Substituting Eq. 2.40 into Eq. 2.4 and using polar coordinates, finally, the field in image space can be deduced as:

$$\begin{aligned} E_x^{(i)}(\rho, \varphi, z) &= \frac{-f_2}{2\epsilon_0 n^2 f_1} \left[\frac{i}{2} (K_{zz}^3 - K_z^3) (\cos 3\varphi \mathbf{p}_x^{dip} + \sin 3\varphi \mathbf{p}_y^{dip}) - \frac{i}{2} K_{zz}^1 \right. \\ &\quad \cdot (3 \cos \varphi \mathbf{p}_x^{dip} + \sin \varphi \mathbf{p}_y^{dip}) - \frac{i}{2} K_z^1 (\cos \varphi \mathbf{p}_x^{dip} + 3 \sin \varphi \mathbf{p}_y^{dip}) \\ &\quad \left. - (K_{\perp z}^2 - K_\perp^2) \cos 2\varphi \mathbf{p}_z^{dip} + (K_{\perp z}^0 + K_\perp^0) \mathbf{p}_z^{dip} \right], \\ E_y^{(i)}(\rho, \varphi, z) &= \frac{-f_2}{2\epsilon_0 n^2 f_1} \left[\frac{i}{2} (K_{zz}^3 - K_z^3) (\sin 3\varphi \mathbf{p}_x^{dip} - \cos 3\varphi \mathbf{p}_y^{dip}) - \frac{i}{2} (K_{zz}^1 - K_z^1) \right. \\ &\quad \cdot (\sin \varphi \mathbf{p}_x^{dip} + \cos \varphi \mathbf{p}_y^{dip}) - (K_{\perp z}^2 - K_\perp^2) \sin 2\varphi \mathbf{p}_z^{dip} \left. \right], \\ E_z^{(i)}(\rho, \varphi, z) &= \frac{-f_2}{2\epsilon_0 n^2 f_1} \left[-K_{z\perp}^0 \mathbf{p}_x^{dip} + K_{z\perp}^2 (\cos 2\varphi \mathbf{p}_x^{dip} + \sin 2\varphi \mathbf{p}_y^{dip}) + 2i K_{\perp\perp}^1 \cos \varphi \mathbf{p}_z^{dip} \right], \end{aligned} \quad (2.41)$$

where

$$\begin{aligned} K_{z\perp}^n(\rho, z) &= \int_0^{k_0 \text{NA}_2} \left(\frac{\tilde{k}_z}{k} \right)^{1/2} \frac{\tilde{k}_\perp}{k \sqrt{k^2 - (f_2/f_1)^2 \tilde{k}_\perp^2}} q_{z\perp}(\tilde{k}_\perp) J_n(\tilde{k}_\perp \rho) e^{i\tilde{k}_z z} \cdot e^{iz \sqrt{k^2 - (f_2/f_1)^2 \tilde{k}_\perp^2}} d\tilde{k}_\perp, \\ K_z^n(\rho, z) &= \int_0^{k_0 \text{NA}_2} \left(\frac{\tilde{k}_z}{k} \right)^{1/2} \frac{\tilde{k}_\perp}{k \sqrt{k^2 - (f_2/f_1)^2 \tilde{k}_\perp^2}} q_z(\tilde{k}_\perp) J_n(\tilde{k}_\perp \rho) e^{i\tilde{k}_z z} \cdot e^{iz \sqrt{k^2 - (f_2/f_1)^2 \tilde{k}_\perp^2}} d\tilde{k}_\perp, \\ K_\perp^n(\rho, z) &= \int_0^{k_0 \text{NA}_2} \left(\frac{\tilde{k}_z}{k} \right)^{1/2} \frac{\tilde{k}_\perp}{k \sqrt{k^2 - (f_2/f_1)^2 \tilde{k}_\perp^2}} q_\perp(\tilde{k}_\perp) J_n(\tilde{k}_\perp \rho) e^{i\tilde{k}_z z} \cdot e^{iz \sqrt{k^2 - (f_2/f_1)^2 \tilde{k}_\perp^2}} d\tilde{k}_\perp, \end{aligned} \quad (2.42)$$

where

$$q_{z\perp}(\tilde{k}_\perp) = \frac{k_z \tilde{k}_\perp}{k^2}, \quad q_\perp(\tilde{k}_\perp) = \frac{k_\perp}{k}, \quad q_z(\tilde{k}_\perp) = \frac{k_z}{k}. \quad (2.43)$$

and k_\perp and k_z are functions of \tilde{k}_\perp given by Eq. 2.32. Other symbols are shown in Eq. 2.37. Again, we introduced the term $\left(\frac{\tilde{k}_z}{k}\right)^{1/2}$ to account for an aplanatic lens.

2.4. Numerical results and discussions

Through this section, we assume the light with wavelength $\lambda = 500\text{nm}$. With Eqs. 2.11 and 2.17, the focal fields of linearly and radially polarized illumination can be obtained. It is important to note, that in the case of tightly focusing ($\text{NA}=0.9$), the focal fields have different polarizations which vary across the focal spots. This is clearly illustrated in Fig. 2.2. When the incident light is linear x (Fig. 2.2(a₁)-(c₁)), it not only produces a field at focus that is linear x , but also in the other two directions (y - and z -). The total field intensity $|\mathbf{E}|^2$ is not cylindrically symmetric in the case of linearly illumination as shown in Fig. 2.2(d₁). However, the asymmetry can be avoided by considering the cylindrically symmetric vector beam of radial polarization, which can be seen in Fig. 2.2(a₂)-(d₂). Besides of this, one can see that a radially polarized light results in a strong and narrow longitudinal component (z component) around the focus.

Fig. 2.3 compares the profiles of the different components when focusing linearly

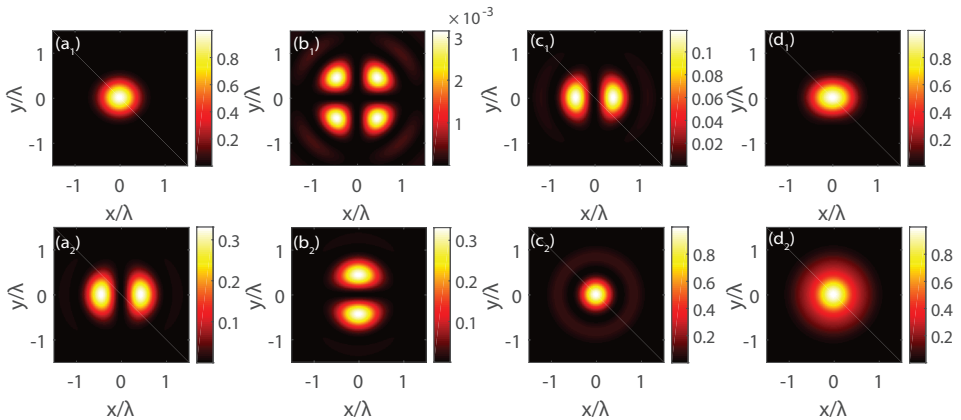


Figure 2.2: Intensity distributions of x -, y -, z - and total field components at focus in air due to the illuminations of linearly x (a₁) – (d₁) and radially (a₂) – (d₂) polarized light at the $\text{NA}=0.9$ objective lens pupil. x and y axes are normalized in units of λ and the plots are normalized to the peak total intensities.

and radially polarized beams. It follows that the FWHM (two times of the HWHM) of the total intensity in the focal plane of the radially polarized pupil field, is slightly smaller than that of a linearly pupil field ($\text{FWHM}_{total}^{rad} \approx 0.72\lambda$, $\text{FWHM}_{total}^{lin} \approx 0.76\lambda$).

In contrast, the FWHM of the squared modulus of the longitudinal component corresponding to the radially polarized pupil field ($\text{FWHM}_{long}^{rad} = 0.48\lambda$), is much smaller than the FWHM of $|\mathbf{E}|^2$ in the case of a linearly polarized pupil field. Thus, the polarization state of the light strongly influences the size of the focused spot in the case of high NA. If the sample is sensitive only to the longitudinal component of the focal spot, then the use of radially polarized light can result in a substantial improvement in resolution.

Figure 2.4(a) shows the comparison of intensities of the longitudinal components

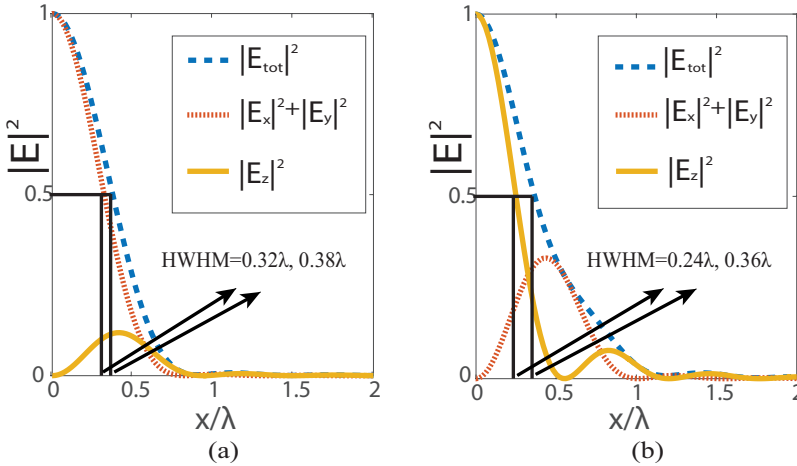


Figure 2.3: Profiles of the squared amplitude of the longitudinal and transverse components and total energy density $|\mathbf{E}|^2$ in the focal plane in the case of a pupil field that is linearly polarized in the x -direction (a) and a pupil field that is radially polarized (b). The focusing lens has $\text{NA}=0.9$. The plots are normalized to the on-axis peak values.

of the focal spots obtained in the case of radially polarized illumination with full aperture, annular aperture and optimized radially polarized illumination, as described in Eqs. 2.17-2.24. The optimized pupil field has FWHM which is 5.4% smaller than that of the full aperture constant pupil field. The FWHM of the intensity distribution of the longitudinal component obtained by focusing a radially polarized beam using a ring mask function (with radius 90% of the total pupil) is even smaller than the above two cases. However, the expanding side lobes in the annular case is larger than for the full aperture and the optimized cases. But the energy in the focal region is of course much weaker in the annular case. The corresponding total intensities of the three different pupils are shown in Figure 2.4(b). From the values of the FWHM of the intensity, the size of the focal spots is: Full aperture > Optimized > Annular aperture with 90% blocked. This gives a conclusion that the narrower the longitudinal component is, the smaller focal spot can be obtained.

We use expressions Eqs. 2.35 and 2.41 (with/without a polarization convertor) to compute the normalized detector signal. In order to make full use of the longitudinal component, the electric dipole is set along the z -axis. A small pinhole is

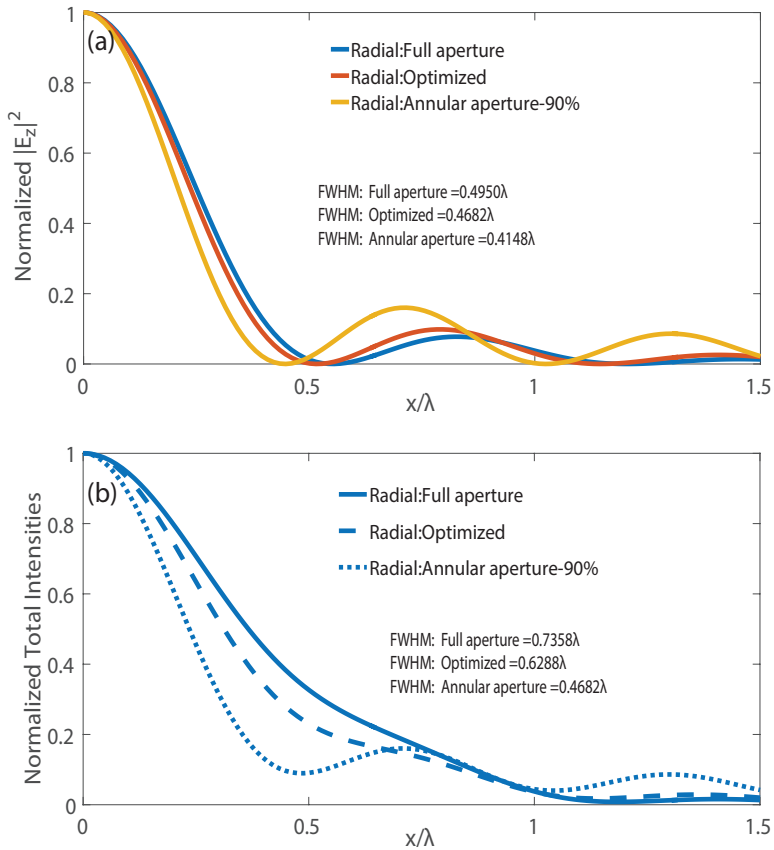


Figure 2.4: Profiles of longitudinal (a) and total (b) intensities of the exciting spot in the focal plane in the case of radially polarized illumination with full aperture, annular aperture and optimized radially polarized pupil field. The plots are normalized to their on-axis maxima.

taken into consideration in the confocal system [43] which helps for improving both lateral and axial resolution because of removing out-of-focus light. The smaller the pinhole is, the higher resolution can be achieved. However, with the decrease of the pinhole size, less light can pass through and the signal can be hardly collected by the detector. Therefore, the criterion for choosing a suitable pinhole size is to make an aperture giving 50% of the maximum intensity [44].

As is indicated in Fig. 2.1, we detect the intensity with a single-pixel camera at

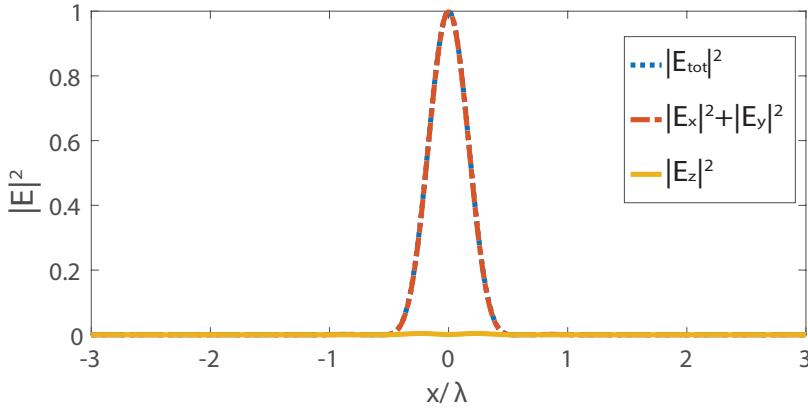


Figure 2.5: Profiles of the intensities at the detector plane with a polarization converter and a small pinhole with radius $r = 0.18\mu\text{m}$ which is 0.36λ in terms of wavelength. The system is composed of: a high $\text{NA}_1 = 0.9$ focusing objective lens and a low $\text{NA}_2 = 0.3$ lens for detection. For illumination, radially polarized light of wavelength $\lambda = 500\text{nm}$ is used. The focal field can be seen in Eq. 2.17. The dipole is set rigidly along the z -axis direction (only α_{zz} is relevant). The plots are normalized to on-axis maxima.

the focal point of the detector lens, which is located at $r = (0, 0, 0)$. However, if we assume purely longitudinal dipole excitation, then without polarization conversion, the intensity at the focal point is a local minimum, meaning that very little intensity is detected. To solve this problem, we propose to use a polarization converter in the pupil of the lens L_2 to change the radially polarized light to linearly polarized light, which in the focal plane will result in an intensity distribution with its maximum at the focal point. The intensity at the detector plane can be obtained by Eq. 2.41. Figure 2.5 shows the final signal along the x axis when the pinhole is set before the detector and the dipole is scanned in the x - y plane at the object plane. Note that because of the use of the polarization converter, the original radial polarization is turned into linear polarization and thus the “transversal” component in Fig. 2.5 corresponds to the contribution of the radially polarized light emitted by the dipole.

To validate that the system has the advantage of higher lateral resolution, two dipoles close to each other need to be analyzed with the above theory. Figure 2.6 shows the cross sections of the detected intensity when two dipoles that are parallel are scanned by a focused spot. The polarization of the illumination is taken as either linear, radial or optimized radial as shown in Eqs. 2.11 and 2.17-2.24. For linearly x -polarized illumination (diamond dot line), the dipoles are set along

the x -axis (only α_{xx} is relevant). If we want to roughly distinguish the two dipoles, the distance between them should be larger than 0.6λ according to the Rayleigh criterion. This value is approaching the diffraction limit $0.61 \frac{\lambda}{NA}$. However, for normal radial illumination (solid line), radial illumination with a ring mask (dashed line) and optimized radial illumination (dot line), with the dipoles set along the z -axis (only α_{zz} is relevant), the smallest distance at which they can be distinguished is reduced to 0.4λ . Meanwhile, the optimized one gives more obvious contrast than the normal radial case and the radial annular case gives the highest contrast. Even when the distance between the two dipoles decreases to 0.36λ , it can be seen that for the radial excitation with a ring mask and optimized radially polarized excitation, the two dipoles can be distinguished better than for the other two focused spots. Moreover, at this distance, note that in the case of linear polarization, the dipoles cannot be resolved.

The visibility as a function of d/λ can be seen in Fig. 2.7. Here the visibility is

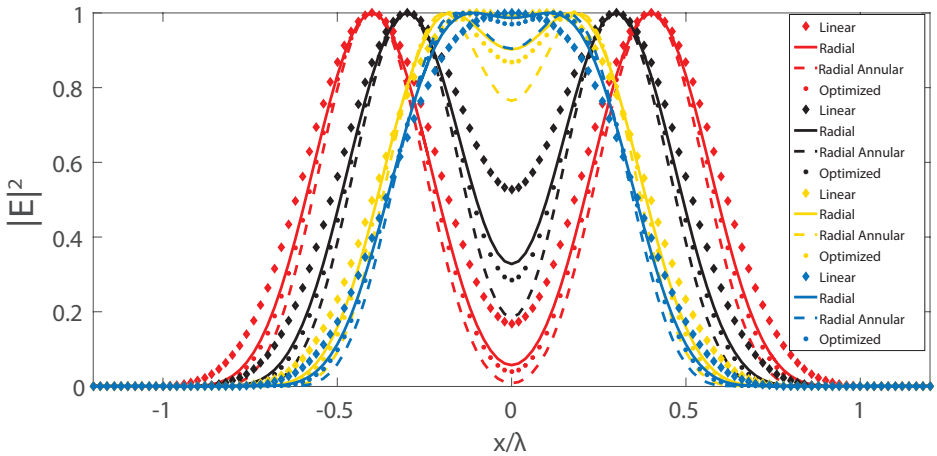


Figure 2.6: Profiles of the detected intensities as function of scanning distance of two separated dipoles for different kinds of illumination and for several distances between the dipoles. The system is composed of two lenses with $NA_1 = 0.9$, and $NA_2 = 0.3$ and is illuminated by light with a wavelength of $\lambda = 500nm$. The illumination is either linearly, radially or optimized radially polarized. The two dipoles are set along the x axis for the linear polarization and along the z axis for the other radially polarized cases. A polarization convertor is added in the case of radially polarized excitation. Four different distances between the dipoles are chosen: $d=0.8\lambda$ (red line), $d=0.6\lambda$ (black line), $d=0.4\lambda$ (yellow line), and $d=0.36\lambda$ (blue line). The plots are normalized to the on-axis peak intensity.

defined as:

$$\text{visibility} = \frac{I_{max} - I_{min}}{I_{max} + I_{min}}. \quad (2.44)$$

Here I_{max} is the normalized intensity which equals 1 and I_{min} is the value of the intensity at $r = (0, 0, 0)$ as shown in Fig. 2.6. When $d/\lambda > 1.2$, for the four cases, the two dipoles can be resolved very well. When $0.2 < d/\lambda < 1.2$, it is clearly seen that the visibility value of linear excitation is smaller than the other three cases,

which means the worst resolution. While the visibility value of radial excitation with the annular objective is the highest in this range. When $0.2 < d/\lambda < 0.3$, the resolution of the system is almost the same for the three radially polarized light excitation cases. When $d/\lambda < 0.2$, the dipoles can not be resolved any more in all cases because of the diffraction limit. This property of visibility agrees well with Fig. 2.6.

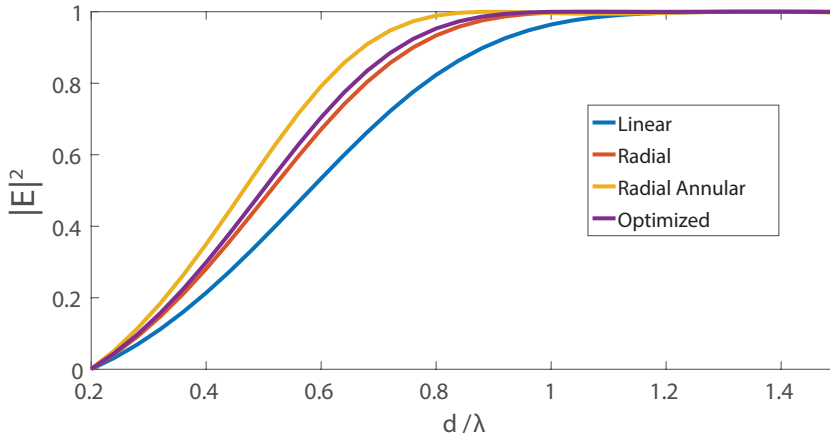


Figure 2.7: Profiles of the visibility as a function of the d/λ for the four cases of pupil fields. The system is the same as shown in Fig. 2.6.

2.5. Conclusion

In this chapter, we present a complete vectorial theoretical analysis to describe the whole imaging process of the high NA confocal system from the illumination point to the imaging plane. Strong longitudinal component as well as shaper focal spots are achieved by comparing the linear ($\text{FWHM}_{total}^{lin} \approx 0.76\lambda$) and radial ($\text{FWHM}_{total}^{rad} \approx 0.72\lambda$) polarization pupil fields. In order to obtain the higher resolution, we apply an optimized pupil field with an amplitude distribution that varies monotonically in the radial direction, which provides 5.4% tighter focused spot for $\text{NA} = 0.9$ than the full aperture constant pupil field. Additionally, the condition of radially polarized illumination with an annular objective lens is also considered to provide the smallest focal spot size, although at the expense of expanding side lobes.

Four kinds of focused spots are used to scan two parallel longitudinal dipoles with variable distances in the objective plane. In order to efficiently detect the field scattered by the longitudinally oriented dipoles, we insert a radial to linear polarization convertor before the pinhole. From our analysis, we show that for a pinhole in front of the detector with radius 0.36λ , by using a radial pupil field with the an annular lens to excite the dipoles, a distance of 0.36λ can be resolved, i.e., beyond the diffraction limit. The proposed method is easy to apply to other pupil fields and helpful to analyze confocal systems. The experiment can be conducted

on the basis of the theory and simulated results with different samples to validate the superiority of the optimized radially polarized illumination combined with the confocal system.

References

- [1] P. Meng, S. Pereira, and P. Urbach, *Confocal microscopy with a radially polarized focused beam*, *Optics Express* **26**, 29600 (2018).
- [2] S. W. Hell and J. Wichmann, *Breaking the diffraction resolution limit by stimulated emission: stimulated-emission-depletion fluorescence microscopy*, *Optics Letters* **19**, 780 (1994).
- [3] E. Betzig, G. H. Patterson, R. Sougrat, O. W. Lindwasser, S. Olenych, J. S. Bonifacio, M. W. Davidson, J. Lippincott-Schwartz, and H. F. Hess, *Imaging intracellular fluorescent proteins at nanometer resolution*, *Science* **313**, 1642 (2006).
- [4] M. J. Rust, M. Bates, and X. Zhuang, *Sub-diffraction-limit imaging by stochastic optical reconstruction microscopy (STORM)*, *Nature Methods* **3**, 793 (2006).
- [5] D. V. Patel and C. N. McGhee, *Contemporary in vivo confocal microscopy of the living human cornea using white light and laser scanning techniques: a major review*, *Clinical and Experimental Ophthalmology* **35**, 71 (2007).
- [6] A. Hoffman, M. Goetz, M. Vieth, P. Galle, M. Neurath, and R. Kiesslich, *Confocal laser endomicroscopy: technical status and current indications*, *Endoscopy* **38**, 1275 (2006).
- [7] S. Le Person, J. Puiggali, M. Baron, and M. Roques, *Near infrared drying of pharmaceutical thin films: experimental analysis of internal mass transport*, *Chemical Engineering and Processing: Process Intensification* **37**, 257 (1998).
- [8] S. Götzinger, L. de S Menezes, O. Benson, D. Talapin, N. Gaponik, H. Weller, A. Rogach, and V. Sandoghdar, *Confocal microscopy and spectroscopy of nanocrystals on a high- q microsphere resonator*, *Journal of Optics B: Quantum and Semiclassical Optics* **6**, 154 (2004).
- [9] K. Lindfors, T. Kalkbrenner, P. Stoller, and V. Sandoghdar, *Detection and spectroscopy of gold nanoparticles using supercontinuum white light confocal microscopy*, *Phys. Rev. Lett.* **93**, 037401 (2004).
- [10] L. Novotny and B. Hecht, *Principles of nano-optics* (Cambridge University) p. 104.
- [11] T. Wilson, R. Juškaitis, and P. Higdon, *The imaging of dielectric point scatterers in conventional and confocal polarisation microscopes*, *Optics Communications* **141**, 298 (1997).

- [12] R. Dorn, S. Quabis, and G. Leuchs, *Sharper focus for a radially polarized light beam*, *Phys. Rev. Lett.* **91**, 233901 (2003).
- [13] K. S. Youngworth and T. G. Brown, *Focusing of high numerical aperture cylindrical-vector beams*, *Optics Express* **7**, 77 (2000).
- [14] R. Chen, K. Agarwal, C. J. Sheppard, and X. Chen, *Imaging using cylindrical vector beams in a high-numerical-aperture microscopy system*, *Optics Letters* **38**, 3111 (2013).
- [15] S. Quabis, R. Dorn, M. Eberler, O. Glöckl, and G. Leuchs, *Focusing light to a tighter spot*, *Optics Communications* **179**, 1 (2000).
- [16] C. J. Sheppard and A. Choudhury, *Annular pupils, radial polarization, and superresolution*, *Applied Optics* **43**, 4322 (2004).
- [17] L. Yang, X. Xie, S. Wang, and J. Zhou, *Minimized spot of annular radially polarized focusing beam*, *Optics Letters* **38**, 1331 (2013).
- [18] Y. Kozawa and S. Sato, *Focusing property of a double-ring-shaped radially polarized beam*, *Optics Letters* **31**, 820 (2006).
- [19] H. Wang, L. Shi, B. Lukyanchuk, C. Sheppard, and C. T. Chong, *Creation of a needle of longitudinally polarized light in vacuum using binary optics*, *Nature Photonics* **2**, 501 (2008).
- [20] H. Guo, X. Weng, M. Jiang, Y. Zhao, G. Sui, Q. Hu, Y. Wang, and S. Zhuang, *Tight focusing of a higher-order radially polarized beam transmitting through multi-zone binary phase pupil filters*, *Optics Express* **21**, 5363 (2013).
- [21] F. Tang, Y. Wang, L. Qiu, W. Zhao, and Y. Sun, *Super-resolution radially polarized-light pupil-filtering confocal sensing technology*, *Applied Optics* **53**, 7407 (2014).
- [22] N. Davidson and N. Bokor, *High-numerical-aperture focusing of radially polarized doughnut beams with a parabolic mirror and a flat diffractive lens*, *Optics Letters* **29**, 1318 (2004).
- [23] H. Urbach and S. Pereira, *Field in focus with a maximum longitudinal electric component*, *Phys. Rev. Lett.* **100**, 123904 (2008).
- [24] K. Ushakova, Q. Van den Berg, S. Pereira, and H. Urbach, *Demonstration of spot size reduction by focussing amplitude modulated radially polarized light on a photoresist*, *Journal of Optics* **17**, 125615 (2015).
- [25] D. P. Biss, K. S. Youngworth, and T. G. Brown, *Dark-field imaging with cylindrical-vector beams*, *Applied Optics* **45**, 470 (2006).
- [26] W. T. Tang, E. Y. Yew, and C. J. Sheppard, *Polarization conversion in confocal microscopy with radially polarized illumination*, *Optics Letters* **34**, 2147 (2009).

- [27] X. Xie, Y. Chen, K. Yang, and J. Zhou, *Harnessing the point-spread function for high-resolution far-field optical microscopy*, *Phys. Rev. Lett.* **113**, 263901 (2014).
- [28] V. Ignatowsky, *Diffraction by a lens of arbitrary aperture*, *Trans. Opt. Inst* **1**, 1 (1919).
- [29] E. Wolf, *Electromagnetic diffraction in optical systems. i. an integral representation of the image field*, in *Proceedings of the Royal Society of London A: Mathematical, Physical and Engineering Sciences*.
- [30] B. Richards and E. Wolf, *Electromagnetic diffraction in optical systems. ii. structure of the image field in an aplanatic system*, in *Proceedings of the Royal Society of London A: Mathematical, Physical and Engineering Sciences*.
- [31] M. Abramowitz and I. A. Stegun, *Handbook of mathematical functions: with formulas, graphs, and mathematical tables*.
- [32] Q. Zhan and J. R. Leger, *Focus shaping using cylindrical vector beams*, *Optics Express* **10**, 324 (2002).
- [33] Q. Zhan, *Cylindrical vector beams: from mathematical concepts to applications*, *Advances in Optics and Photonics* **1**, 1 (2009).
- [34] W. Han, Y. Yang, W. Cheng, and Q. Zhan, *Vectorial optical field generator for the creation of arbitrarily complex fields*, *Optics Express* **21**, 20692 (2013).
- [35] Z. Chen, T. Zeng, B. Qian, and J. Ding, *Complete shaping of optical vector beams*, *Optics Express* **23**, 17701 (2015).
- [36] Z. Rong, Y. Han, S. Wang, and C. Guo, *Generation of arbitrary vector beams with cascaded liquid crystal spatial light modulators*, *Optics Express* **22**, 1636 (2014).
- [37] V. D'ambrosio, F. Baccari, S. Slussarenko, L. Marrucci, and F. Sciarrino, *Arbitrary, direct and deterministic manipulation of vector beams via electrically-tuned q-plates*, *Scientific Reports* **5**, 1 (2015).
- [38] Z. Liu, Y. Liu, Y. Ke, Y. Liu, W. Shu, H. Luo, and S. Wen, *Generation of arbitrary vector vortex beams on hybrid-order poincaré sphere*, *Photonics Research* **5**, 15 (2017).
- [39] D. Naidoo, F. S. Roux, A. Dudley, I. Litvin, B. Piccirillo, L. Marrucci, and A. Forbes, *Controlled generation of higher-order poincaré sphere beams from a laser*, *Nature Photonics* **10**, 327 (2016).
- [40] X. Hao, C. Kuang, T. Wang, and X. Liu, *Phase encoding for sharper focus of the azimuthally polarized beam*, *Optics Letters* **35**, 3928 (2010).
- [41] Y. Kozawa and S. Sato, *Dark-spot formation by vector beams*, *Optics Letters* **33**, 2326 (2008).

- [42] J. Jackson, *Classical Electrodynamics, 2nd edition* (John Wiley & Sons).
- [43] P. Török, P. Higdon, and T. Wilson, *Theory for confocal and conventional microscopes imaging small dielectric scatterers*, *Journal of Modern Optics* **45**, 1681 (1998).
- [44] D. B. Murphy, *Fundamentals of light microscopy and electronic imaging* (John Wiley & Sons).

3

Experimental demonstration of resolution enhancement with modulated radially polarized light

Lateral resolution enhancement is demonstrated in a confocal imaging system with amplitude-modulated radially polarized (RP) light at the wavelength $\lambda=632\text{nm}$. Annular pupil fields and optimized amplitude distribution functions can be realized with a spatial light modulator (SLM). By comparing images obtained with full and amplitude modulated apertures of RP illuminations using a high numerical aperture ($NA=0.9$), spatial resolution of $d=0.358\lambda$ has been achieved experimentally. This result agrees very well with theoretical simulation results and will be helpful in improving performance of the non-fluorescent imaging systems.

3.1. Introduction

Radially polarized (RP) beams have attracted increasing interest due to the unique focusing properties. In the previous work, it has been shown that a RP beam focused by a high NA objective can generate a sharp focal spot because of its strong longitudinal component near focus [2–5], which has potentials in practical applications such as optical tweezers and manipulation [6–8], optical data storage [9], accelerators [10] and super-resolution microscopy [11–14]. However, one limitation is that although the longitudinal component dominates in three components of the focal field, the transverse component still exists and has a donut shape. The transverse component affects the optical process, especially the imaging quality. Therefore, an appropriately shaped focal spot is essential in many applications such as optical recording, photolithography and microscopy. Intensive efforts on phase, polarization and amplitude modulation [15–17] of the pupil field have been made to modify the relative ratio between longitudinal and transverse components of the intensity distribution in focus. One simple method is using an annular aperture pupil field to obtain a tighter focusing spot in a high NA system with RP beam illumination, although this happens at the expense of stronger side lobes [18, 19]. It is shown that the longitudinal component of the focused spot can be, depending on the NA, 15% to 30% less than that of the classical Airy spot when shaping the amplitude of the RP pupil field that increases monotonically as a function of the pupil radius [20]. Spot-size reduction by means of focusing such an optimized RP beam with a high NA objective on a photoresist is confirmed experimentally and agrees with the theoretical analysis [21, 22].

Conventional confocal imaging system is a very commonly used microscopic technique, especially in the research field of biology. Due to advantages of laser excitation, high resolution and 2D sections, it is widely applied in biological fluorescent samples. However, the lateral resolution is limited by the Abbe diffraction limit. Our motivation for this chapter is to implement amplitude modulated RP beam in a confocal imaging set-up. This will provide general guidance for developing a higher resolution confocal imaging system, which can be not only applied for imaging biological objects but also for nanostructures.

3.2. Experimental set-up

3.2.1. General description

The experimental confocal set-up is shown in Fig. 3.1(a). The incident He-Ne laser ($\lambda=632nm$) passes through a single mode fibre and at the output of the fibre the laser is collimated into a large beam of about 8 mm diameter. The intensity distribution of the laser light is shaped by polarizers and SLM, with the latter being a reflected amplitude-only Holoeye LC-R2500. The first polarizer is to produce linearly polarized light from the unpolarized light and should be aligned with the orientation of liquid crystal molecules in the SLM to maximum the reflectance. The light after modulation passes through the second polarizer between the two BSs, which should be cross-polarized for the required amplitude modulation. After that, a liquid-crystal polarization convertor (THORLABS Zero-Order Vortex Half-Wave Re-

tarder, as explained later in Chapter 3.2.3) is used to convert the beam from linear to radial polarization by rotating the linear polarization over an angle that depends on the azimuthal angle ϕ in the pupil. The purpose of adding a $4f$ system between the SLM and the objective lens is to avoid the diffraction of modulated light after long distance propagation. Therefore, the modulated pupil field stays the same at the back focal plane as the one produced by the SLM. Then, the RP beam is tightly focused by an objective (NA=0.9) lens on a sample supported on a substrate. The detected sample is placed on a piezo-electric actuator operating by stepping in the $x-y$ plane within its linear range. The reflected light goes back to the convertor to convert the light back to linear polarization so that the signal can be easily detected in the confocal system [23, 24]. The final signal is detected after being filtered by the linear x polarizer which can improve the image contrast and then collected by a single mode fiber (THORLABS SM600). The fiber with a lens of small NA acts as a pinhole to make an aperture giving 50% of the maximum intensity [25], which is necessary in the confocal microscope. The detector is a silicon photodiode coupled into a low noise amplifier. The laser exposure time and the position of the scan table are controlled with the LabView software.

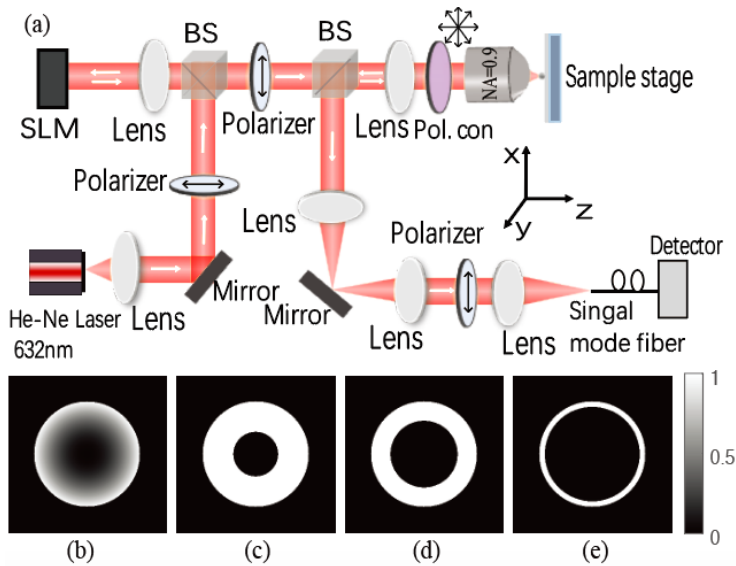


Figure 3.1: Scheme of the confocal imaging set-up with RP beam excitations (a). SLM modulated amplitude functions: optimized amplitude (b), ring aperture $0.38 < NA < 0.9$ (c), $0.57 < NA < 0.9$ (d), and $0.81 < NA < 0.9$ (e). The grey level represents the amplitude of light (in reflection). Abbreviations: beam splitter (BS), spatial light modulator (SLM), polarization convertor (Pol. con).

3.2.2. Amplitude modulation

There are two ways to realize the annular pupil as indicated in Eq. 2.24. One is to use the hard customized ring mask as seen in Fig. 3.2(a), the other is realized with the SLM as seen in Fig. 3.2(b). As we consider three annular apertures with

different ring size, the set-up changes once we change the hard ring mask from one size to another. Therefore, we use a SLM device to get the modulated pupil fields as discussed in Eqs. 2.20 and 2.24.

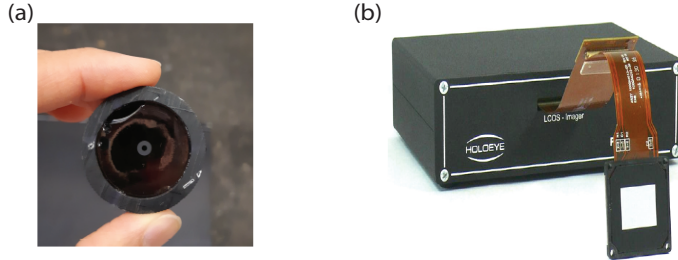


Figure 3.2: Hard ring mask (a) and amplitude reflective SLM (b) [26].

The working principle of SLM is based on the interaction of liquid crystal molecules with light, and subsequent transformation of light characteristics such as amplitude, phase and polarization. Liquid crystal (LC) molecules are polar molecules, possessing an axis. It is possible to position LC molecules in an organized way such that the light of particular polarization with respect to their polarization axis is reflected or transmitted whereas the light of the perpendicular polarization is not. The SLM used is LC-R2500 from Holoeye, which is easy-to-use and based on a reflective liquid crystal on silicon (LCoS) micro-display. It can be used to modulate light spatially in amplitude and phase, where the modulation function can be electrically addressed by a computer. The SLM has a 1024×768 resolution and 256 gray values. Basically, 1024×768 pixels of a picture of a maximum number of 256 gray levels is sent by means of the software to the device to manage the position of the LC molecules in space inside each pixel (pixel pitch is $19 \times 19 \mu m^2$). Each gray level is associated with a certain voltage value that is applied to the LC cell. However, the gray level does not react linearly to an applied voltage. The target image is mapped to a set of voltages via a gamma correction curve onto the SLM driver unit [27]. Gamma correction compensates the non-linear electro-optical transfer function of the displays. A special configuration of two polarizers should be considered, the first before and the second after the SLM, to enable the controllable amplitude modulation of the light beam. These alignment and polarizers positioning procedures are compulsory to ensure a correct position of the polarization axis of the light in respect to the axis of the LC molecules in the maximum and minimum values of the associated gray levels and to have the largest possible range of modulation.

The optimum amplitude function given by Eqs. 2.20-2.21 and the annular shaped mask which blocks the center of the beam up to $NA=0.38$ (42%), 0.57 (63%) and 0.81 (90%) described in Eq. 2.24 are shown in Figs. 3.1(b)-(e), respectively. All these modulated pupil fields can be realized by the SLM. The example of three modulated annular pupils corresponding to Figs. 3.1(c)-(e) in the back focal plane is given by Fig. 3.3.

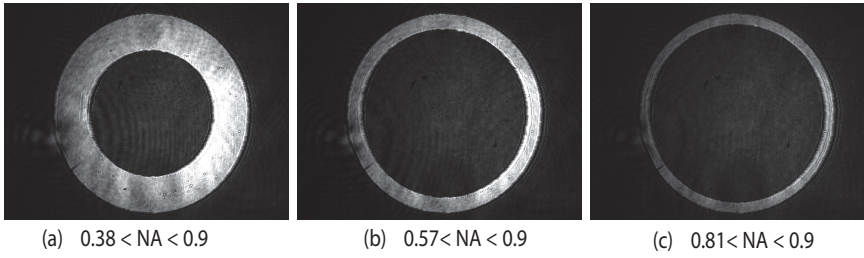


Figure 3.3: Measured amplitude distributions in the back focal plane after modulating the annular functions.

3.2.3. Polarization convertor

There are various methods to design a structured RP pupil, such as binary phase masks [16], reversing the electrical dipole array radiation at the focus [28–30], interferometric techniques [31], using optical fibers [32, 33] and space variant gratings [34, 35]. Although interferometric methods provide high quality radially polarized light, they imply usage of bulky set-ups. The polarization convertor (THORLABS Zero-Order Vortex Half-Wave Retarder $m=1$) we use is a liquid crystal device matching the operational wavelength, which generates radially or azimuthally polarized pattern from linearly polarized light depending on the incident polarization [36]. m is the number of complete polarization rotations per full azimuthal rotation. The orientation of the considered linearly polarized light ϕ depends only on the azimuthal angle θ and can be expressed as

$$\phi(\theta) = m \cdot \theta + \phi_0, \quad (3.1)$$

where ϕ_0 is a bias polarization orientation for $\theta=0$. $m = 1$, namely $\phi(\theta) = \theta$ and $\phi(\theta) = \theta + \pi/2$ represent radially and azimuthally polarized light. Figure 3.4 illustrates the generation of the two polarization modes with a θ -cell. The θ -cell represents an LC cell with a spatially varying twist angle, which is the heart of the convertor [37]. The linearly polarized light, hitting first the unidirectional alignment layer, with the polarization direction oriented parallel (or perpendicular) to the cell axis will emerge as linearly polarized light oriented parallel (or perpendicular) to the circular alignment layer. The described θ -cell is thus able to convert linearly polarized light into azimuthally or radially polarized light or vice versa. The polarization convertor is not only easy-to-use, but also it can convert the light back to linear polarization from the back side, which helps the signal detection [24].

To obtain a high quality radially polarized beam, the polarization convertor must be well-aligned. To do so, a coupled charge device (CCD) camera is used to observe the beam shape while moving the screw of the convertor manually until the two dark dots merge to one bright dot as shown in Fig. 3.5(a)-(b). The detection of the spatial distribution of the longitudinal field in the focal plane is not easy. In the literature, using a quantum well hetrostructures is proposed to study the longitudinal electric field [38] and with fluorescent single molecules, the longitudinal component is also possible able to analyze [39]. However, given the unavailability

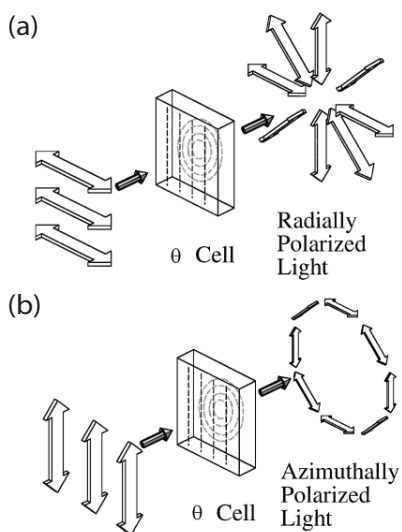


Figure 3.4: Generation of radially (a) and azimuthally polarized (b) light by use of a θ cell [36].

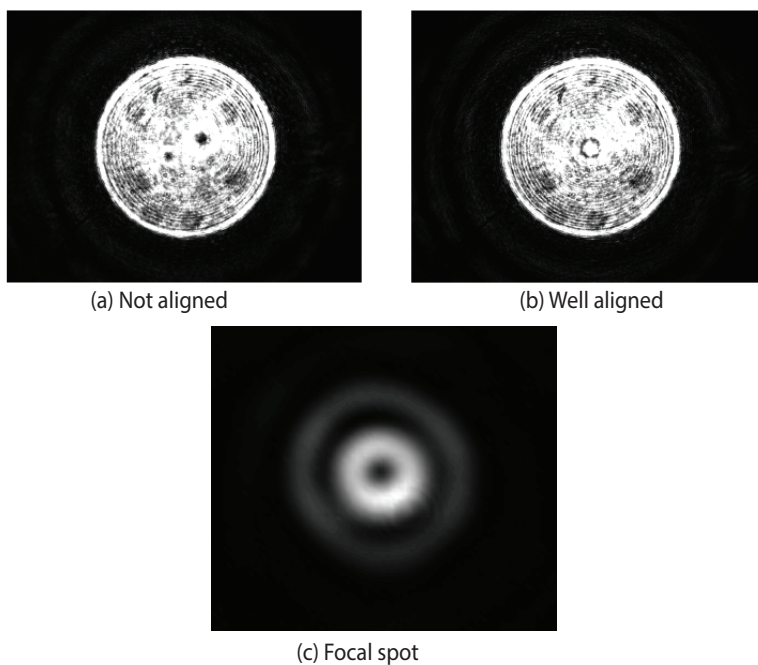


Figure 3.5: Alignment of the polarization convertor (a)-(b), and the radially polarized focal spot (c).

of such detection system, practically only the transverse field is detected. Once the polarization convertor is aligned well, we can focus the radially polarized beam using a high NA ($NA=0.9$) objective lens and re-image it with a low NA lens to demonstrate the focusing performance of the beam. The donut shaped transversal field component of the focused spot is recorded by a CCD camera shown in Fig. 3.5(c). Judging from the symmetry of the transversal component at focus, one can assure that the phase, intensity and polarization is well shaped in the pupil and conclude that the obtained focal spot is of high quality.

3.2.4. Detection

A single mode fiber Thorlabs SM600 with a cladding diameter of $125\ \mu\text{m}$ and mode field diameter of $3.6\text{-}5.3\ \mu\text{m}$, working in the operating wavelength range of $632\text{-}780\ \text{nm}$ is chosen to transmit the signal. The small aperture of the optical fiber acts as a pinhole, which is necessary in a confocal imaging system as previously introduced and the NA is between $0.10\text{-}0.14$. As the aperture of the lens in the fiber is really tiny, we need to correctly adjust the orientation of the coupling light with the help of the micro-metric screws so that the maximum signal is collected. The fiber is connected to a low-noise current pre-amplifier and the amplified signal can be observed with an oscilloscope. During the scanning process, the values of the collecting voltage should be in the range of $0\text{-}5\text{V}$ and cannot saturate.

3.2.5. LabView program

Once the fiber is correctly aligned, a LabView program is built in order to do the scanning automatically. The program operates in a loop-like fashion, which can be controlled by setting the array dimensions $N \times M$, the initial exposure time t , the linear increase in exposure time Δt per column step, the distance between two spots $(\Delta x, \Delta y)$, and stopping the platform for a time of approximately 1s to ensure that the piezo element has stopped vibrating. An example of the LabView interface is shown in Fig. 3.6. It can be seen that it is an efficient way to record data, because only the initial parameters and the step sizes need to be stored. The sample is at the focal plane so that the assumed focal position corresponds to $z = 0$. The detailed algorithm of the LabView program is attached in [Appendix B](#).

3.3. Experimental results and discussions

Before giving the imaging examples, here we firstly give the theoretical results of normalized total intensities in the focal plane for RP beams with different pupils and linear illuminations in Fig. 3.7. Although this figure is similar to Fig. 2.4, Chapter 2, here it is more specific and the optimized pupil matches well with the later produced in the experiment. Figure 3.7 shows the advantage of modulating the amplitude of the pupil. Considering the normalized total intensity distribution with $NA=0.9$ at focus, $\text{FWHM} \approx 0.7514\lambda$ of the spot size with linearly y polarized illumination, while $\text{FWHM} \approx 0.5186\lambda$ for the case of linearly x polarized illumination. However, the optimized pupil function has a FWHM of total intensity 0.434λ , which is 16.3% smaller than the case of conventional RP beam. By blocking 90% in terms of the pupil

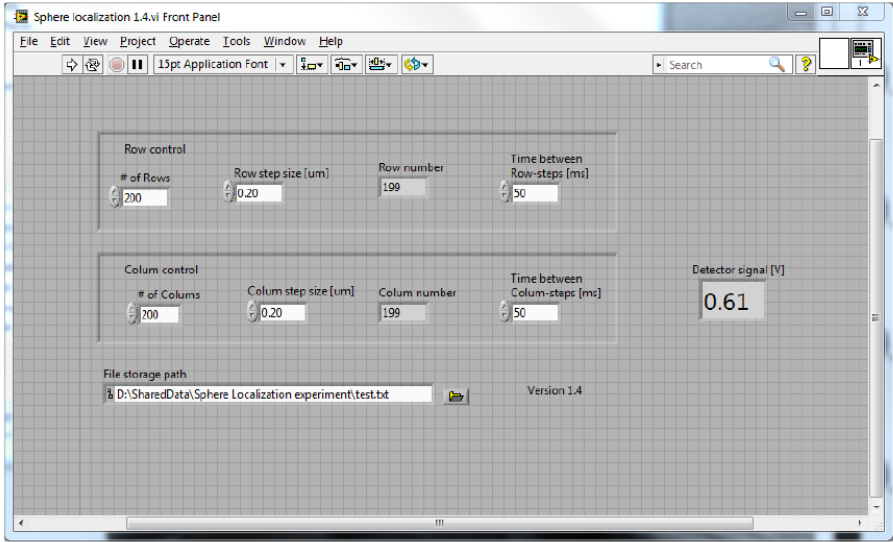


Figure 3.6: Example of a LabView interface.

radius from the center, the value of the FWHM reduces to 0.3916λ , almost 24.5% sharper than the unmodulated conventional RP beam. In our previous theoretical work, we regard subwavelength particles as electric dipoles. And to make full use of the narrow longitudinal component of the RP beam, two nearby dipoles with longitudinal dipole vectors are considered. It is demonstrated that the smallest distinguished distance of the two ideal longitudinal dipoles is 0.36λ with both annular and optimized pupil fields, i.e., beyond the diffraction limit of 0.68λ . However, for the annular pupil field, the light only propagates through the 10% unblocked area. As a consequence, the signal is very weak in the experiment. Strong side lobes can be produced in focus, which has negative influence on imaging a non-isolated object.

The sample we used to demonstrate superresolution is composed of random structures of paint on a glass substrate ($n_{\text{glass}}=1.5$) covered with a very thin layer ($\sim 20\text{nm}$) of Titanium dioxide (TiO_2 , $n_{\text{TiO}_2}=2.3897$) on the top of it. The thin layer functions as a substrate with guided mode excitation to further enhance the resolution and sensitivity [40–42]. The effect of the thin TiO_2 will be discussed in the next chapter in details. A wide view of the sample provided by the digital microscope KEYENCE VHX-6000 is shown in Fig. 3.8 with the magnification $\times 30$. The area in the red dashed box amplified as an inset is the final research target, which is zoomed in by 2000 times in Fig. 3.8(b). Here we need to draw attention to the magnification defined by KEYENCE microscope, which is very high and thus different from the normal optical magnification. In fact, there is a multiplication factor of ~ 22 after the calibration. One group of strips which can be distinguished are separated by $d=1.49\lambda$. Figures 3.8(c)–(g) display the images of the area obtained

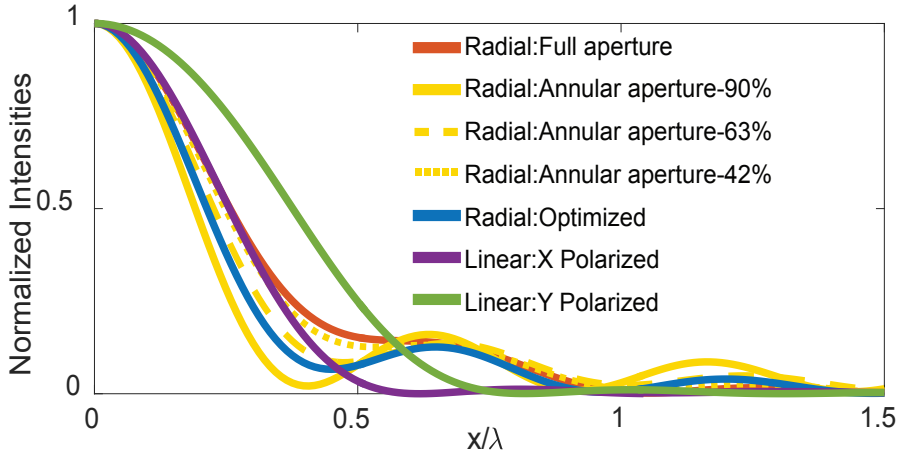


Figure 3.7: Theoretical results of normalized total intensities of in the focal plane for the RP beam with the pupil field of full aperture (red), annular aperture with 90% blocked ring (yellow) in terms of radius, optimized aperture (blue), linearly (purple: along x axis, green: along y axis) polarized illumination when the objective NA=0.9.

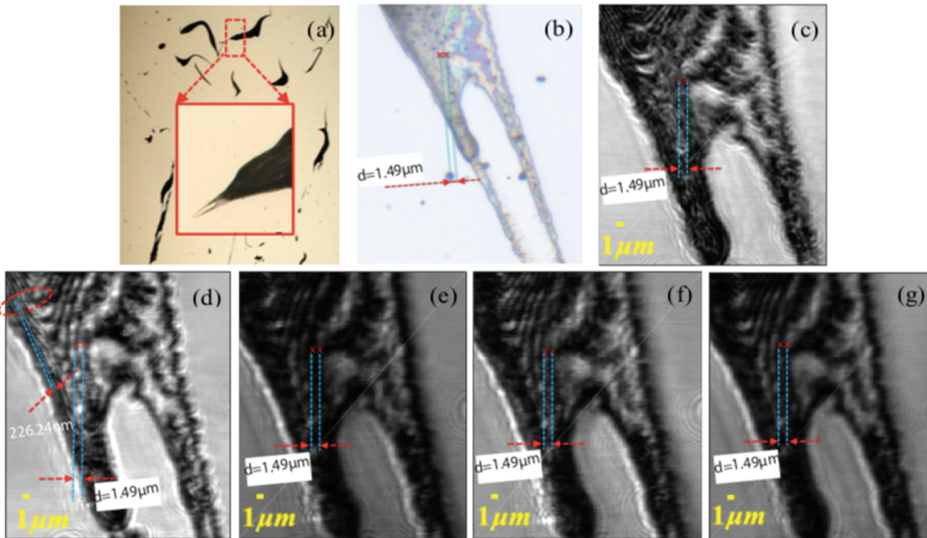


Figure 3.8: Images of a sample mounted on a substrate resolved by the digital microscope (a) in the wide field view with magnification $\times 30$ and (b) $\times 2000$, and by the improved confocal imaging system with different excitations of RP beams (c) conventional, (d) with optimized amplitude pupil field, and annular pupil fields with (e) 42% blocked, (f) 63% blocked, and (g) 90% blocked.

by our confocal imaging system with the excitations of a scanning focused spot corresponding to the conventional RP beam (c), to the optimized RP beam (d) and the annular mask with 42% (e), 63% (f) and 90% (g) of the light being blocked. The stripes with various distances in the structure are useful to determine the spatial resolution. The marked stripes with a distance of in Fig. 3.8(b) can be seen in all the images obtained with the amplitude modulated RP beams (Fig. 3.8(d)-(g)), except in the case of the conventional RP beam (Fig. 3.8(c)). In Fig. 3.8(d), after the sample illuminated by the RP beam with the optimized pupil field as described in Eqs. 2.20-2.21, even the distance of $226.24nm(d=0.358\lambda)$ between two stripes can be observed clearly. The highly resolved distance agrees well with the resolution of $d=0.36\lambda$ as mentioned in our previous theoretical calculation [23]. For the annular pupil fields, the medium size of the ring aperture (63% blocked) gives the best imaging result. This is reasonable, since with the increase of the blocked area (Fig. 3.8(g)), the effect of the side lobes becomes significant. Therefore, in the experiment, the image quality is not so good with the illumination of the RP beam of the annular aperture (90% blocked) as predicted in the simulations. Another important reason is that the sample is not the ideal longitudinal dipole anymore in the experimental work. Although the image quality in Fig. 3.8(e) with 42% of the pupil light being blocked is worse than the other two annular aperture cases (Figs. 3.8(f) and (g)), it is better than the unmodulated conventional condition (Fig. 3.8(c)). Therefore, the RP beam with the optimized amplitude of pupil field gives the most amount of detailed information and the best resolution. The RP beam with the pupil field of an annular ring also has advantages in the application of imaging, but the size of the ring mask should be chosen properly.

Figure 3.9 shows another larger scanning area ($40\mu m \times 40\mu m$) of the sample with five different RP beam illuminations. The scanning is with a step size of $0.2\mu m$. It is not difficult to see that the optimized and annular RP beam excitation in Fig. 3.9(b) and (d) give the best resolutions among the five conditions (Figs. 3.9(a)-(e)), especially at the center part of the black-white stripes. In order to quantify the quality of the image, we use the visibility defined by:

$$visibility = \frac{I_{max} - I_{min}}{I_{max} + I_{min}}, \quad (3.2)$$

with I_{max} and I_{min} the maximum and minimum normalized intensities. The higher the visibility is, the better image quality is achieved. Figure 3.9(f) presents the normalized signal distributions at the position of yellow dashed line labeled P1 as shown in Fig. 3.9(b), and also at the same position for other four conditions. The main reason to choose this position is that, in Figs. 3.9(b) and (d), the stripes can be found, but in other three images, these stripes cannot be observed clearly. Thus, this position is interesting and worth to analyze with the visibility. The fluctuations in Fig. 3.9(f) are related to the dark and bright stripes in the subplots. It can be found that there are some position shifts of the peaks and valleys in five conditions due to the scanning of the sample. The sample is difficult to keep going back to the same original position. Thus we compute the average visibility in the certain range shown in Fig. 3.9(f) and they are 0.2599 (blue), 0.7196 (red), 0.3127 (yellow),

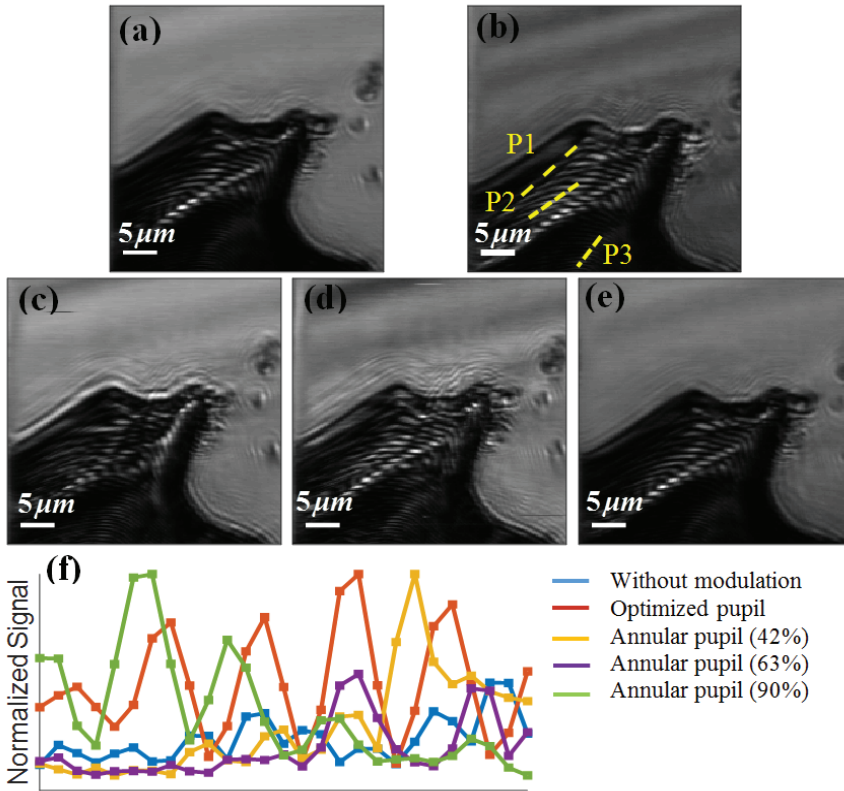


Figure 3.9: Images of another scanning area of the sample mounted on a substrate resolved by the improved confocal imaging system with different excitations of RP beams (a) conventional, (b) with optimized amplitude pupil field, and annular pupil fields with (c) 42% blocked, (d) 63% blocked, and (e) 90% blocked. Cross sections are shown in (f) to make comparisons of the visibility in above five cases.

0.5731 (purple) and 0.5312 (green), respectively. The two lines labeled P2 and P3 as shown in Fig. 3.9(b) are also investigated. The corresponding average visibilities are listed in Table 3.1.

The method to quantify the resolution is to differentiate the measured intensity

Table 3.1: Average Visibilities for Different Modulated RP Beams

Position	Unmodulated	Optimized	42%	63%	90%
1	0.2599	0.7196	0.3127	0.5731	0.5312
2	0.2175	0.5959	0.3149	0.4775	0.3701
3	0.0116	0.0908	0.0237	0.0562	0.0228

with respect to position and the definition of the derivative is defined as following :

$$derivative = \sqrt{\left(\frac{\partial I}{\partial x}\right)^2 + \left(\frac{\partial I}{\partial y}\right)^2} \tag{3.3}$$

where I is the normalized intensity at each position. The case with highest derivative has the highest resolution. Through calculating the derivative along the dashed line P2 in five conditions. The average value is 0.0384 (without modulation), 0.0689 (optimized pupil), 0.0455 (annular pupil 42% blocked), 0.0573 (annular pupil 63% blocked) and 0.0462 (annular pupil 92% blocked). From the data, it is clear that the optimized RP pupil field can provide best image resolution and quality, which is much better than the unmodulated conventional RP pupil field. Annular RP pupil fields can improve the image quality compared to the conventional RP beam illumination to some extent. It is shown that with the medium sized ring, the quality of the image is the best. Thus, the size of the ring mask should be chosen properly before making use of it, as the effect of side lobes and the strength of the signal should be taken into account. This result is consistent with images presented in Fig. 3.8.

3.4. Conclusion

In this chapter, we show the effect of amplitude modulated RP beams in the resolution of a confocal imaging system. Our previous theoretical prediction in the previous Chapter 2 is confirmed experimentally. With a SLM, we have been able to obtain the optimized pupil field and annular aperture pupil fields with different ring sizes of high quality, and shown that the performance of the confocal imaging system is improved, resulting in better image quality than that provided by the conventional RP beam. The smallest distinguishable distance of two nearby strips is $d=0.358\lambda$ in the experiment with the optimized RP beam, which is beyond the diffraction limit. Such results match very well with the simulated value $d=0.36\lambda$. Instead of considering the usual fluorescent samples, our experimental results apply to non-fluorescent samples. We believe that by combining the superiority of the amplitude modulated RP beam with the confocal imaging system should open up

an avenue for applying high resolved imaging technique in not only biological and medical research fields, but also other fields, such as nanostructure characterization.

References

- [1] P. Meng, H. Pham, S. F. Pereira, and H. P. Urbach, *Demonstration of lateral resolution enhancement by focusing amplitude modulated radially polarized light in a confocal imaging system*, *Journal of Optics* **22**, 045605 (2020).
- [2] S. Quabis, R. Dorn, M. Eberler, O. Glöckl, and G. Leuchs, *Focusing light to a tighter spot*, *Optics Communications* **179**, 1 (2000).
- [3] K. S. Youngworth and T. G. Brown, *Focusing of high numerical aperture cylindrical-vector beams*, *Optics Express* **7**, 77 (2000).
- [4] N. Davidson and N. Bokor, *High-numerical-aperture focusing of radially polarized doughnut beams with a parabolic mirror and a flat diffractive lens*, *Optics Letters* **29**, 1318 (2004).
- [5] Y. Kozawa and S. Sato, *Sharper focal spot formed by higher-order radially polarized laser beams*, *J. Opt. Soc. Am. A* **24**, 1793 (2007).
- [6] Q. Zhan, *Trapping metallic rayleigh particles with radial polarization*, *Optics Express* **12**, 3377 (2004).
- [7] M. Li, S. Yan, B. Yao, M. Lei, Y. Yang, J. Min, and D. Dan, *Trapping of rayleigh spheroidal particles by highly focused radially polarized beams*, *J. Opt. Soc. Am. B* **32**, 468 (2015).
- [8] W. Cui, F. Song, F. Song, D. Ju, and S. Liu, *Trapping metallic particles under resonant wavelength with 4 π tight focusing of radially polarized beam*, *Optics Express* **24**, 20062 (2016).
- [9] Y. Zhang and J. Bai, *Improving the recording ability of a near-field optical storage system by higher-order radially polarized beams*, *Optics Express* **17**, 3698 (2009).
- [10] C. Varin, S. Payeur, V. Marceau, S. Fourmaux, A. April, B. Schmidt, P.-L. Fortin, N. Thiré, T. Brabec, F. Légaré, J.-C. Kieffer, and M. Piché, *Direct electron acceleration with radially polarized laser beams*, *Applied Sciences* **3**, 70 (2013).
- [11] Y. Kozawa, D. Matsunaga, and S. Sato, *Superresolution imaging via superoscillation focusing of a radially polarized beam*, *Optica* **5**, 86 (2018).
- [12] Y. Kozawa, T. Hibi, A. Sato, H. Horanai, M. Kurihara, N. Hashimoto, H. Yokoyama, T. Nemoto, and S. Sato, *Lateral resolution enhancement of laser scanning microscopy by a higher-order radially polarized mode beam*, *Optics Express* **19**, 15947 (2011).

- [13] Y. Kozawa and S. Sato, *Numerical analysis of resolution enhancement in laser scanning microscopy using a radially polarized beam*, *Optics Express* **23**, 2076 (2015).
- [14] F. Tang, Y. Wang, L. Qiu, W. Zhao, and Y. Sun, *Super-resolution radially polarized-light pupil-filtering confocal sensing technology*, *Applied Optics* **53**, 7407 (2014).
- [15] R. Dorn, S. Quabis, and G. Leuchs, *Sharper focus for a radially polarized light beam*, *Phys. Rev. Lett.* **91**, 233901 (2003).
- [16] H. Wang, L. Shi, B. Lukyanchuk, C. Sheppard, and C. T. Chong, *Creation of a needle of longitudinally polarized light in vacuum using binary optics*, *Nature Photonics* **2**, 501 (2008).
- [17] S. N. Khonina, S. V. Karpeev, S. V. Alferov, and V. A. Soifer, *Generation of cylindrical vector beams of high orders using uniaxial crystals*, *Journal of Optics* **17**, 065001 (2015).
- [18] C. J. R. Sheppard and A. Choudhury, *Annular pupils, radial polarization, and superresolution*, *Applied Optics* **43**, 4322 (2004).
- [19] L. Yang, X. Xie, S. Wang, and J. Zhou, *Minimized spot of annular radially polarized focusing beam*, *Optics Letters* **38**, 1331 (2013).
- [20] H. P. Urbach and S. F. Pereira, *Field in focus with a maximum longitudinal electric component*, *Phys. Rev. Lett.* **100**, 123904 (2008).
- [21] K. Ushakova, Q. Y. van den Berg, S. F. Pereira, and H. P. Urbach, *Demonstration of spot size reduction by focussing amplitude modulated radially polarized light on a photoresist*, *Journal of Optics* **17**, 125615 (2015).
- [22] M. Van, K. Ushakova, C. W. Bastiaansen, S. F. Pereira, H. P. Urbach, and D. J. Broer, *Enhanced lithographic resolution using longitudinal polarization state of light*, *Journal of Micro/Nanolithography, MEMS, and MOEMS* **14**, 043509 (2015).
- [23] P. Meng, S. Pereira, and P. Urbach, *Confocal microscopy with a radially polarized focused beam*, *Optics Express* **26**, 29600 (2018).
- [24] X. Xie, Y. Chen, K. Yang, and J. Zhou, *Harnessing the point-spread function for high-resolution far-field optical microscopy*, *Phys. Rev. Lett.* **113**, 263901 (2014).
- [25] D. B. Murphy, *Fundamentals of light microscopy and electronic imaging* (John Wiley & Sons, 2002).
- [26] *Image download from the website of holoeye*, <https://holoeye.com/spatial-light-modulators/discontinued-devices/>.

- [27] S. McDermott, P. Li, G. Williams, and A. Maiden, *Characterizing a spatial light modulator using ptychography*, *Optics Letters* **42**, 371 (2017).
- [28] J. Wang, W. Chen, and Q. Zhan, *Engineering of high purity ultra-long optical needle field through reversing the electric dipole array radiation*, *Optics Express* **18**, 21965 (2010).
- [29] J. Wang, Q. Liu, C. He, and Y. Liu, *Reversal construction of polarization-controlled focusing field with multiple focal spots*, *Optical Engineering* **52**, 1 (2013).
- [30] Y. Yu and Q. Zhan, *Creation of identical multiple focal spots with prescribed axial distribution*, *Scientific Reports* **5**, 14673 (2015).
- [31] C. Han, C. Ho, C. Kuo, and R. Chang, *Simple triangular path interferometer for generation of an inhomogeneously polarized beam*, *Japanese Journal of Applied Physics* **48**, 092402 (2009).
- [32] S. Ramachandran, P. Kristensen, and M. F. Yan, *Generation and propagation of radially polarized beams in optical fibers*, *Optics Letters* **34**, 2525 (2009).
- [33] W. Chen, W. Han, D. C. Abeysinghe, R. L. Nelson, and Q. Zhan, *Generating cylindrical vector beams with subwavelength concentric metallic gratings fabricated on optical fibers*, *Journal of Optics* **13**, 015003 (2010).
- [34] G. M. Lerman and U. Levy, *Generation of a radially polarized light beam using space-variant subwavelength gratings at 1064 nm*, *Optics Letters* **33**, 2782 (2008).
- [35] Z. Bomzon, V. Kleiner, and E. Hasman, *Formation of radially and azimuthally polarized light using space-variant subwavelength metal stripe gratings*, *Applied Physics Letters* **79**, 1587 (2001).
- [36] M. Stalder and M. Schadt, *Linearly polarized light with axial symmetry generated by liquid-crystal polarization converters*, *Optics Letters* **21**, 1948 (1996).
- [37] R. Yamaguchi, T. Nose, and S. Sato, *Liquid crystal polarizers with axially symmetrical properties*, *Japanese Journal of Applied Physics* **28**, 1730 (1989).
- [38] G. Kihara Rurimo, M. Schardt, S. Quabis, S. Malzer, C. Dotzler, A. Winkler, G. Leuchs, G. Döhler, D. Driscoll, M. Hanson, et al., *Using a quantum well heterostructure to study the longitudinal and transverse electric field components of a strongly focused laser beam*, *Journal of Applied Physics* **100**, 023112 (2006).
- [39] L. Novotny, M. R. Beversluis, K. S. Youngworth, and T. G. Brown, *Longitudinal field modes probed by single molecules*, *Phys. Rev. Lett.* **86**, 5251 (2001).
- [40] S. Roy, S. F. Pereira, H. P. Urbach, X. Wei, and O. El Gawhary, *Exploiting evanescent-wave amplification for subwavelength low-contrast particle detection*, *Phys. Rev. A* **96**, 013814 (2017).

- [41] O. El Gawhary, M. Dheur, S. Pereira, and J. Braat, *Extension of the classical fabry–perot formula to 1d multilayered structures*, [Applied Physics B](#) **111**, 637 (2013).
- [42] S. Roy, K. Ushakova, Q. van den Berg, S. F. Pereira, and H. P. Urbach, *Radially polarized light for detection and nanolocalization of dielectric particles on a planar substrate*, [Phys. Rev. Lett.](#) **114**, 103903 (2015).

4

Super-resolution effect due to a thin dielectric slab for imaging with radially polarized light

Improving the imaging of small particles is a classic problem and especially challenging when the distance between particles are below the optical diffraction limit. We propose an imaging system illuminated with radially polarized light combined with a suitable substrate which contains a thin dielectric layer to demonstrate that imaging ability of particles that are placed close together can be enhanced. The coupling between the evanescent wave produced in a designed thin dielectric layer, the small particles and the propagating wave, forms a mechanism to transfer sub-wavelength information about the particles to the far field. The smallest distinguished distance reaches to 0.634λ , when the imaging system is composed of a high numerical aperture ($NA=0.9$) lens and the illumination wavelength $\lambda=632\text{nm}$, beyond the diffraction limit 0.678λ . The lateral resolution can be further improved by combining the proposed structure with super-resolution microscopy techniques.

4.1. Introduction

Conventional imaging using lenses and mirrors are naturally limited by diffraction limit. This limit comes from the loss of high-resolution details in the far field. In general, a substrate is necessary for supporting the sample when observing with the microscope. A specially designed substrate containing a thin layer of some designed material and thickness on top of it can be helpful in improving the imaging performance. Veselago was the first to mention materials with negative refractive index [2]. Pendry demonstrated that besides focusing light, these materials would be able to enhance evanescent waves and lead to imaging beyond the diffraction limit [3]. It is then possible to achieve so-called super-resolution. However, negative refractive index materials are not available in nature and they cannot be artificially fabricated at optical frequencies. But Pendry further showed that in the electrostatic regime, metals can mimic those materials. Experimental confirmation of super-resolution with planar silver slabs are shown in Refs. [4, 5]. Although evanescent waves carry the information of high spatial frequency, they are confined to the near field and decay exponentially in a medium with positive permittivity and permeability and are lost before reaching the final imaging plane. Optical superlenses are designed to significantly enhance the evanescent waves and convert them into propagating waves that can be measured in the far field [6, 7]. It was found that a thin dielectric layer can restore evanescent waves as a silver lens does and realize super-resolution, with the advantage that it is easier to deposit thin layers without percolation issues observed for metals [8, 9]. A simple but complete system of evanescent-wave generation, amplification, and the consequent modulation of the far field was designed in Ref. [10]. The far field propagating waves containing information about sub-wavelength objects by coupling evanescent waves can be used in microscopy to recover sub-wavelength details.

In this chapter, we investigate the effect of evanescent waves for imaging sub-wavelength particles on a flat substrate coated with a very thin evanescent wave amplifying layer. In the section of theoretical model, the model is built by considering the subwavelength particle as an electric dipole. It is demonstrated analytically that the evanescent wave can be enhanced in the near field compared with the case of no enhanced layers in the section of simulation results and discussion. Also, we use numerical analysis based on a three-dimensional (3D) finite difference time domain (FDTD) method to simulate the near field distributions when one or two nanospheres are taken into account. The images of the spheres are reconstructed using the methods of angular spectrum and Fourier transform. Through the calculations, far field imaging quality of both signal-to-noise ratio (SNR) and lateral resolution can be enhanced in a simple designed structure. Finally, it can be summarized that the results can be easily applied in other imaging systems, hence immediately improving their performance.

4.2. Axial resolution

In the previous Chapters 2 and 3, we pay main attentions to the lateral resolution enhancement with the tightly focal spot. However, in many areas, and particularly

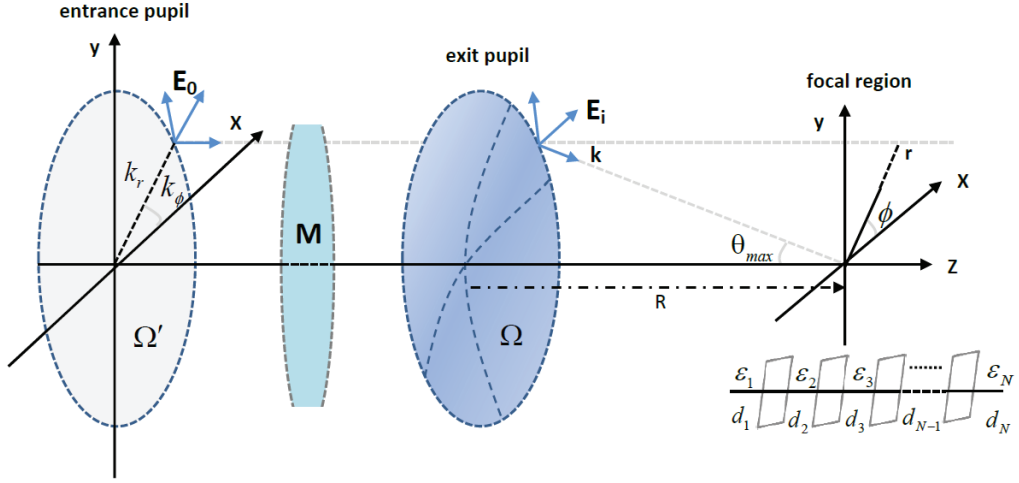


Figure 4.1: Schematic overview of an aplanatic imaging system. The field $\mathbf{E}_0(k_r, k_\phi, 0)$ in the entrance pupil Ω' is focused by the lens to the focal point. The focal field $\mathbf{E}_i(k_r, k_\phi, k_{zi})$ is obtained by an integration over the exit pupil distribution, where several medium transitions can be encountered at $z = d_i$. The first medium at the exit pupil has electric permittivity ϵ_1 and the final medium has electric permittivity ϵ_N .

in microscopy not only lateral but also axial resolution is important, since in many cases one is interested in a three-dimensional image of an object, such as confocal microscopy. In a confocal imaging system, the problem of poor axial resolution can be solved by setting a small pinhole at the detector plane. Even though this technique is a big breakthrough in 3D imaging, the considerable low efficiency due to the loss of light that is blocked by the pinhole limits its applications in some situations. Since we take the substrate into account in this chapter, we firstly present an example to demonstrate higher axial resolution is achieved by focusing RP beam on an interface.

The aplanatic imaging system with a numerical aperture NA and the coordinate system adopted here is shown in Fig. 4.1. The transition from the entrance pupil, disc defined by Ω' , to the exit pupil, a spherical shell defined by Ω can be considered as a rotation of the field vector around the angular axis ($\hat{\phi}$) in a cylindrical basis ($\hat{r}, \hat{\phi}, \hat{z}$). The general problem of focal fields on stratified media has been worked out earlier and the expression for the electric field distribution at focus is given by [11]

$$\mathbf{E}_i(\mathbf{r}) = -\frac{iR}{2\pi} \iint_{\Omega'} \frac{e^{irk_r \cos(k_\phi - \phi)}}{\sqrt{k_{z1}k_1}} \left[e^{ik_{zi}z} \mathbf{M}_i^+ + e^{-ik_{zi}z} \mathbf{M}_i^- \right] \cdot \mathbf{E}_0(k_r, k_\phi) k_r dk_r dk_\phi, \quad (4.1)$$

where the subscript i denotes the medium where the field is calculated, and $k_1^2 = k_{z1}^2 + k_r^2$ is the propagating vector of the first medium. The integration domain Ω' is restricted to $0 \leq k_\phi < 2\pi$ and $0 \leq k_r < \text{NA}k_0$. The propagation matrices \mathbf{M}_i^\pm for

the medium i are defined as

$$\mathbf{M}_i^\pm = \frac{1}{2} \begin{pmatrix} g_i^{0\pm} - g_i^{2\pm} \cos 2k_\phi & -g_i^{2\pm} \sin 2k_\phi & 0 \\ -g_i^{2\pm} \sin 2k_\phi & g_i^{0\pm} + g_i^{2\pm} \cos 2k_\phi & 0 \\ -g_i^{1\pm} \cos k_\phi & -g_i^{1\pm} \sin k_\phi & 0 \end{pmatrix}, \quad (4.2)$$

with the effective reflection and transmission coefficients in medium i for the TE (s) and TM (p) polarization components are given by

$$\begin{aligned} g_i^{0\pm} &= f_i^{s\pm} \pm f_i^{p\pm} \frac{k_{zi}}{k_i}, \\ g_i^{2\pm} &= f_i^{s\pm} \mp f_i^{p\pm} \frac{k_{zi}}{k_i}, \\ g_i^{1\pm} &= 2f_i^{p\pm} \frac{k_r}{k_i}, \end{aligned} \quad (4.3)$$

where the \pm sign denotes the field traveling in the forward or back ward directions.

When the incident radially polarized light (p polarized) is focused on the one layer interface, Eqs.4.1-4.3 can be simplified. And the field is propagated to the interface by the method of angular spectrum representation [12, 13]. The initial, reflected and transmitted fields are assumed and Maxwell's boundary conditions are applied to these fields [14, 15]. The results are

$$\mathbf{E}_f(\rho, z) = \int_0^{\theta_{max}} l_0(\theta) \mathbf{E}_f^\infty \cos^{1/2} \theta \sin \theta d\theta, \quad (4.4)$$

$$\mathbf{E}_r(\rho, z) = \int_0^{\theta_{max}} l_0(\theta) \mathbf{E}_r^\infty \cos^{1/2} \theta \sin \theta d\theta, \quad (4.5)$$

$$\mathbf{E}_t(\rho, z) = \int_0^{\theta_{max}} l_0(\theta) \mathbf{E}_t^\infty \cos^{1/2} \theta \sin \theta d\theta, \quad (4.6)$$

with

$$\mathbf{E}_f^\infty = e^{ik_1 z \cos \theta} \begin{pmatrix} i \cos \theta J_1(\rho k_1 \sin \theta) \\ 0 \\ -\sin \theta J_0(\rho k_1 \sin \theta) \end{pmatrix}, \quad (4.7)$$

$$\mathbf{E}_r^\infty = -r^p e^{-ik_1 z \cos \theta} e^{i2k_1 z_0 \cos \theta} \begin{pmatrix} i \cos \theta J_1(\rho k_1 \sin \theta) \\ 0 \\ \sin \theta J_0(\rho k_1 \sin \theta) \end{pmatrix}, \quad (4.8)$$

$$\mathbf{E}_t^\infty = -t^p e^{ik_1 z_0 \cos \theta} e^{ik_2 \sqrt{1 - \left(\frac{k_1}{k_2} \sin \theta\right)^2} (z - z_0)} \begin{pmatrix} i \sqrt{1 - \left(\frac{k_1}{k_2} \sin \theta\right)^2} J_1(\rho k_1 \sin \theta) \\ 0 \\ \frac{k_1}{k_2} \sin \theta J_0(\rho k_1 \sin \theta) \end{pmatrix}, \quad (4.9)$$

where k_1 and k_2 are the wavelength in the medium n_1 and n_2 , respectively. z_0 represents the interface position. The r_p and t_p are Fresnel reflection and transmission coefficients, which can be expressed as

$$\begin{aligned} r_p &= \frac{n_2 \cos \theta_1 - n_1 \cos \theta_2}{n_1 \cos \theta_2 + n_2 \cos \theta_1}, \\ t_p &= \frac{2n_1 \cos \theta_2}{n_1 \cos \theta_2 + n_2 \cos \theta_1}, \end{aligned} \quad (4.10)$$

An apodization function which describes the Bessel-Gauss beam [16] can be given

4

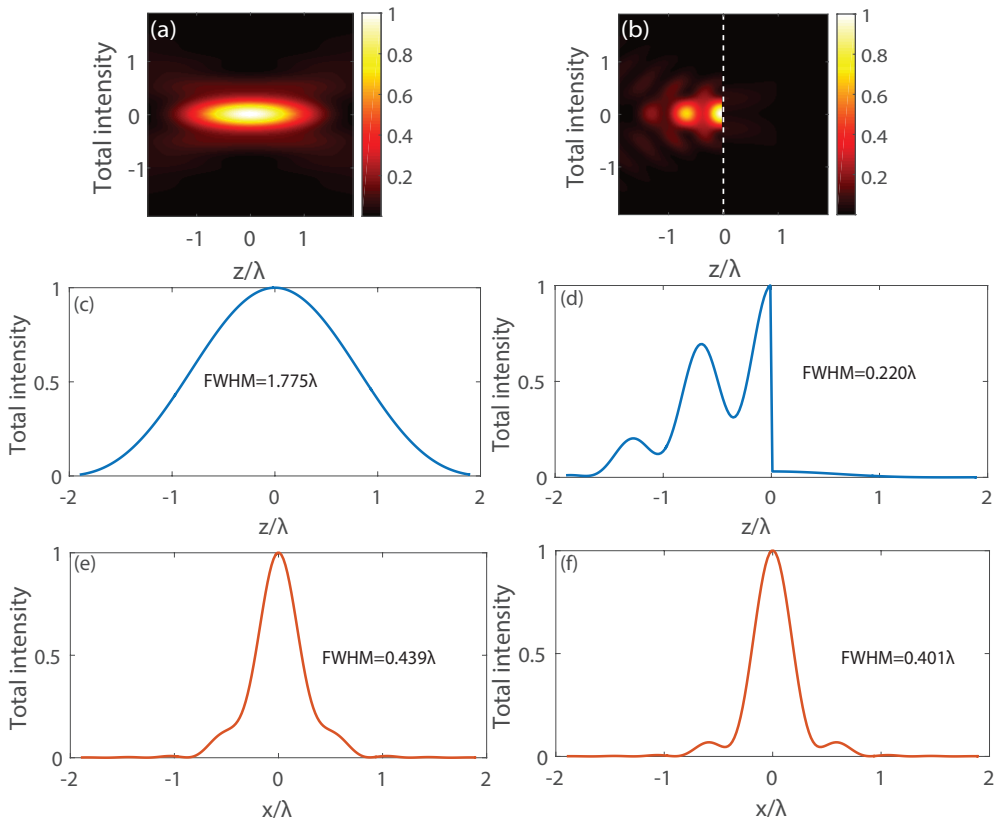


Figure 4.2: (a) Total electric field intensity in the focal region with $\text{NA}=0.9$. The input field is a radially polarized donut. (b) Same as (a) but with the addition of a TiO_2 substrate at the geometrical focus of the lens. (c) and (d) are the profiles of the total electric field intensity of (a) and (b) along the z axis at $x = 0$ respectively. (e) and (f) are the profiles of the total electric field intensity of (a) and (b) along the x axis at $z = 0$ respectively. The intensities are all normalized by the maximum intensity value.

by

$$I_0(\theta) = E_0 \exp\left(-\beta^2 \frac{\sin^2 \theta}{\sin^2 \theta_{max}}\right) J_1\left(2\beta \frac{\sin \theta}{\sin \theta_{max}}\right). \quad (4.11)$$

where θ_{max} is the maximum entering angle of the beam, and β is a ratio of the pupil radius to the entering beam radius. In the following example, we choose $\beta = 1$.

Figure 4.2(a) and (b) show a total field distribution at focus in the zx plane without and with the interface. The illumination is radially polarized light with the wavelength $\lambda=632nm$ and is tightly focused by an objective lens with $NA=0.9$. The refractive indices of the free space and the TiO_2 substrate is $n_1=1.0$ and $n_2=2.3897$, respectively. The position of the interface in at $z_0=0$, which is indicated by the white dashed line in Fig. 4.2(b). The cross sections of the focal fields along the z axis and x axis are shown in Figs 4.2(c)-(d) and (e)-(f). We see that the presence of the interface implies a reduction of the FWHM of the field intensity along the z axis from 1.775λ to 0.220λ and along the x axis from 0.439λ to 0.401λ . It is interesting to note that compared with the spot size in the lateral direction, the reduction in the z direction is much larger, which is clearly understood since destructive interference occurs between the incident and reflected fields. Sharper PSF in the z direction when a substrate is considered results in higher axial resolution, which is important for imaging a deep 3D object. The FWHM of the field along the x axis does not get narrower too much in the above example. The further optimization of the substrate is considered in the next section to improve the resolution in the lateral direction.

4.3. Lateral resolution

4.3.1. Evanescent wave and super-resolution

In electromagnetics, an evanescent wave is an oscillating electric and/or magnetic field that does not propagate as an electromagnetic wave but whose energy is spatially concentrated in the vicinity of the source. In optics, evanescent waves are formed when waves traveling in a medium undergo total internal reflection at its boundary because they strike it at an angle greater than the so-called critical angle [17]. In microscopy, systems that capture the information contained in evanescent waves can be used to create super-resolution images. To explain this principle, we discuss the problem of propagation of the time-harmonic plane waves $U(\mathbf{x}) = e^{i\mathbf{k}\cdot\mathbf{x}}$ from the plane $z = 0$ to some other plane [18]. Firstly, we decompose the field in the plane $z=0$ into two-dimensional (2D) plane waves:

$$U(x, y, 0) = \iint \hat{U}_0(f_x, f_y) e^{2\pi i(f_x x + f_y y)} df_x df_y, \quad (4.12)$$

where f_x and f_y are the spatial frequencies. Each plane wave has a weight $\hat{U}_0(f_x, f_y)$, and this function is called the angular spectrum of the field and one can see that U and \hat{U}_0 are related to each other by a 2D spatial Fourier transform. Then each plane wave should propagate separately to some plane z_0 . It is known that a 3D

plane wave is of the form $e^{i\mathbf{k}\cdot\mathbf{x}} = e^{i(k_x x + k_y y + k_z z)}$, where the wave vector has a fixed length $|\mathbf{k}| = k = \sqrt{k_x^2 + k_y^2 + k_z^2} = \frac{2\pi}{\lambda}$ that is determined by the wavelength. So we see that our 2D plane wave describes the 3D plane wave in the plane $z = 0$ if substituting $k_{x,y}$ with $2\pi f_{x,y}$. The longitudinal component of the wave vector k_z is then fixed up to its sign by the length of the wave vector k

$$k_z = \pm \sqrt{\left(\frac{2\pi}{\lambda}\right)^2 - k_x^2 - k_y^2}, \quad (4.13)$$

The sign of k_z is determined by whether the field propagates in the positive or negative z -direction, which depends on whether the sources of the field are located before or after the plane $z = 0$. This value for k_z determines for each 2D plane wave how it will propagate to any other plane. Finally, all the plane waves are added back together to find the total propagated field $U(x, y, z_0)$, and it can be expressed as

$$U(x, y, z_0) = \iint \hat{U}_0(f_x, f_y) e^{2\pi i \left(f_x x + f_y y + z_0 \sqrt{\left(\frac{1}{\lambda}\right)^2 - f_x^2 - f_y^2} \right)} df_x df_y, \quad (4.14)$$

Eq. 4.14 can also be written differently by using Fourier transforms

$$U(x, y, z_0) = \iint \mathcal{F}^{-1} \left\{ \mathcal{F}\{U(x, y, 0)\}(f_x, f_y) e^{2\pi i z_0 \sqrt{\left(\frac{1}{\lambda}\right)^2 - f_x^2 - f_y^2}} \right\} (x, y), \quad (4.15)$$

We Fourier transform the initial field to decompose it into plane waves, and then multiply the spectrum with a phase term, and at the end inverse Fourier transform the product to add all the waves together.

In the above result of the angular spectrum method, there is an evanescent wave. If $f_x^2 + f_y^2 > \left(\frac{1}{\lambda}\right)^2$, the expression $\sqrt{\left(\frac{1}{\lambda}\right)^2 - f_x^2 - f_y^2}$ is imaginary and this equation describes a circle with radius $\frac{1}{\lambda}$ in a frequency space as shown in Fig. 4.3. For all the frequencies inside the circle the expression is real, and for all the frequencies outside the circle the expression becomes imaginary. When the expression is imaginary, the complex exponential $e^{2\pi i z_0 \sqrt{\left(\frac{1}{\lambda}\right)^2 - f_x^2 - f_y^2}}$ becomes a decaying exponential $e^{-2\pi z_0 \sqrt{\left(\frac{1}{\lambda}\right)^2 - f_x^2 - f_y^2}}$ as the propagation distance z increases. The physical meaning is that all the spatial frequencies within the circle with radius $\frac{1}{\lambda}$ can propagate, whereas the spatial frequencies outside the circle decay exponentially as they propagate, hence the term evanescent field.

The higher spatial frequencies of that field are required to describe the small details in that field, so they correspond to high-resolution information. When this information is lost, the resolution of the field is limited, and this limit is determined by the illumination wavelength λ . If there is an imaging system where the field has to propagate for a distance that is significantly larger than the wavelength of the

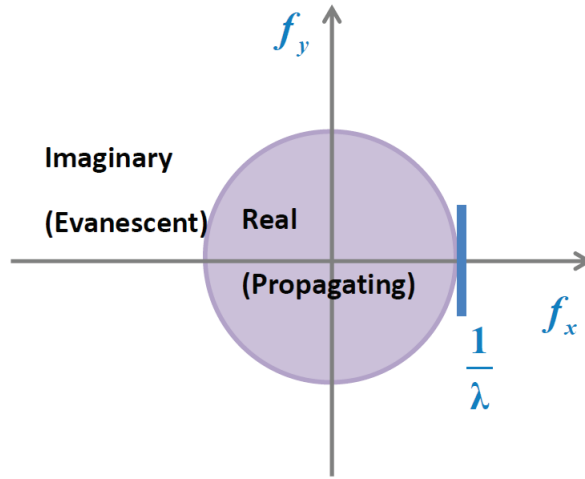


Figure 4.3: Definition of evanescent and propagating waves with different spatial frequencies.

light, the imaging resolution will be limited by the wavelength of the illumination because the evanescent wave decays exponentially as it propagates. This limit is called the diffraction limit.

There are certain methods to achieve a resolution higher than the diffraction

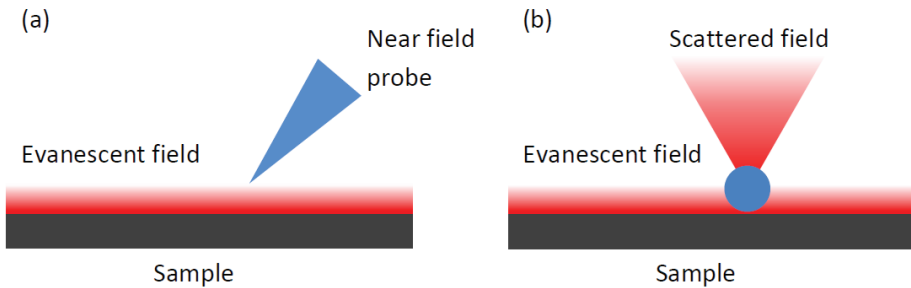


Figure 4.4: Methods for super-resolution with evanescent waves.

limit, which is called super-resolution. One of these methods is near field scanning optical microscopy (NSOM) (see Fig. 4.4(a)), where the field is probed so close to the sample that the evanescent field has not decayed yet. Another method to convert evanescent fields to propagating fields through interaction with some material, so that high resolution information can still be detected far away (see Fig. 4.4(b)).

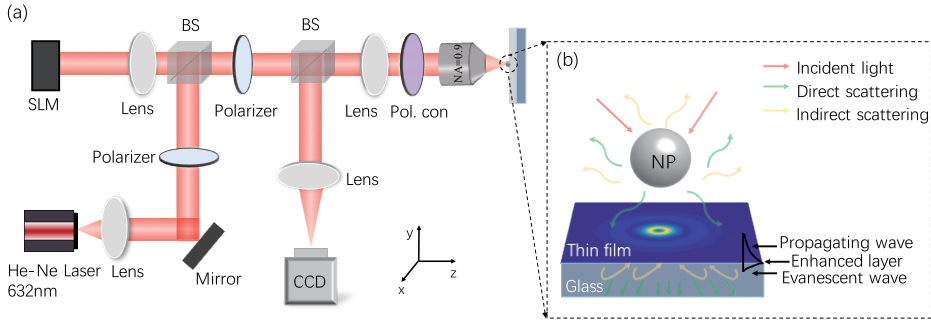


Figure 4.5: Schematic diagram of the imaging system. (a) A complete imaging setup with the illumination of radially polarized beam at the wavelength $\lambda=632nm$. (b) The mechanism of enhancement of evanescent waves by considering a sample on the glass substrate with a thin dielectric film on the top. Abbreviations: beam splitter (BS), spatial light modulator (SLM), polarization converter (Pol.con), nanoparticle (NP).

4.3.2. Single dipole model

Based on the principle of achieving super-resolution in the far field with the evanescent wave as discussed in Fig. 4.4(b), it is important to enhance the evanescent field in the near field. A method is proposed to produce super-resolution patterns based on a dielectric photonic crystal by transmitting high- k evanescent waves diffracted from a grating [19]. Also, there are some fluorescent bio-sensing technologies which utilize the evanescent fields enhanced by dielectric multi-layers [20–22]. Here we design a sample on the top of a thin layer on the substrate which is easier to realize. One example of imaging system is shown in Fig. 4.5(a). The radially polarized light is formed after the red light ($\lambda=632nm$) passes through the polarization converter. Then the light is tightly focused by a high $NA=0.9$ objective lens on a substrate. The information of the sample can be collected in the far field and finally recorded by the CCD. The complex interaction happens between the incident beam, the sample and the thin layer. In order to understand the interactions better, Fig. 4.5(b) gives a detailed illustration of the sample and explains the mechanism of enhancement of evanescent waves [10]. When the incident light (red arrows) illuminates the small particle, evanescent waves can be generated. The direct scattered light (green arrows) includes both propagating and evanescent waves. Some of the scattered light propagates to the far field, while others go into the substrate. The reflected light contains propagating and evanescent waves. In the thin layer, the evanescent wave can be enhanced. After that, the particle can be re-excited by the propagating wave and enhanced evanescent wave. Finally, it will cause a new round of scattering (yellow arrows) to the far field. Compared with the case of no enhanced layer, the evanescent wave decays very quickly in the substrate and cannot interact with the particle. However, by adding a specially designed thin layer, the particle can be re-excited by the increased evanescent waves and new propagating waves can be produced, which provides more information in the far

field.

To understand the principle of the whole imaging process mathematically, let us

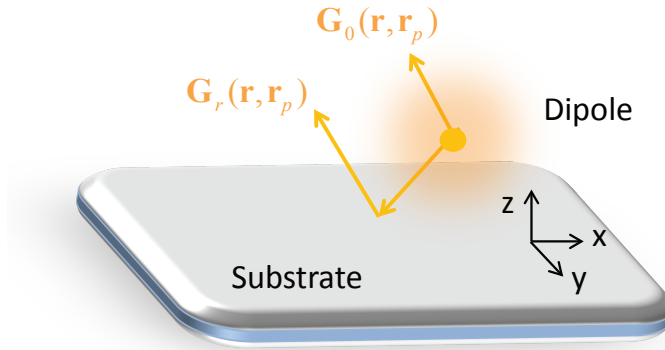


Figure 4.6: Schematic geometry of a dipole placed above the substrate.

consider a Cartesian system (x, y, z) with z as the propagation direction. Since the particle here is sub-wavelength, it can be regarded as an electric dipole and Fig. 4.6 presents the schematic geometry of the problem. As it is known, the dyadic Green's function method [23] is widely used technique in solving problems involving dipole emission near planar surfaces. The field emitted by the dipole in the upper free space ($z > 0$) can be written as the summation from two contributions [24]: [1] the emission of the dipole in free space described by the free space Green's function \mathbf{G}_0 and [2] the reflected field by the surface described by \mathbf{G}_r :

$$\mathbf{U}_{\text{dipole}}(\mathbf{r}) = (\mathbf{G}_0(\mathbf{r}, \mathbf{r}_p) + \mathbf{G}_r(\mathbf{r}, \mathbf{r}_p))\mathbf{p}, \quad (4.16)$$

where $\mathbf{r} = (x, y, z)$ is the position vector of the observation, and $\mathbf{r}_p = (x_p, y_p, z_p)$ is the position vector of the dipole. The free space Green's function \mathbf{G}_0 is

$$\mathbf{G}_0(\mathbf{r}) = -\frac{1}{4\pi} \frac{e^{ik_0|\mathbf{r}-\mathbf{r}_p|}}{|\mathbf{r}-\mathbf{r}_p|} \frac{k_0^2}{\epsilon_0}, \quad (4.17)$$

here ϵ_0 is the permittivity of the free space.

\mathbf{p} represents the dipole moment, and we assume it is known and is expressed as

$$\mathbf{p} = \epsilon_0 \alpha \mathbf{U}_{\text{tot}}^{\text{in}}(\mathbf{r}_p) + \epsilon_0 \alpha \mathbf{G}_r(\mathbf{r}, \mathbf{r}_p)\mathbf{p}, \quad (4.18)$$

It is seen that the reflected field modifies the dipole moment and the effect is called the Purcell effect. If the polarizability α is known, so that

$$\mathbf{p} = \frac{\epsilon_0 \alpha \mathbf{U}_{\text{tot}}^{\text{in}}(\mathbf{r}_p)}{1 - \epsilon_0 \alpha \mathbf{G}_r(\mathbf{r}, \mathbf{r}_p)}, \quad (4.19)$$

where $\mathbf{U}_{\text{tot}}^{\text{in}}$ is related to the total incident field. The reflective field is the inverse Fourier transform of the reflection coefficient times the Fourier transform of the field in homogeneous space and a phase factor due to propagation from z_p to z . The reflective Green's function \mathbf{G}_r is

$$\mathbf{G}_r(\mathbf{r}, \mathbf{r}_p) = \frac{1}{4\pi^2} \iint R(k_{\perp}) \mathcal{F}(\mathbf{G}_0) \left(\frac{k_x}{2\pi}, \frac{k_y}{2\pi}, z_p \right) e^{i[k_x(x-x_p) + k_y(y-y_p) + k_z z]} dk_x dk_y, \quad (4.20)$$

where

$$\mathcal{F}(\mathbf{G}_0(\mathbf{r}, \mathbf{r}_p)) = \frac{e^{-i(k_x x_p + k_y y_p - k_z |z - z_p|)}}{2ik_z}, \quad (4.21)$$

where $\mathbf{k} = (k_x, k_y, k_z)$ is the wave vector, $k_{\perp} = (k_x, k_y)$ is the part of the wave vector perpendicular to the optical axis, with $k_{\perp} = \sqrt{k_x^2 + k_y^2}$ its length, $k_z = \sqrt{k_0^2 n^2 - k_{\perp}^2}$, where $k_0 = 2\pi/\lambda_0$ is the wave number and λ_0 is the wavelength in free space. R and \mathcal{F} denote as the reflection coefficient after multiple transmissions and reflections and the operation of Fourier transform, respectively.

Figure 4.7 shows a sketch of the incident field hitting the thin film on the top of the substrate

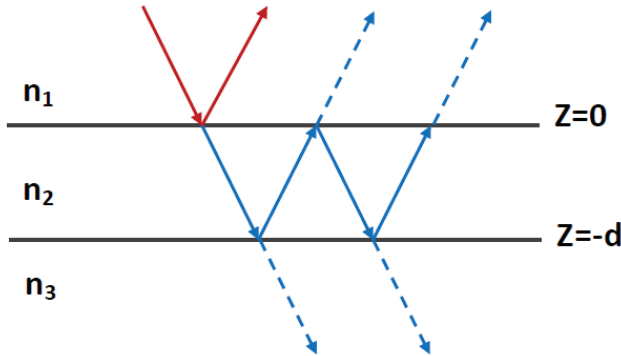


Figure 4.7: A sketch of an incident field hitting the film on top of the substrate. The arrows indicate the direction of the field. The blue arrows inside the film with refractive index n_2 are a reference to a guided mode. The dashed arrows indicate transmissions into the substrate and into the half space above the film. The red arrows are not part of a guided mode.

the substrate, which helps to find the reflection coefficient R in Eq. 4.20. To obtain a guided mode inside the substrate, the wave has to be totally reflected inside the film. This only happens when the angle of incidence is larger than the critical angle of the material, which on itself can only happen when the refractive index of the thin film layer n_2 , is larger than refractive indices of the surrounding materials n_1

and n_3 . Furthermore, the interference of multiple reflected fields has to be constructive, meaning that after being reflected twice (once at $z=0$ and once at $z=-d$) the phase of the field has to be increased by a integer multiple of 2π . As shown in Fig. 4.7, the wave inside the substrate goes up and down multiple times. At every time of reflection, the energy loses since part of the field is transmitted into the substrate or into the half space above the film, indicated by dashed arrows.

The Fresnel reflection coefficient for a wave incident from a medium with refractive index n_i on an interface of a medium with refractive index n_j is:

$$r_{i,j} = \frac{k_{z,i} - k_{z,j}}{k_{z,i} + k_{z,j}}, \quad (4.22)$$

where $k_{z,j}$ is the z component of the wave vector in the material with refractive index n_j . The presence of the thin film gives rise to corrections of the reflection coefficient. These corrections are a transmission at the $n_1 - n_2$ interface, a reflection at the $n_2 - n_3$ interface, and lastly a transmission at the $n_2 - n_1$ interface. These corrections are only valid if, after one round trip, the particular wave exits the substrate with a phase difference of $2m\pi$ (m is an arbitrary integer). The following equation shows how the reflection coefficient is dependent on the extra reflections.

$$R(k_{\perp}) = r_{1,2} + t_{2,1}r_{2,3}t_{1,2}e^{2ik_{z,2}d}\{1 + r_{2,3}r_{2,1}e^{2ik_{z,2}d} + \dots\}, \quad (4.23)$$

where the Fresnel transmission coefficient $t_{i,j} = 1 + r_{i,j} = \frac{2k_{z,i}}{k_{z,i} + k_{z,j}}$. Without considering the high order round trips because of the sharp decrease of the energy, finally the reflection coefficient becomes

$$R(k_{\perp}) = \frac{r_{1,2} + r_{2,3}e^{2ik_{z,2}d}}{1 + r_{2,3}r_{1,2}e^{2ik_{z,2}d}}. \quad (4.24)$$

The previous formula are valid for an arbitrary point \mathbf{r} in the upper half space, However, when observing from the far field, the plane wave expansion for the reflected field is not practical because the integrand is strongly oscillating. It can be seen from the exponent in Eq. 4.20, as it is imaginary for the the propagating plane waves, the integrand in the plane wave expansion of the reflected field oscillates rapidly as function of the integration variable k_{\perp} . However, it is still possible to compute the far field, namely using the method of stationary phase. Appendix C shows the full derivation and here only the final result for the reflected field is given: \mathbf{G}_r is

$$\mathbf{G}_r(\mathbf{r}_{\infty}, \mathbf{r}_p) \approx -R(k_0 n_1 \sin \theta) \frac{1}{4\pi} \frac{e^{ik_0 n_1 |\mathbf{r}_{\infty} - \mathbf{r}_p|}}{|\mathbf{r}_{\infty} - \mathbf{r}_p|}, \quad (4.25)$$

where

$$\sin \theta = \frac{\sqrt{(x - x_p)^2 + (y - y_p)^2}}{|\mathbf{r}_{\infty} - \mathbf{r}_p|}. \quad (4.26)$$

Another way to get the far field imaging information is: as the Green's function can be calculated numerically with stratified media [25], and substituting Eqs. 4.17, 4.19 and 4.20 into Eq. 4.16, the near field $\mathbf{U}_{\text{dipole}}$ radiated by the dipole can be obtained. The far field imaging can be collected by considering the focusing process which has been discussed in the previous chapters. Or performing the matrix operations given in [26, 27] also gives the final imaging information.

4.4. Numerical results and discussions

4.4.1. Reflection coefficient

The most common materials to make photonic crystals are SiO_2 and TiO_2 . Besides, some other materials can also be used in fabrication, for example, inorganic materials including SnO_2 , ZnO , InSb , Si_3N_4 as well as organic materials including polymethyl methacrylate (PMMA), polystyrene (PS), polyethylene (PE), or even some superconductor microstructures or nanostructures. In industrial practice, the chosen materials always have high dielectric constants. For this reason, the materials for the thin film on the substrate we consider in the following simulations are TiO_2 and InSb . To validate the enhancement of the evanescent wave due to the thin layer added on top of the substrate, three kinds of interfaces are taken into account in the calculation: a thick glass ($n_{\text{glass}} = 1.5$) substrate without enhanced layer, 20nm thin layer of TiO_2 ($n_{\text{TiO}_2} = 2.3897$) on top of the thick glass substrate, and 20nm thin layer of InSb ($n_{\text{InSb}} = 4.2842 + 1.8107i$) on top of the thick glass substrate. Figure 4.8 illustrates the enhancement of the reflection coefficient ($r > 1$) when the system is excited by evanescent wave ($k_x/k_0 > 1$). For the s polarized light in Fig. 4.8(a), the enhancement of the case with TiO_2 is much larger than that with InSb slab. The peak amplification happens at $k_x/k_0 = 1.499$, which is 4.606 times higher than the structure without the enhancement film. Similar phenomenon can be seen in Fig. 4.8(b) for the illumination of the p polarized light. In this case, with the thin InSb film, the enhancement starts from $k_x/k_0 > 1$, while with the TiO_2 , the enhancement starts from $k_x/k_0 > 1.281$. Note that, the difference in the reflection coefficient for the two enhancing layers is smaller with the p polarized excitation, compared with the s polarized case. The results in Fig. 4.8 demonstrate that the design of the thin film can amplify the evanescent wave in the near field, this does not occur when only a thick glass substrate is used.

4.4.2. Near field

The dipole approximation makes the physical interaction between the illumination, particles, thin layer and substrate more easily to understand. However, in order to make the calculations more realistic, one should consider real nanospheres as objects. Unlike the analytical method of dipole model, the scattering problem of the sphere should be solved by the numerical method. Therefore, we perform numerical simulations using the 3D finite difference time domain (FDTD) method to obtain the near field in the case of finite size spheres. The images can be rebuilt by taking the simulated near field as $\mathbf{U}_{\text{dipole}}$.

A dielectric nanosphere with a radius $r = 200\text{nm}$ is put on the top of the thin film

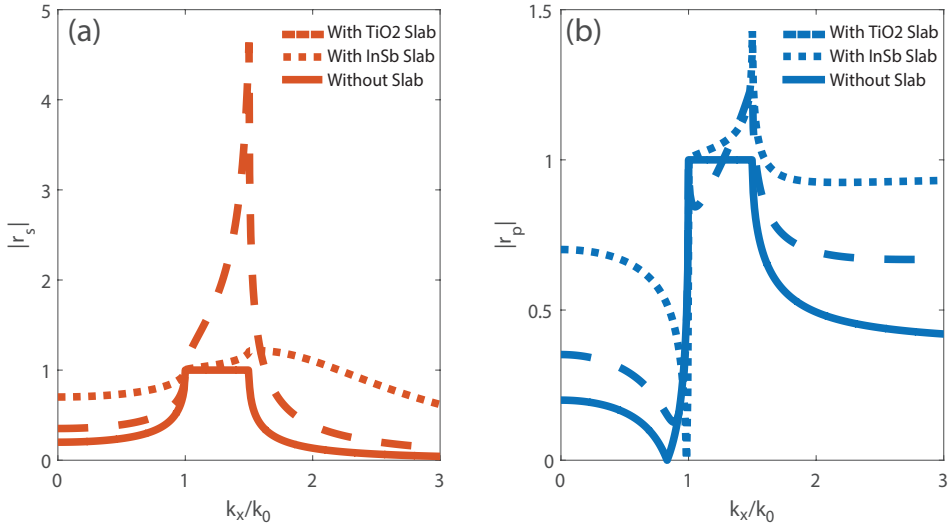


Figure 4.8: The comparison modulus of the reflection coefficients for s- and p- polarizations in the near field of xz plane with the illumination radially polarized beams on the top of the nanosphere (a) $|r_s|$ and (b) $|r_p|$. The solid, dashed and dotted lines corresponds to no slab, InSb slab, and TiO₂ slab, respectively.

layer. The material of the sphere is polystyrene latex (PSL). By using numerical analysis-Lumerical FDTD, the near field distributions in the xz plane under the excitation of focused radially polarized light with the wavelength $\lambda = 632nm$ are shown in Fig. 4.9. Strong scattering field can be seen with the adding slabs TiO₂ and InSb when radially polarized light (Figs. 4.9(a)-(c)) is focused on the top of the sample. Although the near field is enhanced, the scattering light is mainly localized. This is because of the large longitudinal component contained in the tightly focused radially polarized light [28]. A dipole excited by a focused radially polarized beam, will radiate radially polarized waves. If the dipole is on a substrate, there will be the radially polarized reflected fields as well. Looking at the reflection coefficients shown in Fig. 4.8, one observes that the values of $|r_p|$ are largest in the case of the InSb slab, which explains the corresponding strongest near field distribution in Figs. 4.9(c) when the sample is illuminated by the radially polarized light. The enhanced signal can be achieved by inserting the enhancing layer and this gives an explanation of the improved scattering in the far field.

4.4.3. Imaging

Once the near fields $\mathbf{U}_{\text{dipole}}$, which is related to field above the top of the nanosphere in xy plane are obtained, the final imaging can be calculated by the process of re-focusing. Figure 4.10 displays the total scattering field distributions of one dielectric sphere in the xy imaging plane without (Fig. 4.10(a)) and with the enhancing layer (Figs. 4.10(b)-(c)) under the excitation of focused radially polarized beam. As the previous discussion, the total scattering fields are donut shaped. Comparing Figs.

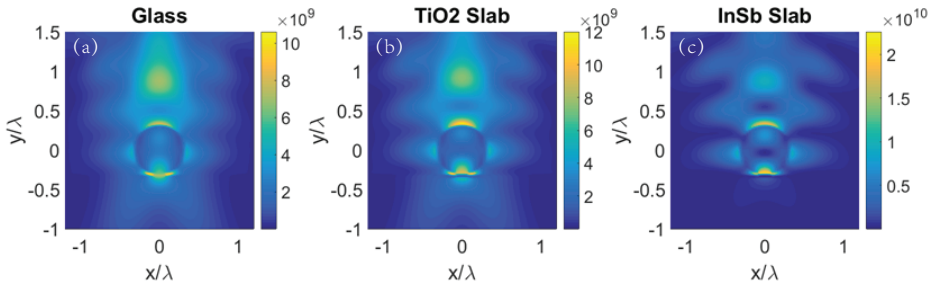


Figure 4.9: The comparison of total intensity distributions in the near field of xz plane with the illumination radially polarized beams on the top of the nanosphere without (a), with TiO₂ (b) and with InSb (c) slab.

4.10(b) and 4.10(c) with Fig. 4.10(a), it can be seen that when thin slabs are inserted, the SNR in the imaging plane are higher than the case of no enhanced layer. This agrees well with the results of near field distributions shown in Fig. 4.9. The corresponding cross section of the normalized total scattering fields is presented in Fig. 4.10(d). Even though the highest SNR is achieved with the InSb as an enhancing layer, the side lobes here are stronger than the case without the enhancing layer and with the layer of TiO₂. The side lobes will decrease the lateral resolution if more spheres are present in the neighborhood. Besides, the sharper distribution in the case of the TiO₂ thin layer, the more accurate particle localization [24]. This will be further demonstrated by the following discussion of imaging two particles.

In order to see whether the lateral resolution in the imaging plane can be improved or not, two identical nanospheres are considered as the new sample. The characteristics of the nanospheres are the same as that in Fig. 4.10. The two nanospheres are placed symmetrically with the y axis and the distance between them changes from 600nm to the smallest resolved value. Based on the performance of the high intensity and better localization in Fig. 4.10, we discuss the imaging of two spheres on the substrate with the enhancing TiO₂ layer is shown in Figs. 4.11(a₁)-4.11(d₁). For comparison, the imaging of two spheres on the substrate without the enhancing layer is shown in Figs. 4.11(a₂)-4.11(d₂). When the two spheres are separated by a large distance 600nm , they can be resolved easily in both conditions. With the decrease of the separated distance, the resolved ability decreases as well. Similar to the Rayleigh criterion, it can be found that two spheres can still be distinguished with a distance of $d = 400\text{nm}$ in the case of with the enhancing TiO₂ layer, while they cannot be resolved anymore at the same distance without the enhancing layer. When the distance is down to 200nm , the two particles are not distinguished anymore for both substrate cases. According to the diffraction limit $d = 0.61\lambda/\text{NA}$, the smallest distance that can be resolved is $d = 0.678\lambda$ in our imaging system theoretically. However, due to the combination of focused radial polarization and the addition of the enhancement layers, the two nanospheres can still be resolved when the distance between them de-

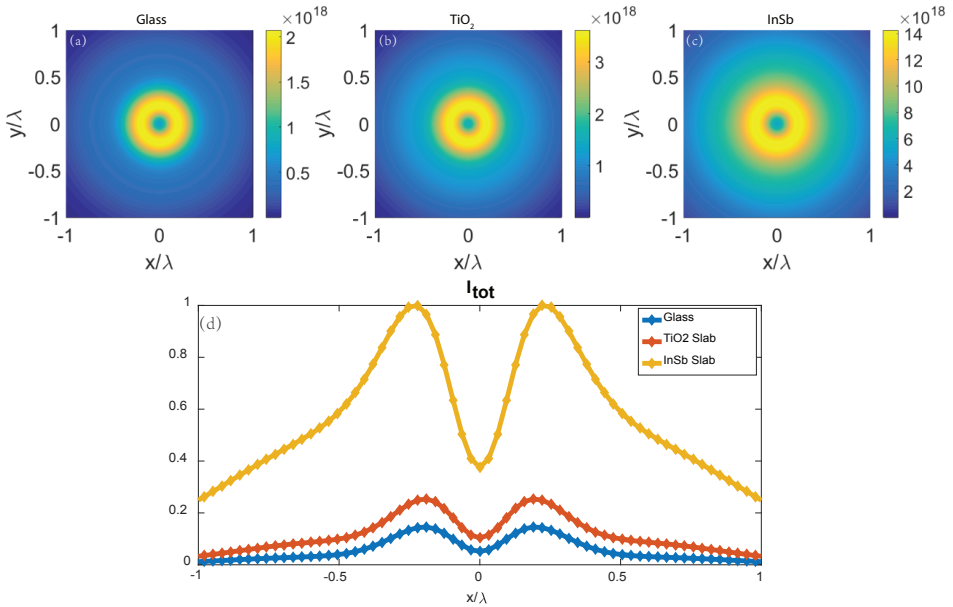


Figure 4.10: Imaging of one sphere in the xy plane without (a) and with ((b)- TiO_2 , (c)-InSb) the enhanced layer under the illumination of radially polarized light. (d) is the cross section of the normalized scattering intensity.

creases to $d = 400\text{nm} = 0.634\lambda$, which is beyond the diffraction limit and means improvement of the lateral resolution. Another important point to judge the imaging performance is the position of two spheres in the imaging plane. The center positions of the spheres in theory are given in red below each subplot and the corresponding positions in the imaging plane with and without the enhancing layer are marked in black dashed lines in each subplot. For example, when $d = 600\text{nm}$, the positions of two spheres are $x = \pm 0.791\lambda$ theoretically, which agrees well with $x_{\text{spheres}} = \pm 0.790\lambda$ in the imaging plane with the TiO_2 layer. However, the error is larger when the two spheres are only on the top of glass as presented in Fig. 4.11(a₂). In the same way, with a separated distance of 500nm (Fig. 4.11(b₁)), the center position is $x = \pm 0.700\lambda$ with the structure with TiO_2 slab, and the error is only 0.012λ . But in the case of a glass substrate, the center positions remain the same with the decrease of separation between the spheres, as shown in Fig. 4.11(b₂). Therefore, the center position of the two identical spheres can also be used as a criterion to determine the localization ability as well as to judge the performance of the imaging system.

4.5. Experimental validation

The above numerical results give an indication that with the TiO_2 on the glass substrate, the imaging resolution will be enhanced. To support the simulated results,

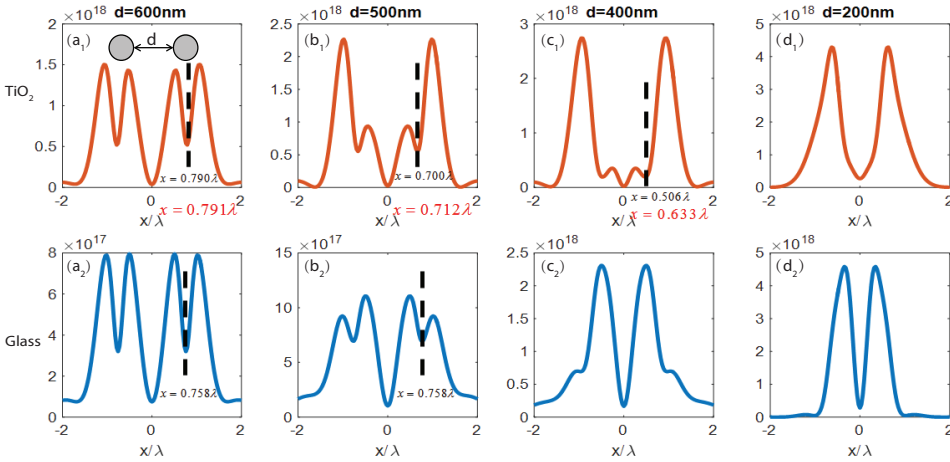


Figure 4.11: Profile of the imaging of two separated nanospheres supported on different substrates with various distances between the spheres: $d = 600nm$, $d = 500nm$, $d = 400nm$ and $d = 200nm$. (a₁)-(d₁): with the enhancing TiO₂ slab on the top of glass, (a₂)-(d₂): without enhancing slab.

a simple experiment is conducted. The sample is a thin fish skin on the glass substrate without (Fig. 4.12(a)) and with (Fig. 4.12(b)) a thin TiO₂ film on the top. The sample is put in a reflection microscope illuminated by white light, and the reflective wide field image is recorded on a CCD camera. It has been discussed in Chapter 3 that the resolution can be quantified by the derivative of the intensity which is given in Eq. 3.3 [29]. The derivatives in both cases (with and without the slab) obtained from the dashed lines at the same position in Fig. 4.12(a) and (b) are presented in Fig. 4.12(c). From the decreasing slope, it can be found that the line corresponding to the case of with the film changes faster than that of no film, which indicates that the resolution is better when a TiO₂ is added on the top of the glass.

4.6. Conclusion

In this chapter, we theoretically investigate how the resolution can be enhanced by inserting a thin dielectric slab on the top of a substrate. By using the principle of evanescent wave amplification, it is demonstrated that higher SNR, better lateral resolution and localization can be achieved when imaging subwavelength particles nearby each other. Through comparison with the case of no enhanced layer, the smallest distance between two nanospheres located on a 20nm thin TiO₂ layer is $d = 400nm = 0.634\lambda$, which is beyond the diffraction limit. The findings have a wide range of applications in the imaging process and can be extended in several ways, such as combining with different microscopy techniques after fabricating suitable enhancing layers for the sample, which is confirmed by a simple experiment.

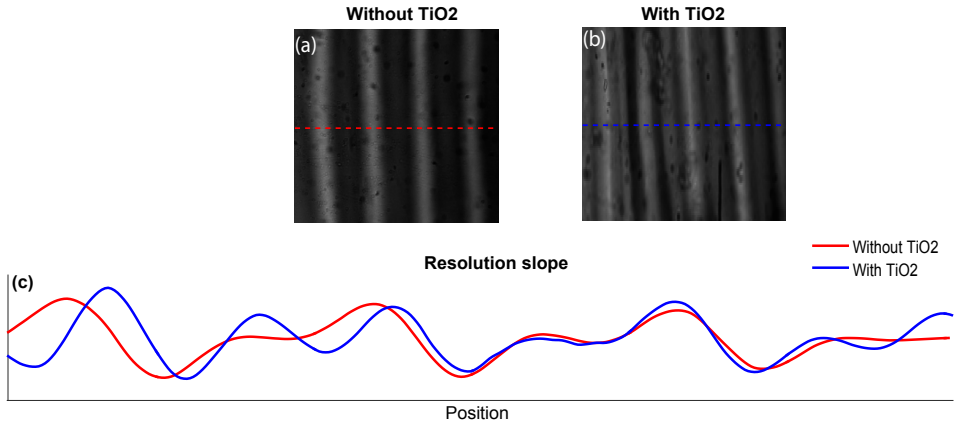


Figure 4.12: Wide field imaging of a fish skin attached on the glass substrates without (a) and with (b) TiO_2 layer on the top. The derivation lines along the dashed line in (a) and (b) are plotted in (c).

References

- [1] P. Meng, S. F. Pereira, X. Dou, and H. P. Urbach, *Superresolution effect due to a thin dielectric slab for imaging with radially polarized light*, *Opt. Express* **28**, 20660 (2020).
- [2] V. Veselago, *Electrodynamics of substances with simultaneously negative ϵ and μ* , *Usp. Fiz. Nauk* **92**, 517 (1967).
- [3] J. B. Pendry, *Negative refraction makes a perfect lens*, *Phys. Rev. Lett.* **85**, 3966 (2000).
- [4] N. Fang, H. Lee, C. Sun, and X. Zhang, *Sub-diffraction-limited optical imaging with a silver superlens*, *Science* **308**, 534 (2005).
- [5] D. O. S. Melville and R. J. Blaikie, *Super-resolution imaging through a planar silver layer*, *Optics Express* **13**, 2127 (2005).
- [6] S. Durant, Z. Liu, J. M. Steele, and X. Zhang, *Theory of the transmission properties of an optical far-field superlens for imaging beyond the diffraction limit*, *J. Opt. Soc. Am. B* **23**, 2383 (2006).
- [7] Z. Liu, H. Lee, Y. Xiong, C. Sun, and X. Zhang, *Far-field optical hyperlens magnifying sub-diffraction-limited objects*, *Science* **315**, 1686 (2007).
- [8] O. E. Gawhary, N. J. Schilder, A. da Costa Assafrao, S. F. Pereira, and H. P. Urbach, *Restoration of s-polarized evanescent waves and subwavelength imaging by a single dielectric slab*, *New Journal of Physics* **14**, 053025 (2012).
- [9] C. J. Regan, D. Dominguez, L. Grave de Peralta, and A. A. Bernussi, *Far-field optical superlenses without metal*, *Journal of Applied Physics* **113**, 183105 (2013).

- [10] S. Roy, S. F. Pereira, H. P. Urbach, X. Wei, and O. El Gawhary, *Exploiting evanescent-wave amplification for subwavelength low-contrast particle detection*, *Phys. Rev. A* **96**, 013814 (2017).
- [11] A. S. van de Nes, L. Billy, S. F. Pereira, and J. J. M. Braat, *Calculation of the vectorial field distribution in a stratified focal region of a high numerical aperture imaging system*, *Optics Express* **12**, 1281 (2004).
- [12] P. Török, P. Varga, and G. R. Booker, *Electromagnetic diffraction of light focused through a planar interface between materials of mismatched refractive indices: structure of the electromagnetic field. i*, *J. Opt. Soc. Am. A* **12**, 2136 (1995).
- [13] L. E. Helseth, *Roles of polarization, phase and amplitude in solid immersion lens systems*, *Optics Communications* **191**, 161 (2001).
- [14] D. P. Biss and T. G. Brown, *Cylindrical vector beam focusing through a dielectric interface*, *Optics Express* **9**, 490 (2001).
- [15] D. P. Biss and T. G. Brown, *Cylindrical vector beam focusing through a dielectric interface: reply to comment*, *Optics Express* **12**, 970 (2004).
- [16] R. H. Jordan and D. G. Hall, *Free-space azimuthal paraxial wave equation: the azimuthal bessel–gauss beam solution*, *Optics Letters* **19**, 427 (1994).
- [17] T. Thio, *A bright future for subwavelength light sources: Generating tiny points of light for such things as storing data on optical disks is aided by a new theory involving evanescent waves*, *American Scientist* **94**, 40 (2006).
- [18] J. W. Goodman, *Introduction to Fourier optics* (2005).
- [19] G. Liang, X. Chen, Z. Wen, G. Chen, and L. J. Guo, *Super-resolution photolithography using dielectric photonic crystal*, *Optics Letters* **44**, 1182 (2019).
- [20] K. Toma, E. Descrovi, M. Toma, M. Ballarini, P. Mandracci, F. Giorgis, A. Mateescu, U. Jonas, W. Knoll, and J. Dostálek, *Bloch surface wave-enhanced fluorescence biosensor*, *Biosensors & bioelectronics* **43**, 108 (2013).
- [21] M. Ballarini, F. Frascella, F. Michelotti, G. Digregorio, P. Rivolo, V. Paeder, V. Musi, F. Giorgis, and E. Descrovi, *Bloch surface waves-controlled emission of organic dyes grafted on a one-dimensional photonic crystal*, *Applied Physics Letters* **99**, 144 (2011).
- [22] M. Ballarini, F. Frascella, E. Enrico, P. Mandracci, N. De Leo, F. Michelotti, F. Giorgis, and E. Descrovi, *Bloch surface waves-controlled fluorescence emission: coupling into nanometer-sized polymeric waveguides*, *Applied Physics Letters* **100**, 39 (2012).
- [23] J. D. Jackson, *Classical electrodynamics* (1999).

- [24] L. Novotny and B. Hecht, *Principles of nano-optics* (2012).
- [25] M. Paulus, P. Gay-Balmaz, and O. J. Martin, *Accurate and efficient computation of the green' s tensor for stratified media*, [Physical Review E](#) **62**, 5797 (2000).
- [26] T. Wilson, R. Juškaitis, and P. Higdon, *The imaging of dielectric point scatterers in conventional and confocal polarisation microscopes*, [Optics Communications](#) **141**, 298 (1997).
- [27] P. Török, P. Higdon, and T. Wilson, *Theory for confocal and conventional microscopes imaging small dielectric scatterers*, [Journal of Modern Optics](#) **45**, 1681 (1998).
- [28] R. Dorn, S. Quabis, and G. Leuchs, *Sharper focus for a radially polarized light beam*, [Phys. Rev. Lett.](#) **91**, 233901 (2003).
- [29] P. Meng, H. Pham, S. F. Pereira, and H. P. Urbach, *Demonstration of lateral resolution enhancement by focusing amplitude modulated radially polarized light in a confocal imaging system*, [Journal of Optics](#) **22**, 045605 (2020).

5

Angular momentum properties of cylindrical vector vortex beams

Optical angular momenta (AM) have attracted tremendous research interest in recent years. We theoretically investigate the electromagnetic field and angular momentum properties of tightly focused arbitrary cylindrical vortex vector (CVV) input beams. Numerical calculations show that an absorptive nanoparticle can be trapped in the intensity hot-spots due to the interaction between the spin and orbital angular momentum of the light beams. The spin-orbit motions of the particle can be predicted and controlled when the influences of different parameters, such as the topological charge, the polarization and the initial phases are taken into account. These findings will be helpful in optical beam shaping, optical spin-orbit interaction and practical optical manipulation.

5.1. Introduction

Since the concept of optical vortices (OVs) was first proposed by Coulet *et al.* in 1989 [2], OVs have been used in a wide scope of applications [3], such as optical tweezers [4–9], nonlinear optics [10–12], optical machining [13–15], microscopy and imaging [16, 17]. Optical beams have been known to carry angular momentum (AM) [18–20], which expresses the amount of dynamical rotation in the electromagnetic field. There are two distinct forms of AM: spin angular momentum (SAM) and orbital angular momentum (OAM) [21–24]. Allen *et al.* proposed the OAM in vortex beams where the OVs propagate in paraxial beams, which unveiled a new understanding of the connection between macroscopic optics and quantum effects [25]. The OAM depends on the fundamental characteristics of electromagnetic fields, and in particular on the wavefront shape, which makes the particle rotate around the optical axis. The SAM is related to the optical polarization and in particular to circular polarization, which causes the rotation of the particle around its own axis [26, 27]. Generally, the two different AM forms are independent, but they can interact and be mutually coupled in specific optical processes such as in inhomogeneous or anisotropic media [28–30] and tightly focusing of circularly polarized beams [31].

In a high NA focusing system, one needs to take the polarization state of the light into account. Cylindrical vector vortex (CVV) optical fields have raised a great deal of interest due to their unique polarization and focusing properties [32–34]. Two extreme cases are radially polarized vortex (RPV) and azimuthally polarized vortex (APV) beams. Previous research work that was mainly on OAM can induce localized SAM in the strong focusing of spin-free linearly, radially, azimuthally, and cylindrically polarized beams [35–39]. However, when a CVV beam is focused, other optical properties including initial phase, topological charge and optical torque should be considered and exploited.

In this chapter, we study the spinning dynamics of particles with highly focused CVV input beams. With the Richards and Wolf formulas for the calculation of focused field of an arbitrary CVV beam, we can theoretically obtain all components of the electromagnetic field near focus in a high NA optical system, as well as SAM densities of the focused field. The focusing behavior and SAM densities of CVV beams with broken axial symmetry are also considered. An absorptive trapped particle is introduced to discuss the influences of optical torque on the motions of the particle. It is demonstrated that even if the illumination beam is asymmetrical, the nanoparticle can still be trapped at the hot-spot of the focused field. The motions of the particle are shown by considering the interaction between the spin and orbital AM. Furthermore, the influence of the size and material of the nanoparticle, the topological charge and the initial phase of the beam, and different sector apertures, are discussed in detail. These results can be used as guidance for the practical optical manipulation, even with asymmetrical illumination beams, which can be used for particle transport in particular.

5.2. Local SAM of focal field for CVV beams

5.2.1. Properties of the symmetrical CVV beams

A generalized CVV beam can be written as a linear superposition of a cylindrically symmetric RPV beam and a cylindrically symmetric APV beam, which are given by [40]

$$\begin{aligned}\mathbf{E}_0 &= A_0 e^{im\varphi} (\cos \varphi_0 \hat{\mathbf{e}}_r + \sin \varphi_0 \hat{\mathbf{e}}_\varphi) \\ &= A_0 e^{im\varphi} [\cos(\varphi + \varphi_0) \hat{\mathbf{e}}_x + \sin(\varphi + \varphi_0) \hat{\mathbf{e}}_y],\end{aligned}\quad (5.1)$$

where A_0 is a constant determining the relative amplitude distributions of the input optical field, φ and φ_0 represent the azimuthal angle and initial phase, respectively. $\hat{\mathbf{e}}_r$ and $\hat{\mathbf{e}}_\varphi$ are the unit vectors along the radial and azimuthal directions in the polar coordinate system. m denotes the topological charge of the CVV beam. An optical vortex beam with the azimuthal vortex phase $\exp(im\varphi)$ can be physically interpreted as light that has OAM of $m\hbar$ per photon. For $m = 0$, the polarization distributions of CVV beams with different initial phases $\varphi_0 = 0, \pi/6, \pi/4, \pi/3, \pi/2$ are shown in Fig. 5.1. In particular, $\varphi_0 = 0$ and $\pi/2$, correspond to two special CVV beams: RPV and APV beams.

For tightly focusing optical systems, vectorial theory is needed to accurately

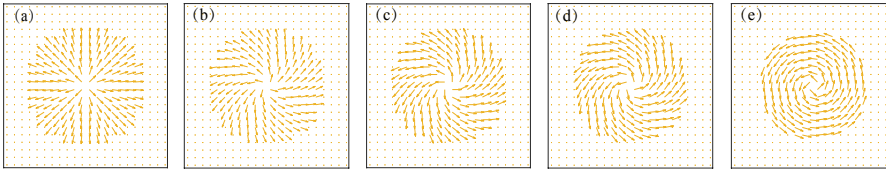


Figure 5.1: Polarization distributions of CVV beams with $\varphi_0 =$ (a) 0, (b) $\pi/6$, (c) $\pi/4$, (d) $\pi/3$, and (e) $\pi/2$, respectively, when the topological charge $m = 0$.

describe the field near the focal plane. When focused in a homogeneous medium with a real-valued refractive index n , with the Richard-Wolf theory, the electric and magnetic fields in the focal region can be expressed as [41]

$$\begin{aligned}\mathbf{E}(r, \phi, z) &= \frac{-ikf}{2\pi} \int_0^{2\pi} \int_0^{\theta_{\max}} \sqrt{\cos \theta} l(\theta) \sin \theta e^{im\varphi} \mathbf{M}_e \exp(i\mathbf{k} \cdot \mathbf{r}) d\theta d\varphi, \\ \mathbf{H}(r, \phi, z) &= \frac{-ikf}{2\pi} \int_0^{2\pi} \int_0^{\theta_{\max}} \sqrt{\cos \theta} l(\theta) \sin \theta e^{im\varphi} \mathbf{k} \times \mathbf{M}_e \exp(i\mathbf{k} \cdot \mathbf{r}) d\theta d\varphi,\end{aligned}\quad (5.2)$$

where the wave numbers are $k = k_0 n$ in the medium and $k_0 = 2\pi/\lambda_0$ in free space, with λ_0 the wavelength in vacuum; f is the focal distance, and the maximum tangential angle $\theta_{\max} = \arcsin(\text{NA}/n)$ is determined by the objective lens; θ and φ represent, respectively, the tangential angle with respect to z axis and the azimuthal angle with respect to x axis. \mathbf{M}_e is the propagating unit electric polarization vector in the image plane. $\mathbf{k} = (-\sin \theta \cos \varphi, -\sin \theta \sin \varphi, \cos \theta)$ is the unit vector of

the wave vector; $\mathbf{r} = (r_s \cos \phi_s, r_s \sin \phi_s, z_s)$ is the position vector of an arbitrary point in the image space, and r_s and ϕ_s denote the polar coordinates in a plane z_s . $l(\theta)$ is the entrance pupil amplitude, which is related to Bessel-Gaussian beam [41], here

$$l(\theta) = \exp \left[-\beta^2 \left(\frac{\sin \theta}{\sin \theta_{\max}} \right)^2 \right] J_1 \left(2\beta \frac{\sin \theta}{\sin \theta_{\max}} \right), \quad (5.3)$$

where β is the ratio of pupil radius to the beam waist and J_1 is the first-order Bessel function of the first kind. In this paper, simulations are performed with the parameters $\text{NA} = 0.9$, $\lambda_0 = 633 \text{ nm}$, and $\beta = 1.0$. The electric polarization vectors \mathbf{M}_e in Eq. 5.2, can be shown to be

$$\mathbf{M}_e = \begin{bmatrix} -\sin \varphi_0 \sin \varphi + \cos \varphi_0 \cos \theta \cos \varphi \\ \sin \varphi_0 \cos \varphi + \cos \varphi_0 \cos \theta \sin \varphi \\ -\cos \varphi_0 \sin \theta \end{bmatrix}, \quad (5.4)$$

thus,

$$\mathbf{k} \times \mathbf{M}_e = \begin{bmatrix} -\cos \varphi_0 \sin \varphi - \sin \varphi_0 \cos \theta \cos \varphi \\ \cos \varphi_0 \cos \varphi - \sin \varphi_0 \cos \theta \sin \varphi \\ -\sin \varphi_0 \sin \theta \end{bmatrix}, \quad (5.5)$$

Integrating along the azimuthal direction in Eq. 5.2, we can obtain the electric fields of an arbitrary CVV beam in the focal region in cylindrical coordinates (r_s, ϕ_s, z_s)

$$\mathbf{E}(r, \phi, z) = \frac{-ikf}{2} \int_0^{\theta_{\max}} l(\theta) \mathbf{P}_m \sqrt{\cos \theta} \sin \theta \exp(ikz_s \sin \theta) d\theta, \quad (5.6)$$

where the polarization vector \mathbf{P}_m is

$$\mathbf{P}_m = i^m e^{im\phi_s} \begin{bmatrix} i[J_{m+1}(\xi) - J_{m-1}(\xi)] \cos \varphi_0 \cos \theta - [J_{m+1}(\xi) + J_{m-1}(\xi)] \sin \varphi_0 \\ [J_{m+1}(\xi) + J_{m-1}(\xi)] \cos \varphi_0 \cos \theta - i[J_{m+1}(\xi) - J_{m-1}(\xi)] \sin \varphi_0 \\ 2J_m(\xi) \cos \varphi_0 \end{bmatrix}. \quad (5.7)$$

Here $\xi = kr_s \sin \theta$ and $J_m(\xi)$ is the m th-order Bessel function of the first kind.

For an arbitrary time-harmonic beam, the time-averaged SAM density can be written as [23, 42]

$$\mathbf{S} = \frac{\text{Im}[\epsilon(\mathbf{E}^* \times \mathbf{E}) + \mu(\mathbf{H}^* \times \mathbf{H})]}{4\omega}, \quad (5.8)$$

where ω is the angular frequency of the light beam. The superscript $*$ denotes the complex conjugate and $\text{Im}[z]$ denotes the imaginary part of z . Compared with the dominant interaction between the electric field and particles in nature, the magnetic field acts weakly on them. Therefore, we only take the SAM originated from the electric field into account. Then the three orthogonal components of \mathbf{S} are in

cylindrical coordinates given by

$$\begin{aligned} S_r &= \frac{\epsilon}{4\omega} \text{Im}(E_\phi^* E_z - E_\phi E_z^*), \\ S_\phi &= \frac{\epsilon}{4\omega} \text{Im}(E_z^* E_r - E_z E_r^*), \\ S_z &= \frac{\epsilon}{4\omega} \text{Im}(E_r^* E_\phi - E_r E_\phi^*). \end{aligned} \quad (5.9)$$

Now we first investigate the focusing properties of the CVV beams in free space. The intensity distributions of the electric fields in the focal plane of CVV beams with $\varphi_0 = 0, \pi/4, \pi/3, \pi/2$ and $-\pi/4$, when the topological charge $m = 0$ are shown in Fig. 5.2. For the illumination without OAM ($m = 0$), it is well known that the radial component is a donut shape and the azimuthal component is zero while the longitudinal component is strongly centered when $\varphi_0 = 0$, which corresponds to an RPV beam in Figs. 5.2(a₁)-5.2(d₁). When increasing of φ_0 , the intensities of both radial and longitudinal components decrease while the intensities of the azimuthal components increase. In the extreme case $\varphi_0 = \pi/2$ only azimuthal component exists, which corresponds to the APV beam shown in Figs. 5.2(a₄)-5.2(d₄). It can be seen in Figs. 5.2(a₂)-5.2(d₂) and Figs. 5.2(a₅)-5.2(d₅) that the intensities do not change, when the initial phase φ_0 changes from $\pi/4$ to $-\pi/4$. Figure 5.3 shows the normalized SAM density distributions of the corresponding focused CVV input beams in Fig. 5.2. All the SAM density profiles are donut-shaped and the longitudinal SAM densities S_z remain zero, because such focal field has a purely transverse SAM locally [43]. From Eq. 5.9, when there is no OAM ($m = 0$), it can be easily found that the radial and longitudinal SAM densities equal zero with the RPV illumination shown in Fig. 5.3(a₁)-5.3(c₁) because of the lack of an azimuthal component. Similarly and also interestingly, with the APV illumination, there are no SAM densities at all as in Figs. 5.3(a₄)-5.3(c₄). Apart from these two extreme conditions, for other initial phases, the focal fields all carry transverse SAM densities S_r and S_ϕ . Moreover, the signs between the radial and azimuthal SAM densities are opposite whenever the initial phase φ_0 is positive. It is worth noting that when $\varphi_0 = -\pi/4$, as seen in Figs. 5.3(a₅) and 5.3(b₅), the sign of S_r changes to positive while S_ϕ keeps the same sign compared with Figs. 5.3(a₂) and 5.3(b₂).

Next, we discuss the influence of the topological charge m on the local spin state. For comparison, we start again from the focal field profiles of CVV beams with $m = 1$ and $\varphi_0 = 0, \pi/4, \pi/3, \pi/2$ and $-\pi/4$ in Fig. 5.4. As opposed to focusing CVV beams without OAM in Fig. 5.2, the CVV beams with $m = 1$ generate solid focal spots. The donut-shaped longitudinal intensities disappear gradually with the increase of the initial phase φ_0 , while the focal spots get increasingly sharper as seen in Figs. 5.4(d₁)-5.4(d₄). The special cases of field distributions generated by RPV and APV beams are shown in Figs. 5.4(a₁)-5.4(d₁) and Figs. 5.4(a₄)-5.4(d₄), respectively. It is well known and widely used that the RP beam provides tight focus, but the focal spot of APV beam with $m = 1$ shown in Fig. 5.4(d₄) gives the smallest size compared with focal spots given by RPV beams as shown in Fig. 5.2(d₁). This fact was noted in earlier work [44] and can be used for improving the resolution of optical imaging systems. Figure 5.5 gives the results of SAM density

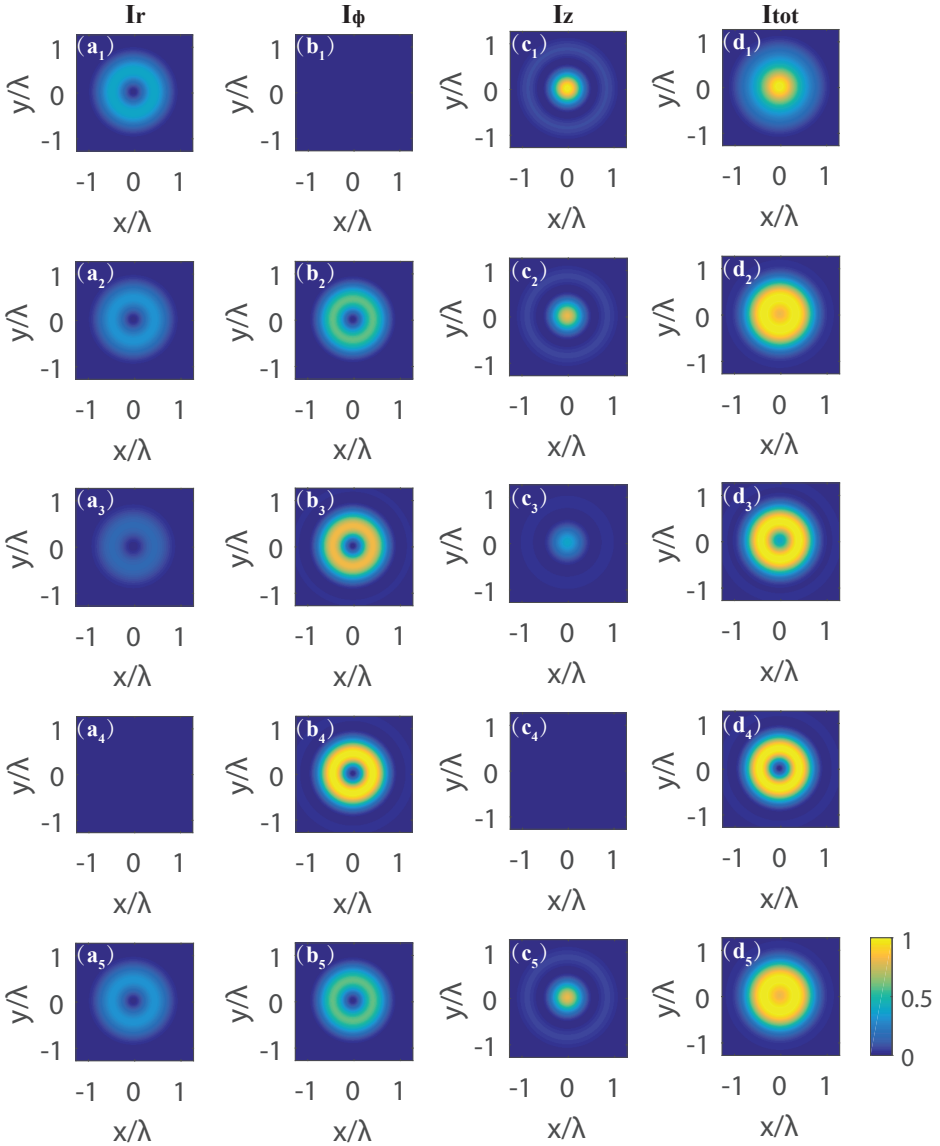


Figure 5.2: Electric field intensity distributions in the focal plane of CVV beams with $\varphi_0 = 0, \pi/4, \pi/3, \pi/2$ and $-\pi/4$ (rows 1-5, respectively), when the topological charge $m = 0$. All the intensities are normalized to the maximum intensities near focus for each illumination mode.

distributions of the corresponding focused CVV input beams with $m = 1$ as in Fig. 5.4. In Fig. 5.5 one observes similar as in Fig. 5.3, but in addition one can notice that the purely transverse spin states in Fig. 5.3 change to three components here. Strong longitudinal SAM densities appear in the focal plane and dominate in three

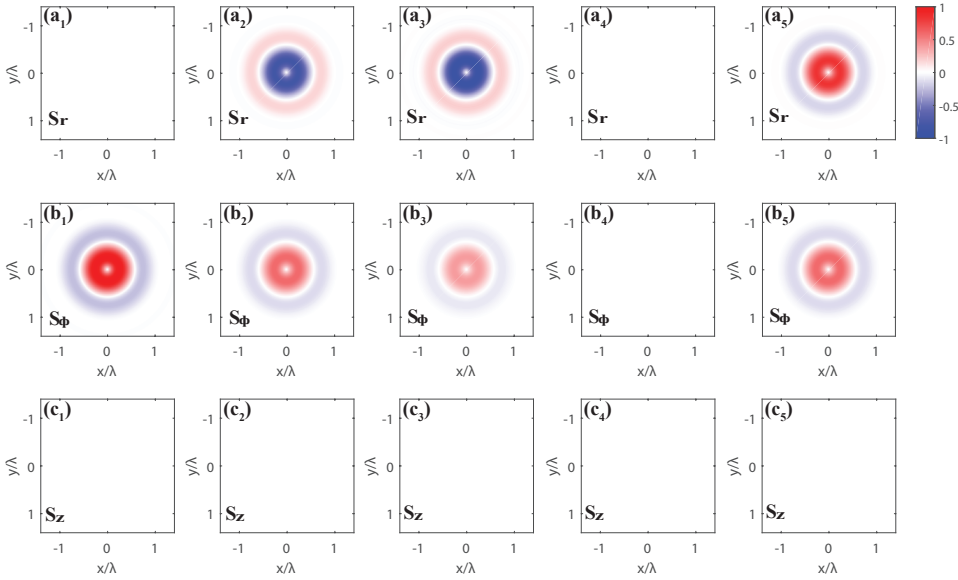


Figure 5.3: Normalized SAM density distributions in the focal plane for CVV beams in Fig. 5.2 with $\varphi_0 = 0, \pi/4, \pi/3, \pi/2$ and $-\pi/4$ from left column to right, respectively. Rows 1-3 are radial, azimuthal and longitudinal components of SAM density.

components, even in the special cases of RPV and APV input beams. The SAM densities of the other two components are getting weaker, which means the properties of the local spin state have been converted. Obviously, the varying ratios between transverse and longitudinal SAM densities is because of different initial phases and the induced OAM. To avoid the misunderstanding, we should point out that the global axial SAM S_z is zero, which can be validated by numerically integrating the S_z density over the whole focal plane.

To explore further the influences of the initial phases and OAM on the distributions of SAM density, Fig. 5.6 depicts the normalized cross sections of SAM densities in the focal plane of strongly focused input CVV beams with $\varphi_0 = 0, \pi/6, \pi/4, \pi/3, \pi/2$ and $-\pi/4$ and topological charge $m = 0$ (Figs. 5.6(a₁)-5.6(c₁)), $m = 1$ (Figs. 5.6(a₂)-5.6(c₂)) and $m = -1$ (Figs. 5.6(a₃)-5.6(c₃)). All distributions have been normalized to their maximum values. In Figs. 5.6(c₂) and 5.6(c₃), it is demonstrated that the longitudinal SAM densities S_z only exist when there is OAM, i.e., $m \neq 0$. We can see that the sign of S_z changes from positive to negative when the topological charge changes from $m = 1$ to $m = -1$, while the absolute values of the amplitudes remain unchanged. With the increase of initial phase φ_0 , the absolute values of S_z increase as well. Conversely, the absolute values of S_ϕ decrease to zero when φ_0 reaches to $\pi/2$ no matter what the topological charge is, seen in Figs. 5.6(b₁)-5.6(b₃). Figures 5.6(a₁)-5.6(a₃) display that the radial SAM density values are zero when $\varphi_0 = 0$ or $\pi/2$ for any value of m . Moreover, the S_r curves overlap when $\varphi_0 = \pi/3$ and $\pi/6$. From the first column (Figs. 5.6(a₁)-5.6(a₃)), one can

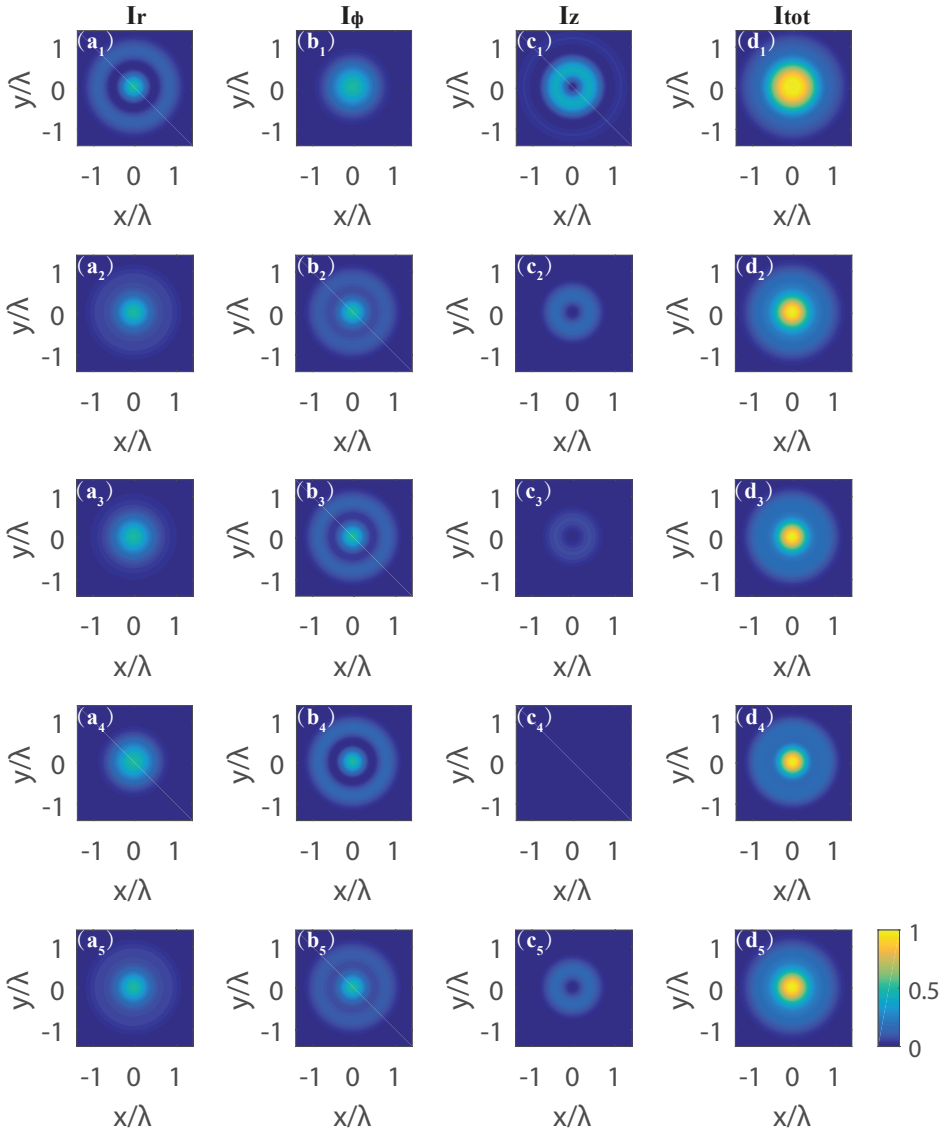


Figure 5.4: Electric field intensity distribution in the focal plane of CVV beams with $\varphi_0 = 0, \pi/4, \pi/3, \pi/2$ and $-\pi/4$ (rows 1-5, respectively), when the topological charge $m = 1$. All the intensities are normalized to the maximum intensities near focus for each illumination mode.

see that the sign of the initial phase φ_0 only affects the radial spin density. When changing the $\varphi_0 = \pi/4$ to $-\pi/4$, the value of S_r changes from negative to positive. The other two components do not change. As aforementioned discussion in Fig. 5.3(a₁) and Fig. 5.5(a₁), with RPV illumination ($\varphi_0 = 0$), the radial SAM density is

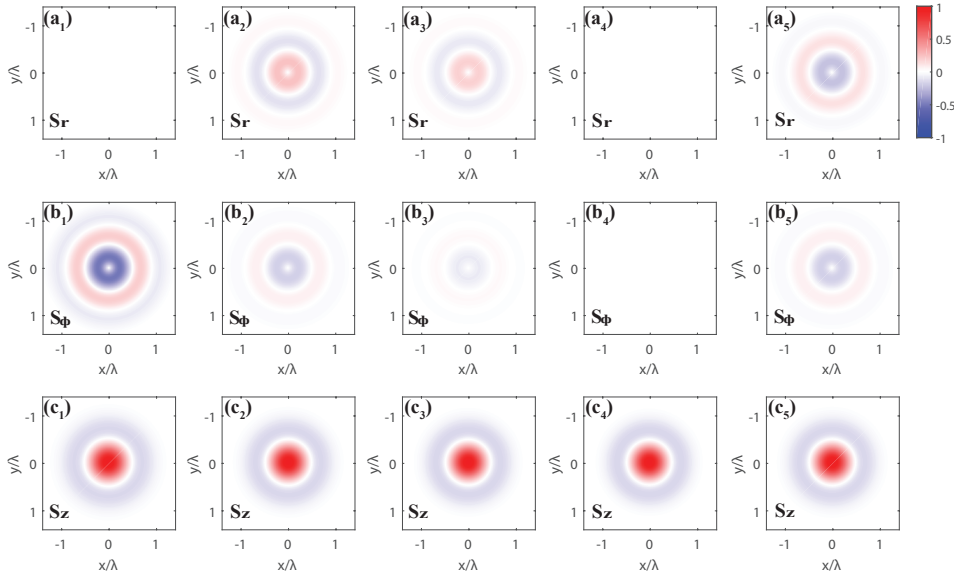


Figure 5.5: Normalized SAM density distributions in the focal plane for CVV beams in Fig. 2.4 with $\varphi_0 = 0, \pi/4, \pi/3, \pi/2$ and $-\pi/4$ from left column to right, respectively. Rows 1-3 are radial, azimuthal and longitudinal components of SAM density.

always zero regardless of the value of m , which agrees well with the results shown in Figs. 5.6(a₁)-5.6(a₃). With APV illumination ($\varphi_0 = \pi/2$), one can only produce longitudinal spin density.

Next, we turn to the impacts of the topological charge on the SAM density. Based on the analysis in Fig. 5.6, the case of $\varphi_0 = \pi/4$ is chosen as a general example. As presented in Fig. 5.7, S_r and S_ϕ are donut-shaped for all values of topological charge that have been tested. However, for the longitudinal SAM densities S_z , they are donut shapes, only for $m > 2$. In all three components, the density distributions expand from the center to two outer sides and the peak intensity value decreases as the value of m increases. For high m , the peak intensity values are of the same order of magnitude. In fact, the redistributions of SAM densities are caused by the spin flux, which originates from the changes of OAM. As the OAM increases, the dark channel expands from the center of the SAM densities [36]. All of these observations validate the interaction between SAM and OAM in the tightly focusing process. The above results will be helpful in the application of optical trapping and tweezers.

5.2.2. Properties of the asymmetrical CVV beams

Most previous efforts on the topics of AM have been devoted to beams with axial symmetry. However, breaking of the symmetry is also a significant and interesting issue because this condition widely exists and has technological applications [45, 46], although this issue has rarely been discussed in the literature so far. A

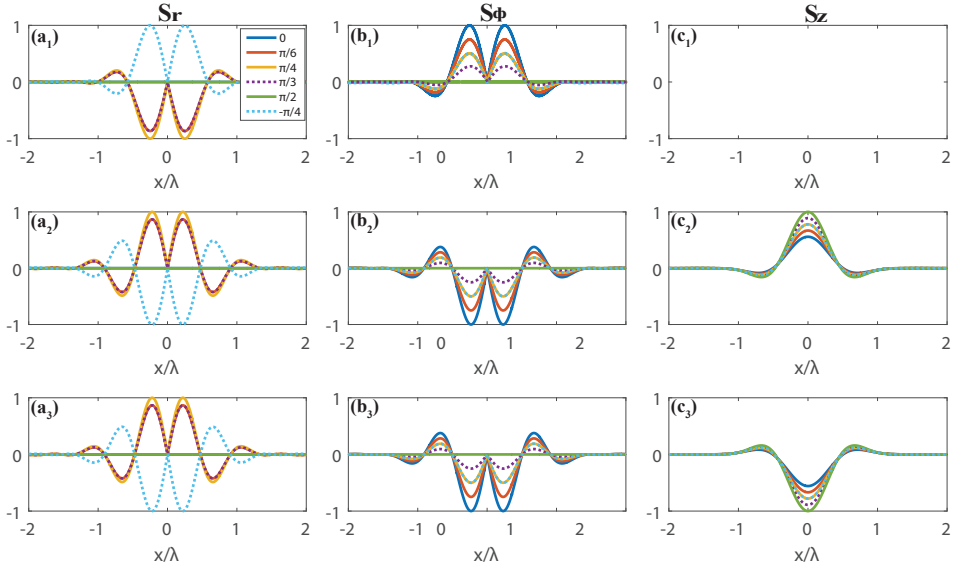


Figure 5.6: Normalized cross-sectional electric spin densities in the focal plane of strongly focused input CVV beams with $\varphi_0 = 0, \pi/6, \pi/4, \pi/3, \pi/2$ and $-\pi/4$ and topological charge $m = 0$ (Figs. 5.6(a₁)-5.6(c₁)), $m = 1$ (Figs. 5.6(a₂)-5.6(c₂)) and $m = -1$ (Figs. 5.6(a₃)-5.6(c₃)), respectively. The distributions in all plots are normalized to their maximum values.

partial vortex output distribution is rotated by $\pi/2$ compared with the input beam when the angular phase pattern occupying half of the input plane is blocked [47]. Franke-Arnold *et al.* [48] investigated the asymmetrical beam produced by using a sector aperture. It was found that the focused axial-symmetry-broken linearly polarized light can be separated into a pair of partial rings which belong to the right-handed (RH) and left-handed (LH) circularly polarized field components carrying the opposite OAM and SAM [49]. It was experimentally confirmed that the focal field of a RPV beam with broken axial symmetry can be used to transport particles in an optical tweezer system [50]. The asymmetrical spinning and orbiting motions of trapped Rayleigh particles can be realized by the use of a tightly focused power-exponent azimuthal variant vector field [51].

Mathematically, a CVV beam with broken axial symmetry that is blocked by a sector aperture and propagates in the z direction can be expressed in cylindrical coordinates (r, φ, z) with the directional unit vectors $(\hat{\mathbf{e}}_r, \hat{\mathbf{e}}_\varphi, \hat{\mathbf{e}}_z)$ as in [52]

$$\mathbf{E}_0 = A_0 \cdot \mathbf{M}(\varphi) \cdot e^{im\varphi} [\cos(\varphi + \varphi_0) \hat{\mathbf{e}}_r + \sin(\varphi + \varphi_0) \hat{\mathbf{e}}_\varphi], \quad (5.10)$$

where A_0 is the relative amplitude of the input field, φ and φ_0 are the azimuthal angle and initial phase, respectively. m represents the topological charge of the CVV phase and $\mathbf{M}(\varphi)$ is the sector aperture, which can be described by the following

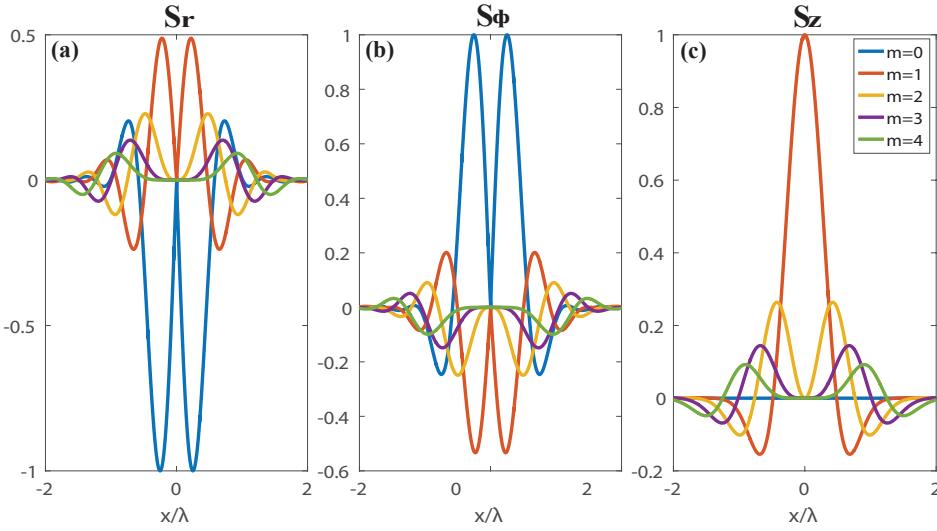


Figure 5.7: Normalized cross-sectional electric spin densities (a) radial SAM density S_r , (b) azimuthal SAM density S_ϕ and (c) longitudinal SAM density S_z in the focal plane of strongly focused input CVV beams with $\varphi_0 = \pi/4$ and topological charge changes from 0 to 4. The distributions in all plots are normalized to their maximum values.

function:

$$M(\varphi) = \begin{cases} 1 & \varphi \in [0, b) \\ 0 & \text{otherwise.} \end{cases} \quad (5.11)$$

The field in the focal plane can be obtained with the same method as described in Chapter 5.2.1. The schematic diagram of the input CVV beam can be seen in Fig. 5.8. Except for Fig. 5.8(a), all subfigures are CVV beams with broken axial symmetry realized by different sector apertures and determined by the value of b .

Figure 5.9 shows the focal field intensity distributions with the illumination of

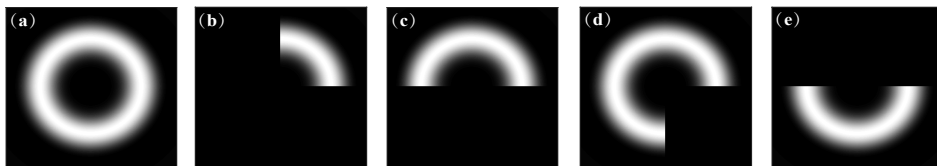


Figure 5.8: Schematic diagram of the input CVV beam with axial symmetry (a) $b = 2\pi$, and broken axial symmetry (b) $b = \pi/2$, (c) $b = \pi$, (d) $b = 3\pi/2$ and (e) $b = -\pi$.

CVV beams in free space. The initial phase is chosen to be $\varphi_0 = \pi/4$ and the topological charge is $m = 4$, which means there is non-zero OAM. For comparison, the first row (Figs. 5.9(a₁)-5.9(d₁)) displays the tightly focused spots of the

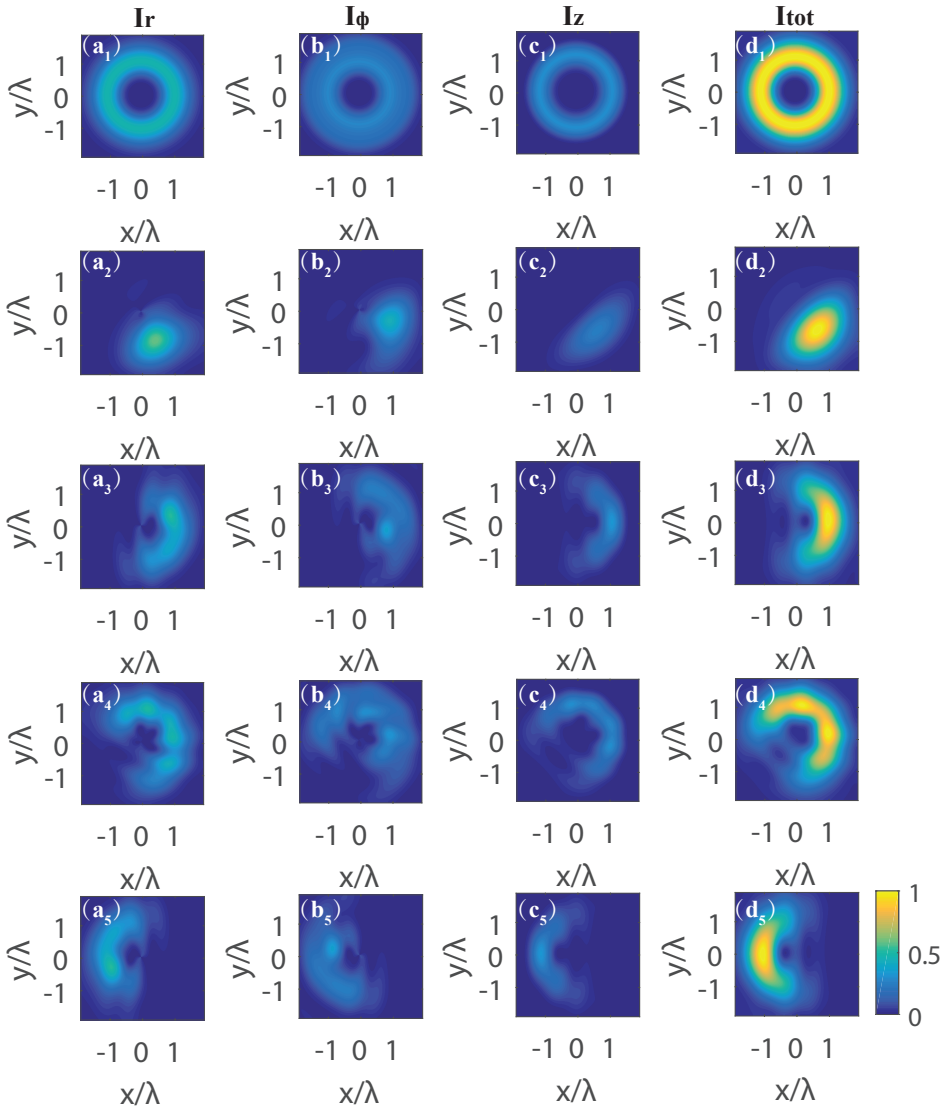


Figure 5.9: Electric field intensity distributions in the focal plane of CVV beams with initial phase $\varphi_0 = \pi/4$ and topological charge $m = 4$. The first row shows the axially symmetric case for $b = 2\pi$; the second, third, fourth and fifth rows show the symmetry breaking case for $b = \pi/2, \pi, 3\pi/2$ and $-\pi$, respectively. The columns from the left to right show the focal behavior of radial, azimuthal, longitudinal components and total intensity distribution, respectively. All the intensities are normalized to the maximum value of the total intensities for each illumination mode.

symmetric input CVV beam ($b = 2\pi$). The four columns from left to right are: radial, azimuthal, longitudinal components and total intensity distribution. Unlike

the conventional radially or azimuthally polarized light, all these components are donut shaped and the longitudinal component is dominant because of the high NA of the system. When the input CVV beam is partially blocked by different sector apertures with $b = \pi/2, \pi, 3\pi/2$ and $-\pi$ as shown in Figs. 5.8(b)-5.8(e), the axial symmetry of the beam is broken and the corresponding intensity distributions in the focal plane can be found from the second to fifth row in Fig. 5.9. While the generated CVV beam with a sector aperture for $b = \pi/2$ occupies the first quadrant as shown in Fig. 5.8(b), the focused intensity distributions of all the components are quarter rings that occupy the fourth quadrant (Figs. 5.9(a₂)-5.9(d₂)). In the same manner, for the input CVV beams with $b = \pi$ and $b = 3\pi/2$, it is worth to notice that all the components at focus are rotated clockwise by an angle of $\pi/2$ with respect to the input fields (Figs. 5.9(a₃)-5.9(d₃)) and Figs. 5.9(a₄)-5.9(d₄)), which agrees well with the finding for the focal behavior of a scalar vortex beam with broken axial symmetry [47]. When $b = -\pi$, the focused field distributions in Figs. 5.9(a₅)-5.9(d₅) are rotated counterclockwise by an angle of π on the basis of the condition in Figs. 5.9(a₃)-5.9(d₃) as $b = \pi$.

The intensity distributions in the focal plane with illuminations of the asymmetrical CVV beams with initial phases $\varphi_0 = 0, \pi/4, \pi/3, \pi/2$ and $-\pi/4$ are presented in Fig. 5.10, where the topological charge $m = 4$ and the sector aperture $b = 3\pi/2$. The initial phase $\varphi_0 = 0$ is related to an asymmetrical RPV beam, the focal intensity distributions are shown in Figs. 5.10(a₁)-5.10(d₁). The radial component is very weak and the longitudinal component dominates the total intensity. When increasing φ_0 from 0 to $\pi/2$, the intensities of the radial component in the first column increase gradually while the azimuthal and longitudinal components in the second and third columns decrease. In particular, the longitudinal component is zero when $\varphi_0 = \pi/2$ in Fig. 5.10(c₄), which is related to an APV input beam. Conversely, the radial component reaches its maximum and dominates in the total intensity. When observing how the total intensity distributions change with increasing initial phase from 0 to $\pi/2$, we find that the size of the hot-spots becomes sharper. Figures 5.10(a₅)-5.10(d₅) illustrate that the sign of the initial phase φ_0 does not change the focal intensity distributions, compared with Figs. 5.10(a₂)-5.10(d₂).

The normalized local SAM density distributions for the focused field of CVV beams in Fig. 5.9 are summarized in Fig. 5.11. The rows are related to the three field components while the columns are related to different sector apertures $b = 2\pi, \pi/2, \pi, 3\pi/2$ and $-\pi$ from left to right, respectively. Note that for the symmetrical input CVV beam, the SAM density is also donut shaped. For the asymmetrical input CVV beams, the SAM densities are not symmetrical, but the shapes and positions of the local SAM density distributions are similar to the focal spots. One common point for all kinds of input CVV beams is that the signs of the radial and azimuthal components are always opposite and the longitudinal components S_z are much stronger than the transverse SAM densities S_r and S_ϕ . The sign of b which changes from π to $-\pi$ only causes the SAM density distributions to be rotated counterclockwise by an angle of π (see Figs. 5.11(a₃)-5.11(c₃) and Figs. 5.11(a₅)-5.11(c₅)). Similarly, considering the influence of the initial phase φ_0 , Fig. 5.12 gives the results of SAM density distributions corresponding to the focused field

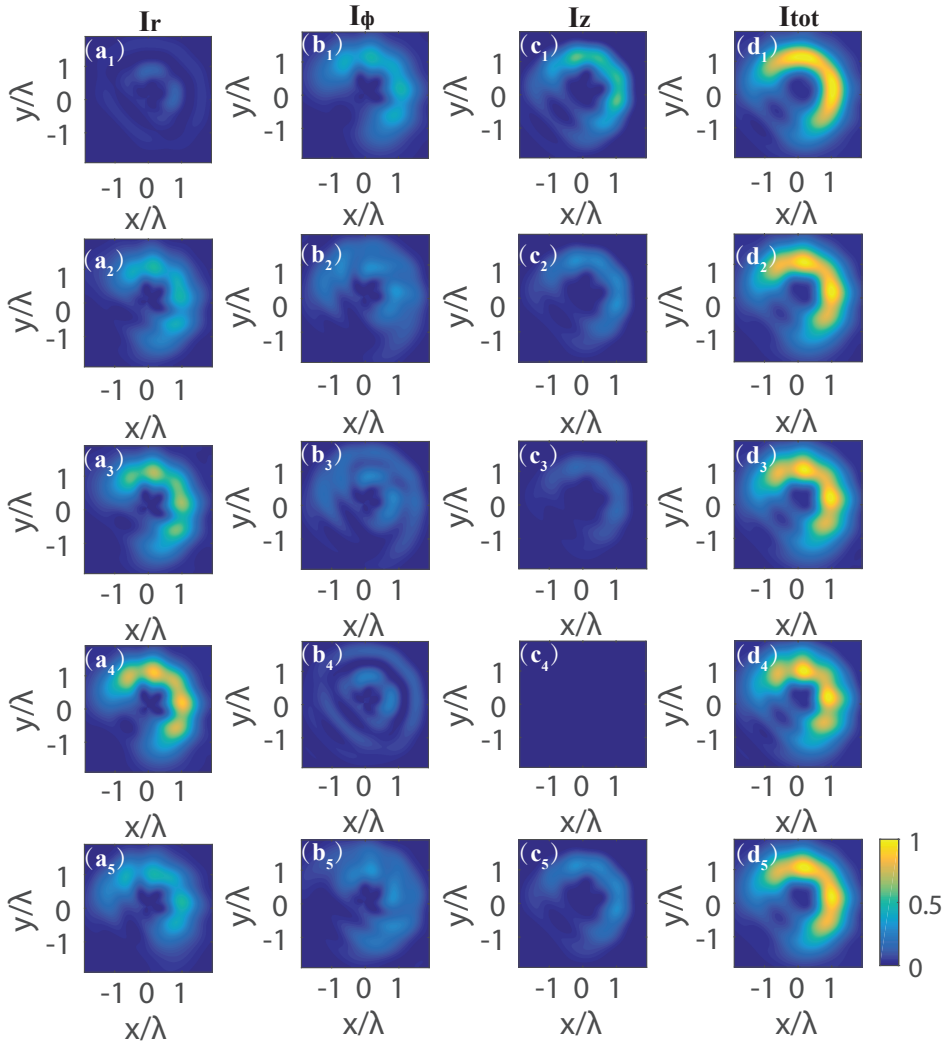


Figure 5.10: Electric field intensity distributions in the focal plane of CWV beams with broken axial symmetry $b = 3\pi/2$ and topological charge $m = 4$. Different initial phases φ_0 are considered from the first row to the last row: 0 , $\pi/4$, $\pi/3$, $\pi/2$ and $-\pi/4$. The columns from the left to right show the focal behavior of radial, azimuthal, longitudinal and total components, respectively. All the intensities are normalized to the maximum value of the total intensities for each illumination mode.

with broken axial symmetry as shown in Fig. 5.10. As in the preceding discussion, the first and fourth columns correspond to the RPV and APV input beams. In Figs. 5.12(a₄)-5.12(c₄), only the longitudinal component of the SAM S_z exists due to the lack of a longitudinal component of the electric field E_z (Fig. 5.10(c₄)). This is the same as the case of a symmetric APV input beam. For the RPV beam, the radial SAM density S_r is smaller than the other two components (Figs. 5.12(a₁)-5.12(c₁)).

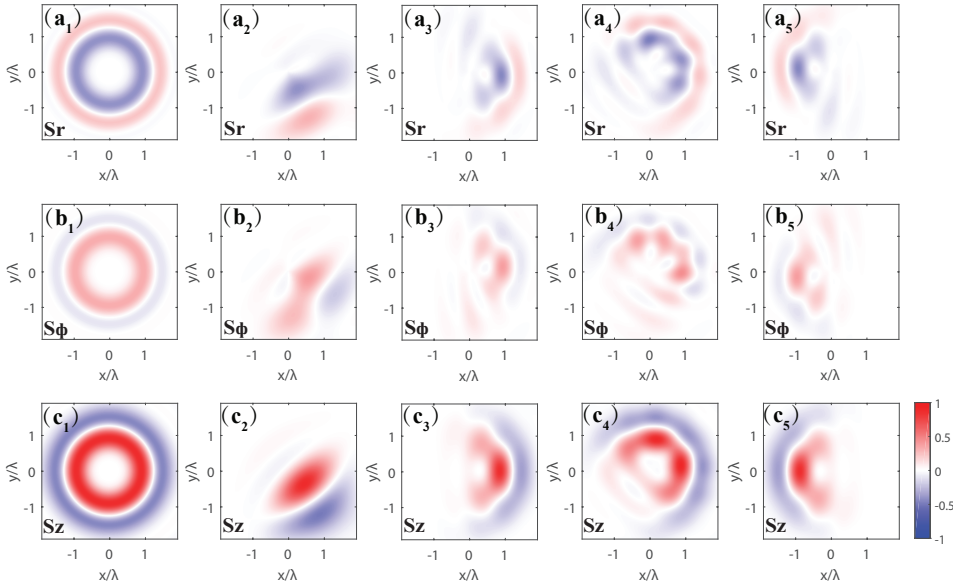


Figure 5.11: Normalized SAM density distributions in the focal plane for the symmetrical and asymmetrical CVV beams in Fig. 5.9 with different sector apertures $b = 2\pi, \pi/2, \pi, 3\pi/2$ and $-\pi$ from left column to right, respectively. The first, second and third rows are the radial, azimuthal and longitudinal components of the SAM density.

As the initial angle φ_0 increases from 0 (first column) to 2π (fourth column), the strength of the transverse components of the SAM density decay gradually to zero, but this does not affect the longitudinal component too much. Special attention is paid to the influence of the sign of the initial phase in Figs. 5.12(a₂) and 5.12(a₅), the signs of the radial SAM density distributions with the initial phase $\varphi_0 = \pi/4$ and $-\pi/4$ are opposite.

The topological charge m , i.e the OAM, is another factor which influences the SAM density distribution. Figure 5.13 shows the SAM density distribution at focus for the asymmetric CVV beam with a sector aperture $b = 3\pi/2$ and initial phase $\varphi_0 = \pi/4$. The area of the SAM density distribution expands by increasing the topological charge from 1 to 8 as seen in the left four columns. Besides this, the sign of the topological charge m makes a big difference in the distribution of the SAM density, which is shown in Figs. 5.13(a₃)-5.13(c₃) and 5.13(a₅)-5.13(c₅). All three components are rotated clockwise by an angle of π as m changes from 4 to -4, and the magnitudes of the transverse SAM densities S_r and S_ϕ are not affected. However, the sign of the longitudinal SAM density S_z is flipped. The above discussion reveals the interaction between the OAM and SAM. Since the motion of small particle can be influenced by the AM, understanding the spin-orbit (SAM-OAM) interaction is important for optical trapping and manipulation.

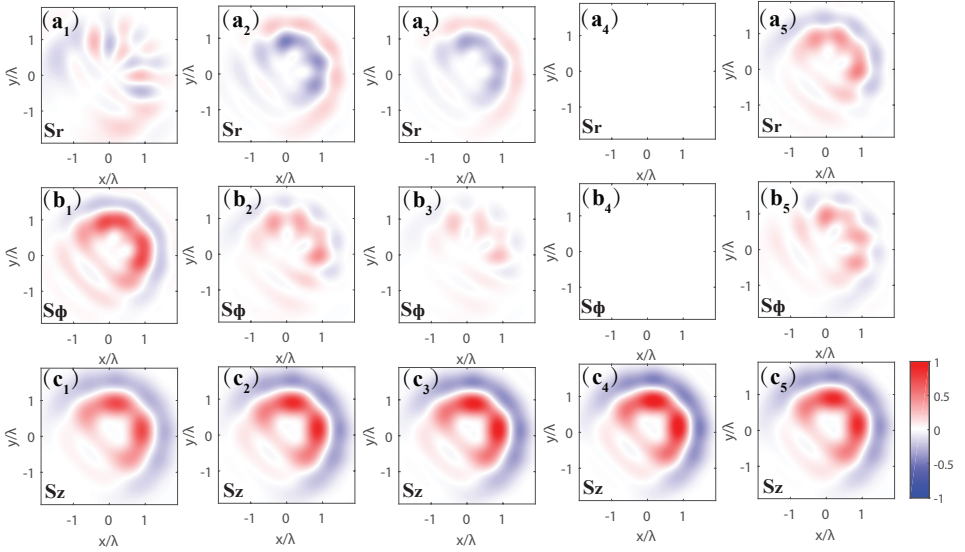


Figure 5.12: Normalized SAM density distributions in the focal plane for the asymmetrical CVV beams in Fig. 5.10 with initial phases $\varphi_0 = 0, \pi/4, \pi/3, \pi/2$ and $-\pi/4$ from left column to right, respectively. The first, second and third rows are the radial, azimuthal and longitudinal components of the SAM density.

5.3. Optical force and torque on nanoparticles

5.3.1. Expressions for optical force and torque

As discussed above, small particles can be trapped due to the localized optical SAM. In other words, the local SAM can also be detected by a small particle. Therefore, we now consider the motion of a Rayleigh sphere with permittivity ϵ_2 in the CVV focal field with a medium of permittivity ϵ_1 . The small sphere with a radius a , which should be smaller than the trapping wavelength can be regarded as an electric dipole. The dipole moment is $\mathbf{p} = \alpha \mathbf{E}$ [53–55], where α is the electric polarizability given by

$$\alpha = \frac{\alpha_0}{1 - i(2/3)k^3\alpha_0}, \quad \alpha_0 = 4\pi\epsilon_1 a^3 \frac{\epsilon_2/\epsilon_1 - 1}{\epsilon_2/\epsilon_1 + 2}, \quad (5.12)$$

As it is known, when a CVV beam is tightly focused on a Rayleigh nanoparticle, the optical force exerted on the particle can be calculated in the dipole approximation

$$\mathbf{F} = (\mathbf{p} \cdot \nabla) \mathbf{E} + (1/c)(\partial \mathbf{p} / \partial t) \times \mathbf{B}, \quad (5.13)$$

where c is the light speed in vacuum and \mathbf{B} is the magnetic induction. Therefore, the time-averaged optical force is given by [56, 57]

$$\langle \mathbf{F} \rangle = \frac{1}{2} \text{Re}[\alpha E_j \partial_i (E_j)^*], \quad (5.14)$$

where i and j denote the Cartesian components (x, y, z) , and the dummy index means a summation.

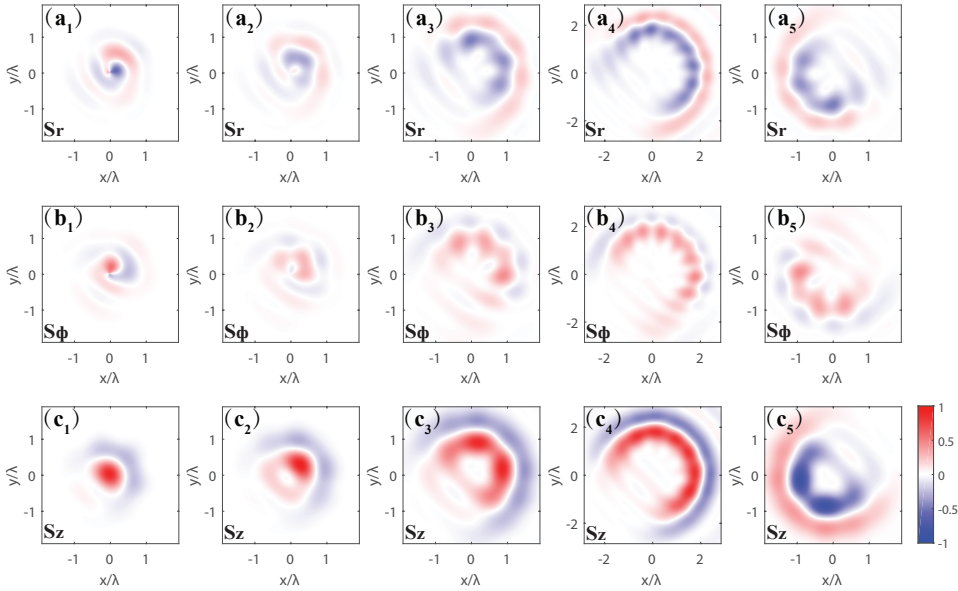


Figure 5.13: Normalized SAM density distributions in the focal plane for the CVV input beams with broken axial symmetry $b = 3\pi/2$ and initial phase $\varphi_0 = \pi/4$. Topological numbers change from left column to right: $m = 1, 2, 4, 8$ and -4 , respectively. The first, second and third rows are the radial, azimuthal and longitudinal components of the SAM density.

Just like transferring linear momentum from light to a particle generates an optical force on the particle, transferring AM to particle produces an optical torque $\mathbf{\Gamma} = \mathbf{p} \times \mathbf{E}$. When the electric field \mathbf{E} of the CVV beam oscillates harmonically in time, the time-averaged optical spin torque becomes

$$\mathbf{\Gamma} = \frac{1}{2} |\alpha|^2 \text{Re} \left[\frac{1}{\alpha_0^*} \mathbf{E} \times \mathbf{E}^* \right], \quad (5.15)$$

Therefore, the three orthogonal components of the torque are given in cylindrical coordinates by

$$\begin{aligned} \Gamma_r &= \frac{1}{2} |\alpha|^2 \text{Re} \left[\frac{1}{\alpha_0^*} (E_\phi E_z^* - E_z E_\phi^*) \right], \\ \Gamma_\phi &= \frac{1}{2} |\alpha|^2 \text{Re} \left[\frac{1}{\alpha_0^*} (E_z E_r^* - E_r E_z^*) \right], \\ \Gamma_z &= \frac{1}{2} |\alpha|^2 \text{Re} \left[\frac{1}{\alpha_0^*} (E_r E_\phi^* - E_\phi E_r^*) \right]. \end{aligned} \quad (5.16)$$

5.3.2. Particle's motion with symmetrical CVV beams

Figure 5.14 shows the three-dimensional optical spin torque distributions in the focal plane. An absorptive sphere with refractive index $n_2 = 1.59 + 0.005i$ is placed

in a general focused CVV field with topological charges $m = \pm 4$ (Figs. 5.14(a) and 5.14(b)) and $\varphi_0 = \pi/4$. The size of the particle is $a = 30nm$. The green arrows indicate the direction of the optical torque, while the magnitude has been normalized. The torque has the same magnitude but opposite direction for opposite signs of m . The reversion is due to the change of the directions of the SAM density shown in Fig. 5.6. Compared with Eqs. 5.9 and 5.16, it is easy to find that the torque is proportional to the SAM density. Figures 5.14(c) and 5.14(d) display the motions of the spheres at hot-spots with the corresponding topological charges in Figs. 5.14(a) and 5.14(b). The green arrows and circles are the orientations of the spinning and the orbital motions, respectively. The spheres can be trapped at the hot spot of the maximum intensities. Such orientations depend on the illumination polarization as well as topological charge signs.

The influences of the topological charge m (OAM) on the local maximum values

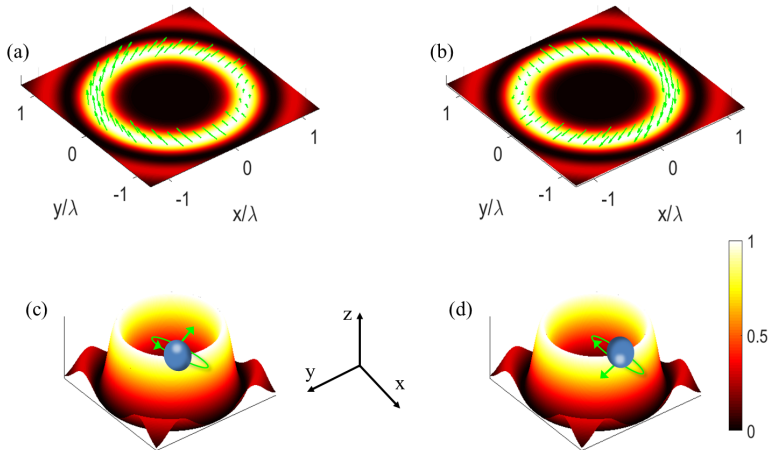


Figure 5.14: Three-dimensional optical torque Γ distributions in the focused fields of general CVV beams with $\varphi_0 = \pi/4$ and topological charges (a) $m=4$ and (b) $m=-4$. The corresponding spin and orbital motions of trapped absorptive spheres illuminated by the same focal beams with (c) $m=4$ and (d) $m=-4$.

of optical torque at the hot-spot position versus the angle φ_0 are presented in Fig. 5.15. In Figs. 5.15(a)-5.15(c), it can be seen that for different topological charges, the three torque components vary as a function of φ_0 in similar ways. The maximum longitudinal spin torque at the hot-spot dominates in the three components for any values of angle φ_0 . Γ_z starts from minimum value when $\varphi_0 = 0$ and increases gently to the maximum value somewhere when $\varphi_0 = \pi/2$. However, the local maximum azimuthal torque decreases from maximum value to zero till φ_0 increases to $\pi/2$. Meanwhile, the local maximum value of radial torque starts from minimum value zero when $\varphi_0 = 0$, and increases until $\varphi_0 = \pi/4$, then it decreases together with

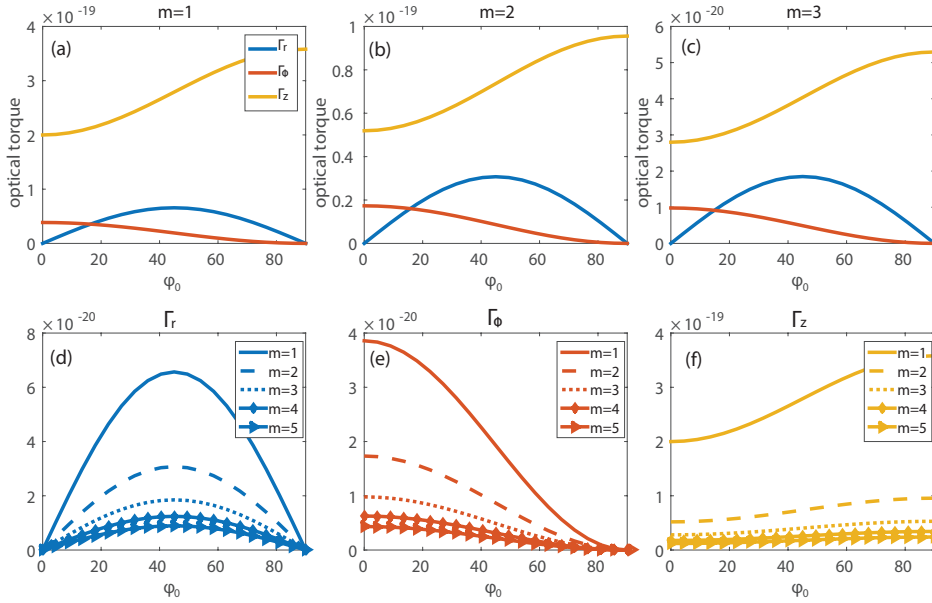


Figure 5.15: Three components of local maximum optical torques Γ at the hot-spots in the focused fields of CVV beams with topological charges (a) $m=1$, (b) $m=2$ and (c) $m=3$ versus the angle φ_0 changes from 0 to 2π . Different colors refers to different components: blue-the radial torque, red-the azimuthal torque and yellow-longitudinal torque. For comparison, (d)-(f) show the variations of each maximal optical torque components at the hot-spot as the topological charge changes from 1 to 5 and φ_0 changes from 0 to 2π . Different line styles represent different topological charges.

the radial torque till $\varphi_0 = \pi/2$. The amplitudes of the local maximum optical torque decrease with the topological charge increases. In order to make it clear to observe, Figs. 5.15(d)-5.15(f) plot variations of each maximal optical torque component at the hot-spot separately. The colors of lines agree with the three components in the above subplots (Figs. 5.15(a)-5.15(c)), and different line styles represent different topological charges. The trends in each case are similar to the examples in Figs. 5.15(a)-5.15(c). With the increase of m , the values of local maximal optical torques decrease. Another common point is that the fluctuation goes more slightly when m increases, which means the influences of the topological charge on the local maximal values of optical torques at the hot-spot position become tiny, and so as the influences come from the initial phase φ_0 .

5.3.3. Particle's motion with asymmetrical CVV beams

We now discuss the optical force experienced by a Rayleigh nanosphere in the focal field of a normal CVV input beam and a CVV beam with broken axial symmetry. The sphere has the same parameters as that in Fig. 5.14 and it is placed in the focused CVV beam with the initial phase $\varphi_0 = \pi/4$ and topological charge $m = \pm 6$. The transverse optical forces in the focal plane can be seen in Fig. 5.16. The

black arrows indicate the directions of the optical force and they point together to the maximum values of the intensity distribution (hot-spots) in the bright circle as shown in Figs. 5.16(a) and 5.16(c) with opposite topological charges. As a result, the nanosphere can be trapped around the optical axis. The sphere orbits clockwise for $m = 6$, whereas it orbits counterclockwise for $m = -6$ around the z -axis. In Figs. 5.16(b) and 5.16(d), the intensity distributions of optical force are shown for an input CVV beam with a sector aperture $b = \pi$ with topological charge $m = \pm 6$. Even though there is asymmetry, the optical forces still point to the hot-spots. Due to the sign of the topological charge, the spheres move along the blue solid lines around the optical axis in two opposite directions: clockwise (Fig.5.16(b)) and counterclockwise (Fig.5.16(d)). As the sign of the topological charge m is related to the optical OAM, the results in Fig.5.16 give an explanation of transfer of OAM to the particle with symmetrical and asymmetrical illuminations.

Figure 5.17 displays the sketch of the spin and orbital motion of the nanoparti-

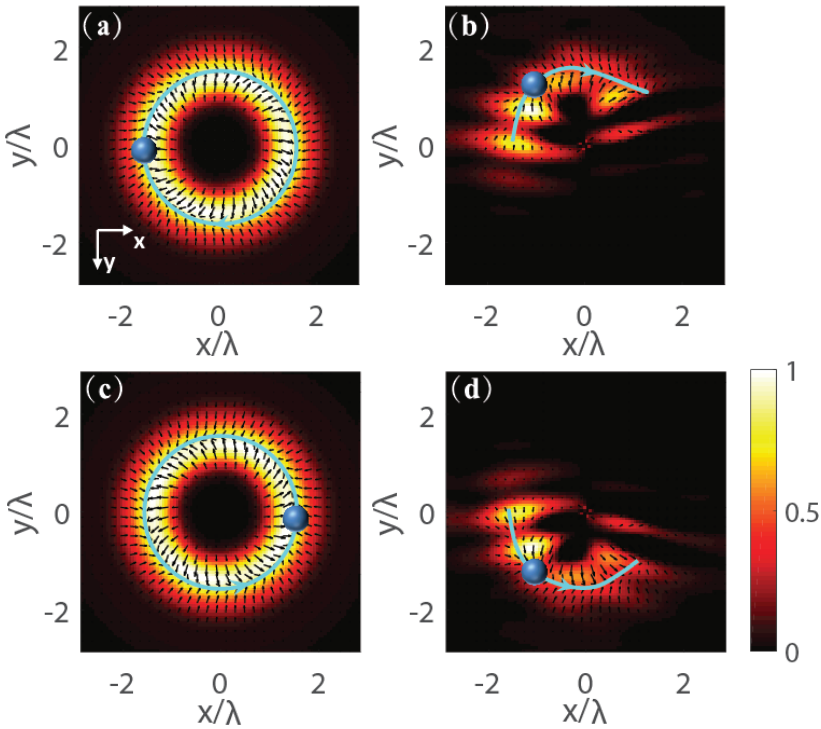


Figure 5.16: Transverse force distributions focused by the symmetrical CVV beams with the topological charges of (a) $m = 6$ and (c) $m = -6$, and by asymmetrical CVV beams ($b = \pi$) with the topological charges of (b) $m = 6$ and (d) $m = -6$. The initial phase $\varphi_0 = \pi/4$.

cle under the excitation of the CVV beams with different sector apertures $b = 2\pi$, $b = \pi$ and $b = 3\pi/2$ in columns, respectively. The topological charges are $m = 6$ and $m = -6$ in the upper and bottom rows. Regardless of whether the input CVV

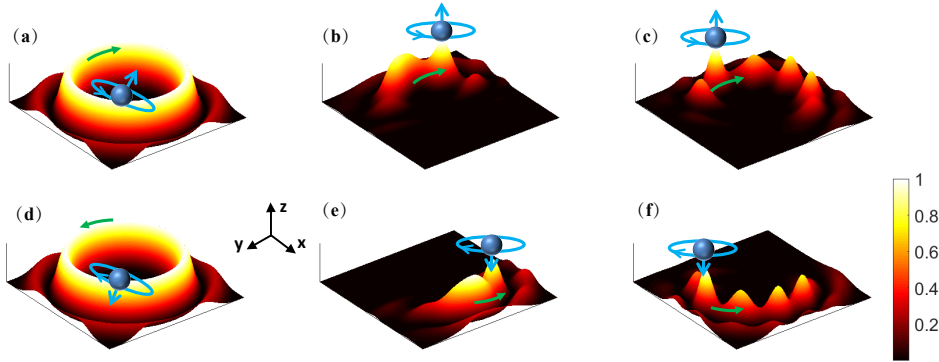


Figure 5.17: Three-dimensional optical torque Γ distributions in the focused fields of input CVV beams with sector apertures $b = 2\pi$ for (a) and (d), $b = \pi$ for (b) and (e), and $b = 3\pi/2$ for (c) and (f). The topological charge $m = 6$ for the upper three figures and $m = -6$ for the bottom three figures. The initial phase $\varphi_0 = \pi/4$.

beam is symmetrical or not, the particle can be trapped at the intensity maxima (hot-spots) as indicated with green arrows. The green arrows represent the orbital motion directions of the particle around the z -axis, which are determined by the signs of the topological charge. The blue up and down arrows correspond to the directions of the optical torques that determine the spinning motions of the sphere. It can be found that the sphere experiences a counterclockwise motion with the topological charge $m = 6$ (Figs. 5.17(a)-5.17(c)), and a clockwise motion for $m = -6$ (Figs. 5.17(d)-5.17(f)). By considering Eqs. 5.8 and 5.15, and combining the simulated results of the SAM density distributions in Figs. 5.13(a₃)-5.13(c₃), Figs. 5.13(a₅)-5.13(c₅), and the three dimensional orientations of the spin torques in Fig. 5.17, we can conclude that the spin torque on the nanosphere comes from the transfer of the SAM from the incident light beam to the particle.

Figure 5.18 considers the influence of the topological charge m (OAM) on the local maximum values of three components of optical torque at hot-spots versus the initial phase φ_0 . For comparison, the results obtained by the symmetrical illuminations are taken into account firstly, see in Figs. 5.18(a)-5.18(c). The properties are the same as that in Figs. 5.15(d)-5.15(f). The similar trends observed in the case of asymmetrical input CVV beams with $b = \pi$ (Figs. 5.18(d)-5.18(f)), but the radial torque behaves differently. The transverse components of the optical torque decrease monotonically (Figs. 5.18(d) and 5.18(e)). One common point is that the longitudinal torque is the dominant component of the optical torque, regardless of whether the CVV excitation is symmetrical or not. Another common point for both conditions of the symmetrical and asymmetrical CVV excitations is the curve fluctuates less when the topological charge m increases, which means the influence of the topological charge on the local maximal values of optical torques at the hot-spot position becomes tiny. And also the influence of the initial phase φ_0 becomes weak. As mentioned previously, optical torque is related to the SAM density. Discussions

such as the preceding one can help us understand the interaction between the OAM and SAM, and in addition, they can also provide a guide to trapped particle motions with symmetrical and asymmetrical focused CVV beams.

The motion of the particle not only depends on the illumination light, but also is

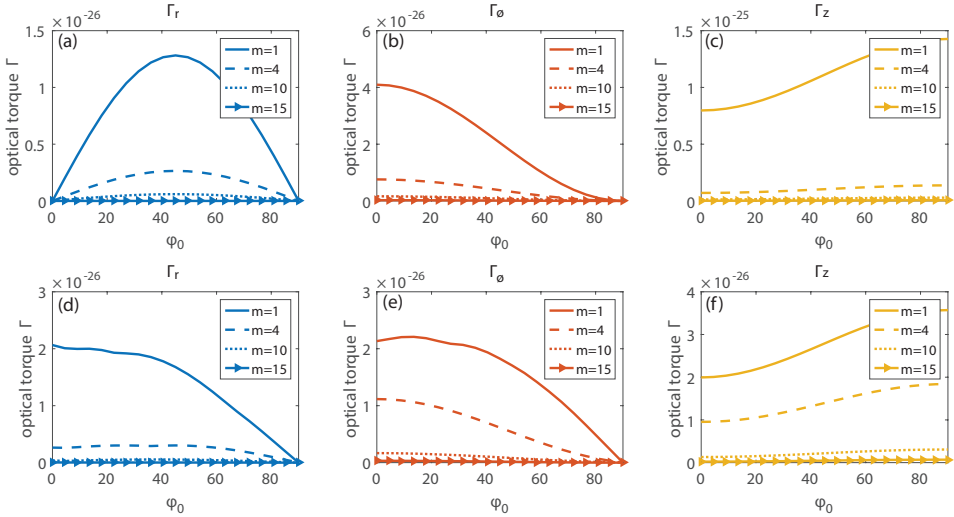


Figure 5.18: Variations of the maximal optical torque components at the hot-spot as the topological charge m changes from 1 to 15 and the initial phase φ_0 changes from 0 to 2π . For comparison, (a)-(c) are three components of optical torques with symmetrical CVV input beams, while (d)-(f) correspond to asymmetrical CVV input beams with a sector aperture $b = \pi$. Different colors refer to different components: blue-the radial torque, red-the azimuthal torque and yellow-the longitudinal torque. Different line styles represent different topological charges.

affected by the characteristics of the nanoparticle. Figure 5.19 shows how the total optical torques at the hot-spots depend on the particle's size and materials. The trend of lines is similar in all conditions: the optical torque is largest when the particle is excited by the CVV beam with broken axial system $b = 3\pi/2$, and smallest with the CVV beam with $b = \pi/2$. The other two cases ($b = \pi$ and symmetrical CVV beam) are in between. In Fig. 5.19(a), the total optical torques change as a function of the radius of nanoparticle a for a fixed refractive index $n_2 = 1.59 + 0.005i$ under the illuminations of symmetrical (green lines) and asymmetrical (other color lines) input CVV beams with topological charges $m = 6$ (solid lines) and $m = -6$ (dashed lines), respectively. When the radius of the nanoparticle is 70nm in each case, the total optical torque reaches its maximum, which means this is the optimal size for the trapping particle of that particular material. Figures 5.19(b) and (c) show the dependence of the optical torque on the particle's complex refractive index. The particle has a fixed radius $a = 30\text{nm}$. In Fig. 5.19(b), we fix the imaginary part of the refractive index at 0.005 and let the real part vary from 1 to 4. It is noticed that the strength of the optical torque decreases as the real part increases. When fixing the real part of the refractive index at 1.59 and varying the imaginary part in

the range of $[0, 0.1]$, the optical torque grows with the increase of the imaginary part. Therefore, to get large optical torque of the trapping particle, the dimension and the material need to be chosen properly.

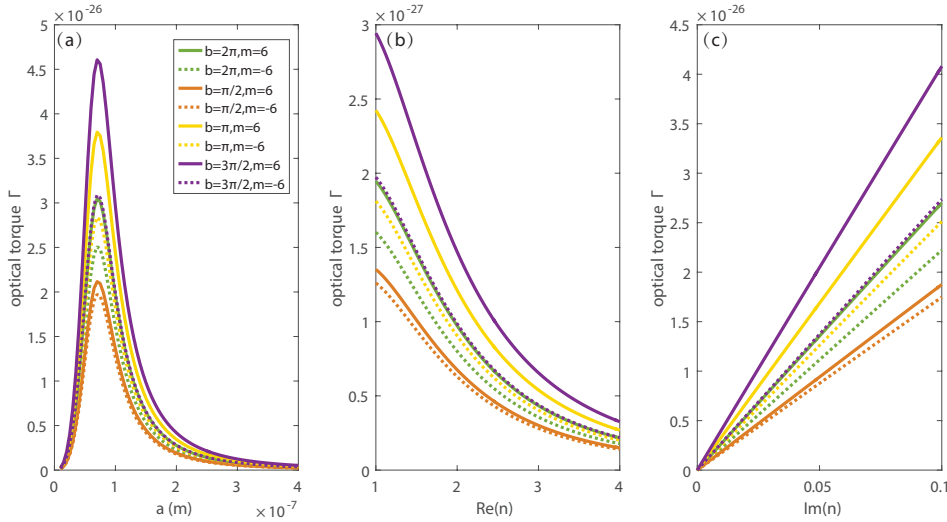


Figure 5.19: The changes of the maximal total optical torques at hot-spots exerted on the nanosphere with varying radius a (a), real part (b) and imaginary part of the refractive index under illuminations of symmetrical (green lines) and asymmetrical (other color lines) input CVV beams with topological charges $m = 6$ (solid lines) and $m = -6$ (dashed lines).

5.4. Conclusion

To summarize, we have proposed theoretical investigations on electric field and AM properties of arbitrary highly focused symmetrical and asymmetrical CVV beams. With Richard-Wolf vectorial focusing theory, all components of the electric field near the focus can be obtained, as well as the SAM density produced by the focal field. It is revealed that the properties of the input beam such as the polarization state, the topological charge and initial phase can affect the SAM distribution. The interaction between the SAM and OAM is demonstrated by changing the topological charge m . The redistributions of SAM density are due to the spin flux, which originates from the changes of OAM. The sign of m only changes the direction of longitudinal SAM density and the sign of the initial phase φ_0 only changes the direction of transverse SAM density. Compared with the case of symmetrical input CVV beam, the symmetry of the focal field is broken if the illumination is an asymmetrical CVV beam, and the three field components at focus can be rotated by an angle of $\pi/2$ with respect to the input beam. In particular, the optical forces and torques of the highly focused CVV beam on an absorptive nanosphere are discussed. The sphere can be trapped, moving clockwise or counterclockwise around the optical axis and is confined to the hot-spot of the maximal optical torque and rotates around itself,

no matter with the normal CVV beam or the beam with broken axial symmetry. The motion directions are determined by the sign of topological charge, which confirms the interaction between OAM and SAM. Finally, it is noted that the optical torque can be optimized by choosing the size and material of the trapped particle properly. These findings make the particles' motion under the illumination of the CVV beams predictable and controllable, which will be helpful in achieving good performance in optical manipulation and particle transport in highly focusing optical systems.

References

- [1] P. Meng, Z. Man, A. P. Konijnenberg, and H. P. Urbach, *Angular momentum properties of hybrid cylindrical vector vortex beams in tightly focused optical systems*, *Optics Express* **27**, 35336 (2019).
- [2] P. Couillet, L. Gil, and F. Rocca, *Optical vortices*, *Optics Communications* **73**, 403 (1989).
- [3] Y. Shen, X. Wang, Z. Xie, C. Min, X. Fu, Q. Liu, M. Gong, and X. Yuan, *Optical vortices 30 years on: Oam manipulation from topological charge to multiple singularities*, *Light: Science & Applications* **8**, 1 (2019).
- [4] H. He, M. E. J. Friese, N. R. Heckenberg, and H. Rubinsztein-Dunlop, *Direct observation of transfer of angular momentum to absorptive particles from a laser beam with a phase singularity*, *Phys. Rev. Lett.* **75**, 826 (1995).
- [5] L. Paterson, M. P. MacDonald, J. Arlt, W. Sibbett, P. Bryant, and K. Dholakia, *Controlled rotation of optically trapped microscopic particles*, *Science* **292**, 912 (2001).
- [6] M. P. MacDonald, L. Paterson, K. Volke-Sepulveda, J. Arlt, W. Sibbett, and K. Dholakia, *Creation and manipulation of three-dimensional optically trapped structures*, *Science* **296**, 1101 (2002).
- [7] D. G. Grier, *A revolution in optical manipulation*, *Nature* **424**, 810 (2003).
- [8] M. Padgett and R. Bowman, *Tweezers with a twist*, *Nature photonics* **5**, 343 (2011).
- [9] Z. Shen, Z. Hu, G. Yuan, C. Min, H. Fang, and X. Yuan, *Visualizing orbital angular momentum of plasmonic vortices*, *Optics Letters* **37**, 4627 (2012).
- [10] G. Li, S. Chen, N. Pholchai, B. Reineke, P. W. H. Wong, E. Y. B. Pun, K. W. Cheah, T. Zentgraf, and S. Zhang, *Continuous control of the nonlinearity phase for harmonic generations*, *Nature Materials* **14**, 607 (2015).
- [11] S. Keren-Zur, O. Avayu, L. Michaeli, and T. Ellenbogen, *Nonlinear beam shaping with plasmonic metasurfaces*, *ACS Photonics* **3**, 117 (2015).

- [12] G. Musarra, K. Wilson, D. Faccio, and E. M. Wright, *Rotation-dependent non-linear absorption of orbital angular momentum beams in ruby*, *Optics Letters* **43**, 3073 (2018).
- [13] K. Toyoda, F. Takahashi, S. Takizawa, Y. Tokizane, K. Miyamoto, R. Morita, and T. Omatsu, *Transfer of light helicity to nanostructures*, *Phys. Rev. Lett.* **110**, 143603 (2013).
- [14] S. Syubaev, A. Zhizhchenko, A. Kuchmizhak, A. Porfirev, E. Pustovalov, O. Vitrik, Y. Kulchin, S. Khonina, and S. Kudryashov, *Direct laser printing of chiral plasmonic nanojets by vortex beams*, *Optics Express* **25**, 10214 (2017).
- [15] F. Takahashi, K. Miyamoto, H. Hidai, K. Yamane, R. Morita, and T. Omatsu, *Picosecond optical vortex pulse illumination forms a monocrystalline silicon needle*, *Scientific Reports* **6**, 21738 (2016).
- [16] P. Tan, X. Yuan, G. Yuan, and Q. Wang, *High-resolution wide-field standing-wave surface plasmon resonance fluorescence microscopy with optical vortices*, *Applied Physics Letters* **97**, 241109 (2010).
- [17] K. I. Willig, S. O. Rizzoli, V. Westphal, R. Jahn, and S. W. Hell, *Sted microscopy reveals that synaptotagmin remains clustered after synaptic vesicle exocytosis*, *Nature* **440**, 935 (2006).
- [18] L. Allen, S. M. Barnett, and M. J. Padgett, *Optical angular momentum* (Chemical Rubber Company, 2016).
- [19] D. L. Andrews and M. Babiker, *The angular momentum of light* (Cambridge University, 2012).
- [20] A. T. O'Neil, I. MacVicar, L. Allen, and M. J. Padgett, *Intrinsic and extrinsic nature of the orbital angular momentum of a light beam*, *Phys. Rev. Lett.* **88**, 053601 (2002).
- [21] L. Allen, M. W. Beijersbergen, R. J. C. Spreeuw, and J. P. Woerdman, *Orbital angular momentum of light and the transformation of laguerre-gaussian laser modes*, *Phys. Rev. A* **45**, 8185 (1992).
- [22] K. Y. Bliokh, E. A. Ostrovskaya, M. A. Alonso, O. G. Rodríguez-Herrera, D. Lara, and C. Dainty, *Spin-to-orbital angular momentum conversion in focusing, scattering, and imaging systems*, *Optics Express* **19**, 26132 (2011).
- [23] A. Aiello, P. Banzer, M. Neugebauer, and G. Leuchs, *From transverse angular momentum to photonic wheels*, *Nature Photonics* **9**, 789 (2015).
- [24] K. Y. Bliokh, F. J. Rodríguez-Fortuño, F. Nori, and A. V. Zayats, *Spin-orbit interactions of light*, *Nature Photonics* **9**, 796 (2015).
- [25] L. Allen, M. W. Beijersbergen, R. Spreeuw, and J. Woerdman, *Orbital angular momentum of light and the transformation of laguerre-gaussian laser modes*, *Phys. Rev. A* **45**, 8185 (1992).

- [26] V. Garcés-Chávez, D. McGloin, M. Padgett, W. Dultz, H. Schmitzer, and K. Dhoklaka, *Observation of the transfer of the local angular momentum density of a multiringed light beam to an optically trapped particle*, *Phys. Rev. Lett.* **91**, 093602 (2003).
- [27] A. Lehmuskero, R. Ogier, T. Gschneidner, P. Johansson, and M. Käll, *Ultrafast spinning of gold nanoparticles in water using circularly polarized light*, *Nano Letter* **13**, 3129 (2013).
- [28] M. Onoda, S. Murakami, and N. Nagaosa, *Hall effect of light*, *Phys. Rev. Lett.* **93**, 083901 (2004).
- [29] V. S. Liberman and B. Y. Zel'dovich, *Spin-orbit interaction of a photon in an inhomogeneous medium*, *Phys. Rev. A* **46**, 5199 (1992).
- [30] L. Marrucci, C. Manzo, and D. Paparo, *Optical spin-to-orbital angular momentum conversion in inhomogeneous anisotropic media*, *Phys. Rev. Lett.* **96**, 163905 (2006).
- [31] Z. Bomzon, M. Gu, and J. Shamir, *Angular momentum and geometrical phases in tight-focused circularly polarized plane waves*, *Appl. Phys. Lett.* **89**, 241104 (2006).
- [32] M. Rashid, O. M. Maragò, and P. H. Jones, *Focusing of high order cylindrical vector beams*, *Journal of Optics A: Pure and Applied Optics* **11**, 065204 (2009).
- [33] J. Pu and Z. Zhang, *Tight focusing of spirally polarized vortex beams*, *Optics & Laser Technology* **42**, 186 (2010).
- [34] S. N. Khonina, *Vortex beams with high-order cylindrical polarization: features of focal distributions*, *Applied Physics B* **125**, 100 (2019).
- [35] P. Shi, L. Du, and X. Yuan, *Structured spin angular momentum in highly focused cylindrical vector vortex beams for optical manipulation*, *Optics Express* **26**, 23449 (2018).
- [36] L. Han, S. Liu, P. Li, Y. Zhang, H. Cheng, and J. Zhao, *Catalystlike effect of orbital angular momentum on the conversion of transverse to three-dimensional spin states within tightly focused radially polarized beams*, *Phys. Rev. A* **97**, 053802 (2018).
- [37] M. Li, Y. Cai, S. Yan, Y. Liang, P. Zhang, and B. Yao, *Orbit-induced localized spin angular momentum in strong focusing of optical vectorial vortex beams*, *Phys. Rev. A* **97**, 053842 (2018).
- [38] P. Yu, Q. Zhao, X. Hu, Y. Li, and L. Gong, *Orbit-induced localized spin angular momentum in the tight focusing of linearly polarized vortex beams*, *Optics Letters* **43**, 5677 (2018).

- [39] S. N. Khonina and I. Golub, *Generation of an optical ball bearing facilitated by coupling between handedness of polarization of light and helicity of its phase*, *J. Opt. Soc. Am. B* **36**, 2087 (2019).
- [40] Q. Zhan, *Cylindrical vector beams: from mathematical concepts to applications*, *Advances in Optics and Photonics* **1**, 1 (2009).
- [41] K. S. Youngworth and T. G. Brown, *Focusing of high numerical aperture cylindrical-vector beams*, *Optics Express* **7**, 77 (2000).
- [42] T. Bauer, M. Neugebauer, G. Leuchs, and P. Banzer, *Optical polarization möbius strips and points of purely transverse spin density*, *Phys. Rev. Lett.* **117**, 013601 (2016).
- [43] W. Zhu, V. Shvedov, W. She, and W. Krolikowski, *Transverse spin angular momentum of tightly focused full poincaré beams*, *Optics Express* **23**, 34029 (2015).
- [44] S. N. Khonina, *Simple phase optical elements for narrowing of a focal spot in high-numerical-aperture conditions*, *Optical Engineering* **52**, 091711 (2013).
- [45] G. Milione, A. Dudley, T. A. Nguyen, O. Chakraborty, E. Karimi, A. Forbes, and R. R. Alfano, *Measuring the self-healing of the spatially inhomogeneous states of polarization of vector besse beams*, *Journal of Optics* **17**, 035617 (2015).
- [46] L. Hang, Y. Wang, and P. Chen, *Symmetry of electric spin angular momentum density in the tight focusing of linearly polarized vortex beams*, *J. Opt. Soc. Am. A* **36**, 1374 (2019).
- [47] J. A. Davis and J. B. Bentley, *Azimuthal prism effect with partially blocked vortex-producing lenses*, *Optics Letters* **30**, 3204 (2005).
- [48] S. Franke-Arnold, S. M. Barnett, E. Yao, J. Leach, J. Courtial, and M. Padgett, *Uncertainty principle for angular position and angular momentum*, *New Journal of Physics* **6**, 103 (2004).
- [49] X. Wang, K. Lou, J. Chen, B. Gu, Y. Li, H. Wang, et al., *Unveiling locally linearly polarized vector fields with broken axial symmetry*, *Phys. Rev. A* **83**, 063813 (2011).
- [50] Z. Man, L. Du, Y. Zhang, C. Min, S. Fu, and X. Yuan, *Focal and optical trapping behaviors of radially polarized vortex beam with broken axial symmetry*, *AIP Advances* **7**, 065109 (2017).
- [51] Y. Zhang, Y. Xue, Z. Zhu, G. Rui, Y. Cui, and B. Gu, *Theoretical investigation on asymmetrical spinning and orbiting motions of particles in a tightly focused power-exponent azimuthal-variant vector field*, *Optics Express* **26**, 4318 (2018).

- [52] C. Maurer, A. Jesacher, S. Fürhapter, S. Bernet, and M. Ritsch-Marte, *Tailoring of arbitrary optical vector beams*, [New Journal of Physics](#) **9**, 78 (2007).
- [53] B. T. Draine, *The discrete-dipole approximation and its application to interstellar graphite grains*, [The Astrophysical Journal](#) **333**, 848 (1988).
- [54] M. Li, S. Yan, Y. Liang, P. Zhang, and B. Yao, *Spinning of particles in optical double-vortex beams*, [Journal of Optics](#) **20**, 025401 (2018).
- [55] P. C. Chaumet and M. Nieto-Vesperinas, *Time-averaged total force on a dipolar sphere in an electromagnetic field*, [Optics Letters](#) **25**, 1065 (2000).
- [56] A. Canaguier-Durand, A. Cuche, C. Genet, and T. W. Ebbesen, *Force and torque on an electric dipole by spinning light fields*, [Phys. Rev. A](#) **88**, 033831 (2013).
- [57] D. B. Ruffner and D. G. Grier, *Optical forces and torques in nonuniform beams of light*, [Phys. Rev. Lett.](#) **108**, 173602 (2012).

6

Conclusion and outlook

6.1. Conclusion

In this thesis, we aim to shape the focal spot for two main purposes. The first one is to apply it in an optical system to improve its image performance (chapters 2-4). The second is to understand the motion of nanoparticles driven by a focused light beam (chapter 5).

According to the Rayleigh criterion, the lateral resolution is limited by the wavelength and the NA of the objective lens. Therefore, we start our work from analyzing the focusing properties in high NA systems with the Richards-Wolf vectorial theory. On the basis of the fact that the radially polarized light creates sharper focal spot than linearly polarized light due to the tight longitudinal component, the radial polarization state can be considered in order to increase the resolution of a confocal imaging system. In addition, by considering amplitude modulation, such as annular and optimized pupil field, even smaller focal spots can be achieved. In most commercial confocal microscopes, the light source is laser light without considering its polarization. Here, we use modulated radially polarized laser beam to illuminate the sample in the confocal imaging set-up to improve the lateral resolution further. It is demonstrated theoretically that the smallest resolved distance between two identical longitudinal dipoles is 0.36λ with $NA=0.9$, which is beyond the diffraction limit compared with the conventional confocal microscope. Experimental result shows good agreement with the theoretical calculation. An experimental confocal set-up to shape and focus a laser beam of the wavelength $\lambda = 632nm$ by a high NA objective lens on the sample is designed, built and tested. The experimental realization involves many optical elements including polarization convertors, SLM, single mode fiber, and piezo electric-driven translator stage. Special attention has been given to the sample scanning procedure, controlled by the LabView programs.

The question 'Can we improve the performance of the imaging system further after the illumination is optimized?' motivates us to modify the sample substrate. The design of the substrate is such that evanescent waves generated by the ob-

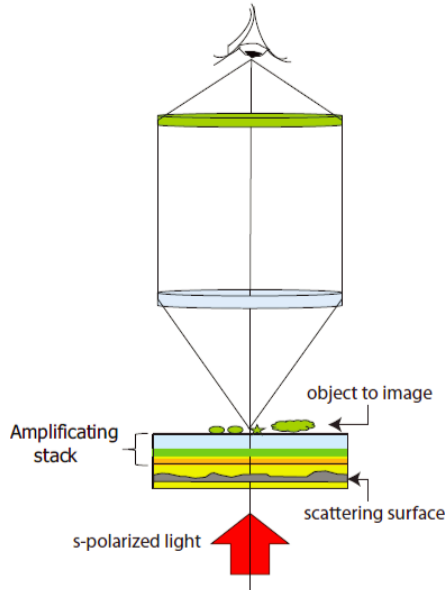
ject placed on it can be enhanced and re-scattered in the far field, resulting in super-resolution effect. The evanescent wave amplification structure we consider is simply a thin TiO_2 film layer on the top of the original glass substrate. This is easier to realize than other meta-material structures that have been suggested in the literature. We validate the idea by analyzing the problem of a dipole scattering on an interface analytically, building two nanospheres numerically using the Lumerical software and finally calculating the far field image in a wide field microscopy setup.

The second part of the thesis regards the focusing properties and angular momentum of symmetrical and asymmetrical CVV beams to consider the effect of the phase of the light to shape the focus. The spin and orbital coupling is demonstrated by adjusting the different parameters such as the topological charge and the initial phase of the light. The interaction between the SAM and OAM also reveals on the optical torque and force when an absorptive nanosphere is introduced, which makes the motion of the nanoparticles predictable and controllable.

6.2. Outlook

Regarding the work we have proposed involving the high spatial frequency information carried by the amplified evanescent wave, one may envision plenty of useful applications such as far field microscopy (see in Fig. 6.1).

We show the design of a simple evanescent wave enhanced structure in chapter



FAR FIELD MICROSCOPY

Figure 6.1: Far field microscopy application of the amplifying stack for evanescent waves.

4 and, to understand the problem, we use an analytical model of one dipole on the interface combining with the FDTD method to calculate numerically the far field of two nanospheres on the designed substrate. If multiple particles exist, rigorous analytical method is necessary. For instance, to consider the near field of two dipoles next to each other on the proposed substrate, it is helpful to understand the complicated interactions between the original focal field, the enhanced layer, and the two dipoles. The iterative algorithm and convergence speed should be taken into account.

The work in chapter 4 is inspired by the previous work on coherent Fourier scatterometry (CFS) for particle detection [1]. Besides the improvement of the imaging quality, the detection sensitivity of particles on a substrate is also highly enhanced by using the principle of evanescent-wave amplification [2]. However, all the designed substrate applied in these papers are simple because of the purpose of achieving a first demonstration of its application. Studying material absorption of dielectric films provides another way to observe the evanescent enhancement. A dielectric stack that is properly designed to reach a total absorption (100%) which corresponds to an enhancement maximum is discussed in Ref [3]. Therefore, the enhancement layer can be optimized by investigating the light transmission and reflection, as well as the absorption through the multilayer structure (see in Fig. 6.2). By appropriately optimizing the thickness and reasonably choosing the material for each layer, the evanescent enhancement would be further improved.

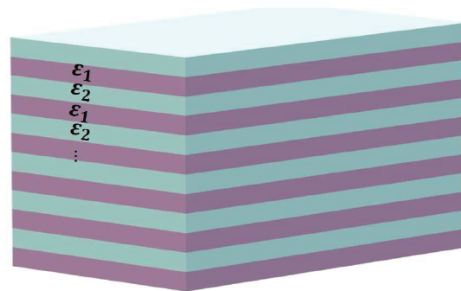


Figure 6.2: An example of one dimensional multilayer photonic structure consisting of two repeating materials with dielectric constants ϵ_1 and ϵ_2 .

References

- [1] S. Roy, S. F. Pereira, H. P. Urbach, X. Wei, and O. El Gawhary, *Exploiting evanescent-wave amplification for subwavelength low-contrast particle detection*, *Phys. Rev. A* **96**, 013814 (2017).
- [2] D. Kolenov, P. Meng, and S. Pereira, *A highly sensitive laser focus positioning method with sub-micrometre accuracy using coherent fourier scatterometry*, *Measurement Science and Technology* **31**, 064007 (2020).

- [3] C. Ndiaye, F. Lemarchand, M. Zerrad, D. Ausserré, and C. Amra, *Optimal design for 100% absorption and maximum field enhancement in thin-film multilayers at resonances under total reflection*, [Applied Optics](#) **50**, C382 (2011).

Acknowledgements

Now my thesis comes to the end together with my PhD study. The work presented here would not be possible without a lot of help and support from dozens of individuals in the past four years.

First of all, I would like to express the deep gratitude to my promotor, Prof. Dr. H. Paul Urbach, and my daily supervisor Assoc. Prof. Dr. Sylvania F. Pereira. Paul, thank you for your critical inputs and reviews. The way you analyzed a complex physical problem starting from a simple mathematical model is really helpful to shape my own scientific thinking. Thanks for giving me freedom to pursue the research direction I am interested in and supporting me with valuable recommendations. Sylvania, thank you for guiding me on the daily basis through the whole period. I strongly appreciate your incredible patience, enormous efforts and time to help with experimental realization and theoretical interpretation of the results. You are an excellent female scientist and I learned a lot from you. Moreover, I thank all the committee members for reading and comments on my thesis.

I would like to thank Thomas Siefke from Friedrich Schiller University, Jena for the fabrication of the nanolayer on the substrate to perform the experiments in chapter 4. I also acknowledge the Optics Research Group experimental support team of Roland and Thim. You create a safe lab environment and because of you, my experiment went smoothly. Thank you Roland for helping me with all the software and computer problems. Thank you Thim for always being available to provide optical components requested for my set-up. Thanks to the internship student Hong-Liên Pham for helping me to scan the sample in the cleanroom again and again. Thanks to the bachelor student Ahmed for building and testing the imaging system with me at the early stage of the experiment. Thanks Milad for helping me to take the data of Fig. 4.12.

Life is not easy for a PhD student. Thank you Yvonne for your support and assistance in all the administrative problems and private life. It is enjoyable to talk with you because of your optimistic attitude on the life. A special thanks to Dr. Nandini for the constant encouragement during my tough period. I would also like to extend my thanks to all the other Optics staff members, Aurele, Gao, Florian, Omar, Joseph, Wim, Peter and Jeff.

Now, I thank all my colleagues in the Optics group. Sander Konijnenberg, I deeply thank you for helping me, teaching me and for all the interesting and fruitful discussions we had. I thank my one year office mate, the visiting researcher Dr. Man to provide valuable advice on the last chapter of my thesis. Special thanks need to be given to Xiujie. Thank you for teaching me the Lumerical software. You are a good time planner, and I am grateful for your constant encouragement. I wish you a successful scientific career! Thanks Dmytro for sharing your research experience with me and it is nice to collaborate with you. Thank you Xukang for your assistance

with the research work and life. I also thank you Po-Ju and Polly for sharing your stories, and listening to my difficulties, worries and complains. Bingxin, thank you for your company at the end of my PhD study and making me addicted to work at night efficiently. Sven, it is nice to talk with you and thanks for practising Dutch with me. I would like to express my thank to all others who contributed in some or other way: Anna, Alex, Boling, Chengliang, Felliipe, Guang, Hamed, Iman, Jin, Katsiaryna, Lauryna, Lei, Matthias, Macro, Min, Paolo, Po-Sheng, Priya, Thomas, Yao, Yifeng, Ying, Yuquan, Yuxin, Zhe, Zhongwen, Zheng (Xi), Zheng (Zhu). All the best for all of you.

From outside of the Optics group, I would like thank to the staff from the Kavil Nanolab group who gave me a training for working in the cleanroom. Thanks to my former supervisors Prof. Dr. Yunfei Liu and Prof. Dr. K. Yasumoto for helping me with academic problems even I have finished the master study for a long time. Thanks to my former room mate Haoyuan for sharing nice food and interesting stories with me, also for helping me to move into a studio. You help me a lot! Chunyan, it seems that you always know what I do not know, and explain them patiently to me, thank you. I also thank teachers from TUDelft Sports centre: Yadira (Zumba), Cindy (Pilates), and Roos (BBB and Body-Power) for their courses. It is a good way to release the anxiety after work, also keep fit. And I enjoy them a lot.

Last but not least, my family. I am deeply grateful to my dear parents for their endless love and support. This thesis is dedicated to you. My dear Dad, you always supported me unconditionally and gave me better life and education. You always pushed me to go forward bravely and encouraged me to study harder. Without you, my life would have been totally different. I will always miss you. Whatever we are, you and I will always collide (无论如何, 我们终会相遇). Mom, thank you for bringing me to life, raising me, supporting me and teaching me to face difficulties and making me strong. I thank you with all of my heart. Bin, it is my greatest luck to have met you. Without your understanding, tolerance, sacrifice and company, I would not be able to finish this journey. Thank you very much.

Peiwen Meng

A

Derivation of the focal fields of given power with a maximum longitudinal electric component

The purpose of this section is to present closed form expression for the electric field in the lens pupil, which maximizes the longitudinal electric field component at the focal point is larger than any other focused field with the same power. The optimum pupil field is shown as in Eqs. 2.20 and 2.21. It is found to be radially polarized; however, the amplitude is not of doughnut type but increases monotonically with distance to the optical axis in a way that depends on the NA [1–3].

The plane wave expansions of the electromagnetic field at focus are given in Eq. 2.1 in the section 2.2.1 as well as the definition of the polarizations of the plane waves in Eq. 2.2. Here we shall use spherical coordinate system in the reciprocal \mathbf{k} space, therefore the positively orientated orthonormal basis $\hat{\mathbf{k}}$, $\hat{\boldsymbol{\theta}}$ and $\hat{\boldsymbol{\phi}}$ are defined as:

$$\begin{aligned}\hat{\mathbf{k}} &= \sin \theta \cos \phi \hat{\mathbf{x}} + \sin \theta \sin \phi \hat{\mathbf{y}} + \cos \theta \hat{\mathbf{z}}, \\ \hat{\boldsymbol{\theta}} &= \cos \theta \cos \phi \hat{\mathbf{x}} + \cos \theta \sin \phi \hat{\mathbf{y}} - \sin \theta \hat{\mathbf{z}}, \\ \hat{\boldsymbol{\phi}} &= -\sin \phi \hat{\mathbf{x}} + \cos \phi \hat{\mathbf{y}},\end{aligned}\tag{A.1}$$

where $0 \leq \theta \leq \theta_{max}$, $0 \leq \phi \leq 2\pi$ are polar and azimuthal angles, correspondingly. The Jacobian of the transformation of spherical coordinates θ , ϕ into \mathbf{k} components k_x and k_y is written:

$$\begin{pmatrix} \frac{\partial k_x}{\partial \theta} & \frac{\partial k_x}{\partial \phi} \\ \frac{\partial k_y}{\partial \theta} & \frac{\partial k_y}{\partial \phi} \end{pmatrix} = k_0 n \begin{pmatrix} \cos \theta \cos \phi & -\sin \theta \sin \phi \\ \cos \theta \sin \phi & \sin \theta \cos \phi \end{pmatrix},\tag{A.2}$$

and $dk_x dk_y = k_0^2 n^2 \cos \theta \sin \theta d\theta d\phi$. The vector amplitude \mathbf{A} in Eq. 2.3 can also be expressed as:

$$\mathbf{A}(\theta, \phi) = A_\theta(\theta, \phi)\hat{\boldsymbol{\theta}} + A_\phi(\theta, \phi)\hat{\boldsymbol{\phi}}, \quad (\text{A.3})$$

According to the property of orthonormality of the unit vectors:

$$\hat{\mathbf{k}} \times \hat{\boldsymbol{\theta}} = \hat{\boldsymbol{\phi}}, \quad \hat{\boldsymbol{\theta}} \times \hat{\boldsymbol{\phi}} = \hat{\mathbf{k}}, \quad \hat{\boldsymbol{\phi}} \times \hat{\mathbf{k}} = \hat{\boldsymbol{\theta}}, \quad (\text{A.4})$$

then

$$\hat{\mathbf{k}} \times \hat{\mathbf{A}} = k_0 n (-A_\phi \hat{\boldsymbol{\theta}} + A_\theta \hat{\boldsymbol{\phi}}), \quad (\text{A.5})$$

The plane wave expansion in Eq. 2.1 can be written as integrals over the angles θ and ϕ :

$$\begin{aligned} \mathbf{E}^e(\mathbf{r}) &= \frac{n^2}{\lambda_0^2} \int_0^{2\pi} \int_0^{\theta_{max}} (A_\theta \hat{\boldsymbol{\theta}} + A_\phi \hat{\boldsymbol{\phi}}) \sin \theta \cos \theta e^{i\mathbf{k}\cdot\mathbf{r}} d\phi d\theta, \\ \mathbf{H}^e(\mathbf{r}) &= \frac{n^3}{\lambda_0^2} \left(\frac{\epsilon_0}{\mu_0} \right)^{1/2} \int_0^{2\pi} \int_0^{\theta_{max}} (-A_\phi \hat{\boldsymbol{\theta}} + A_\theta \hat{\boldsymbol{\phi}}) \sin \theta \cos \theta e^{i\mathbf{k}\cdot\mathbf{r}} d\phi d\theta, \end{aligned} \quad (\text{A.6})$$

In the optimization, $E_z(\mathbf{0})$ is considered as a functional of A_θ and is given by:

$$E_z(\mathbf{0}) = -\frac{n^2}{\lambda_0^2} \int_0^{2\pi} \int_0^{\theta_{max}} A_\theta(\phi, \theta) \sin^2 \theta \cos \theta d\phi d\theta, \quad (\text{A.7})$$

By using Plancherel's formulas, we can get the total time-averaged power flow in the z direction through a plane $z=\text{const}$ by integrating the the normal component of the vector $\frac{1}{2}\text{Re } \mathbf{S}$ over the plane, where $\mathbf{S} = \mathbf{E} \times \mathbf{H}^*$ represents the complex Poynting vector. The integral of $\text{Re } \mathbf{S}$ can be written as:

$$\begin{aligned} P(A_\theta, A_\phi) &= \int_{-\infty}^{\infty} \int_{-\infty}^{\infty} \frac{1}{2} \text{Re}[\mathbf{E}^e(\mathbf{r}) \times \mathbf{H}^e(\mathbf{r})^*] \cdot \hat{\mathbf{z}} dx dy, \\ &= \frac{n^3}{2\lambda_0^2} \left(\frac{\epsilon_0}{\mu_0} \right)^{1/2} \int_0^{2\pi} \int_0^{\theta_{max}} [|A_\theta(\phi, \theta)|^2 + |A_\phi(\phi, \theta)|^2] \cos^2 \theta \sin \theta d\phi d\theta. \end{aligned} \quad (\text{A.8})$$

$P(A_\theta, A_\phi)$ is called the power flow, which is independent of the plane $z=\text{const}$ and should be in a medium without losses.

The optimization problem is to find the plane wave amplitude $\mathbf{A}(\theta, \phi) = A_\theta(\theta, \phi)\hat{\boldsymbol{\theta}} + A_\phi(\theta, \phi)\hat{\boldsymbol{\phi}}$ for which the amplitude of the longitudinal component of the electric field at the origin is maximum among all fields with the same mean power P_0 flow through a plane $z=\text{const}$ and the same NA, i.e.,

$$\text{maximize : } E_z(\mathbf{0}), \quad \text{under the constraint : } P(A_\theta, A_\phi) = P_0, \quad (\text{A.9})$$

As the the object functional $E_z(\mathbf{0})$ depends linearly on the plane wave amplitudes and the energy constraint functional P is quadratic in these amplitudes, the optimization problem is a classical quadratic problem. Solving Eq. A.9 can be done with the Lagrange multiplier rule,

$$\delta E_z(\mathbf{0}) - \Lambda \delta P = 0, \quad (\text{A.10})$$

where Λ denotes the Lagrange multiplier.

The Lagrange multiplier rule therefore yields a system of linear equations for the optimum plane wave amplitudes. By using this system of equations the optimum plane wave amplitudes can be expressed in the Lagrange multiplier Λ and one can find

$$A_\theta(\theta, \phi) = -\frac{\tan \theta}{\Lambda}, \quad A_\phi(\theta, \phi) = 0, \quad (\text{A.11})$$

The Lagrange multiplier is obtained by substituting Eq. A.11 into the power constraint $P(A_\theta, A_\phi) = P_0$, and this gives

$$\Lambda = \left(\frac{\pi}{P_0} \right)^{1/2} \frac{n^{3/2}}{\lambda_0} \left(\frac{\epsilon_0}{\mu_0} \right)^{1/4} \left(\frac{2}{3} - \cos \theta_{max} + \frac{1}{3} \cos^3 \theta_{max} \right)^{1/2}. \quad (\text{A.12})$$

Eqs. A.11 and A.12 are the same as Eqs. 2.20 and 2.21 except the different notations.

References

- [1] H. P. Urbach and S. F. Pereira, *Field in focus with a maximum longitudinal electric component*, *Phys. Rev. Lett.* **100**, 123904 (2008).
- [2] H. P. Urbach and S. F. Pereira, *Focused fields of given power with maximum electric field components*, *Phys. Rev. A* **79**, 013825 (2009).
- [3] Q. Y. van den Berg, S. F. Pereira, and H. P. Urbach, *Focused fields of given power with maximum longitudinal electric field component inside a substrate*, *J. Opt. Soc. Am. A* **33**, 1010 (2016).

B

LabView program

The purpose of this section is to give a detailed algorithm of controlling the piezo for the scanning process in the experiment.

Require: $(x; y; z) = (0; 0; f)$ \mapsto The piezos are at their rest position and the sample is at focus.

Function Expose $(x; y; z; t)$

Make marker. \mapsto Create a marker point by heavily overexposing start of array.

for $n= 0$ to $(N-1)$ do

for $m= 0$ to $(M-1)$ do

$x = x + n \cdot \Delta x$

$y = y + m \cdot \Delta y$

$t = t + m \cdot \Delta t$

Pause at current location, pulse laser

end for

end for

Return to initial stage position

end Function Expose

C

Full derivation of the reflective far field

This appendix gives a detailed derivation of how to get the far field scattering by a single dipole on a substrate with the stationary phase method. The reflected field is given by

$$\mathbf{G}_r(\mathbf{r}, \mathbf{r}_p) = -\frac{1}{4\pi^2} \int_{-\infty}^{\infty} \int_{-\infty}^{\infty} q(k_x, k_y) e^{if(k_x, k_y)} dk_x dk_y, \quad (\text{C.1})$$

where

$$q(k_x, k_y) = \frac{R(k_{\perp})}{2ik_z}, \quad (\text{C.2})$$

$$f(k_x, k_y) = k_x(x - x_p) + k_y(y - y_p) + k_z(z + z_p), \quad (\text{C.3})$$

where $R(k_{\perp})$ is the reflection coefficient. The integrand in Eq. C.1 will oscillate quickly as function of k_x and k_y , when the observation position \mathbf{r} is far from the dipole \mathbf{r}_p . The point of least fast oscillations (k_{x0}, k_{y0}) , is the one whose phase is stationary, i.e.:

$$\frac{\delta f(k_x, k_y)}{\delta k_x} = \frac{\delta f(k_x, k_y)}{\delta k_y} = 0, \quad (\text{C.4})$$

Solving Eq.C.4 gives the following results for k_{x0} and k_{y0}

$$k_{x0} = k_0 n_1 \frac{x - x_p}{|\mathbf{r} - \mathbf{r}_p|}, \quad (\text{C.5})$$

$$k_{y0} = k_0 n_1 \frac{y - y_p}{|\mathbf{r} - \mathbf{r}_p|}, \quad (\text{C.6})$$

$$|\mathbf{r} - \mathbf{r}_p|^2 = (x - x_p)^2 + (y - y_p)^2 + (z + z_p)^2, \quad (\text{C.7})$$

Due to k_{\perp} becomes

$$k_{\perp} = \sqrt{k_{x0}^2 + k_{y0}^2} = k_0 n_1 \frac{\sqrt{(x - x_p)^2 + (y - y_p)^2}}{|\mathbf{r} - \mathbf{r}_p|}, \quad (\text{C.8})$$

then we have

$$k_z = k_0 n_1 \frac{z + z_p}{|\mathbf{r} - \mathbf{r}_p|}, \quad (\text{C.9})$$

At the point of stationary phase, Eq. C.3 is

$$\begin{aligned} f(k_x, k_y) &= f(k_{x0}, k_{y0}) + \frac{1}{2} a (k_x - k_{x0})^2 \\ &+ \frac{1}{2} b (k_y - k_{y0})^2 + c (k_x - k_{x0})(k_y - k_{y0}) + \dots \end{aligned} \quad (\text{C.10})$$

where the coefficients a , b and c are given by

$$a = \left. \frac{\partial^2 f(k_x, k_y)}{\partial k_x^2} \right|_{k_x=k_{x0}} = -\frac{z + z_p}{k_{z0}} - \frac{k_{x0}^2}{k_{z0}^3} (z + z_p), \quad (\text{C.11})$$

$$b = \left. \frac{\partial^2 f(k_x, k_y)}{\partial k_y^2} \right|_{k_y=k_{y0}} = -\frac{z + z_p}{k_{z0}} - \frac{k_{y0}^2}{k_{z0}^3} (z + z_p), \quad (\text{C.12})$$

$$c = \left. \frac{\partial^2 f(k_x, k_y)}{\partial k_x \partial k_y} \right|_{k_x=k_{x0}, k_y=k_{y0}} = -\frac{k_{x0} k_{y0}}{k_{z0}^3} (z + z_p), \quad (\text{C.13})$$

Substituting Eqs. C.5- C.9 in Eqs. C.11- C.13 results in

$$a = -\frac{|\mathbf{r} - \mathbf{r}_p| [(x - x_p)^2 + (z + z_p)^2]}{k_0 n_1 (z + z_p)^2}, \quad (\text{C.14})$$

$$b = -\frac{|\mathbf{r} - \mathbf{r}_p| [(y - y_p)^2 + (z + z_p)^2]}{k_0 n_1 (z + z_p)^2}, \quad (\text{C.15})$$

$$c = -\frac{|\mathbf{r} - \mathbf{r}_p| (x - x_p)(y - y_p)}{k_0 n_1 (z + z_p)^2}, \quad (\text{C.16})$$

Eq. C.1 can be rewritten as

$$\mathbf{G}_r(\mathbf{r}_{\infty}, \mathbf{r}_p) \approx -\frac{1}{2\pi} \frac{\sigma}{\sqrt{|ab - c^2|}} q(k_{x0}, k_{y0}) e^{if(k_{x0}, k_{y0})}, \quad (\text{C.17})$$

where σ is given by

$$\sigma = \begin{cases} i, & \text{if } a > 0 \text{ and } ab - c^2 > 0, \\ 1, & \text{if } a > 0 \text{ and } ab - c^2 < 0, \\ -i, & \text{if } a < 0 \text{ and } ab - c^2 > 0, \\ 1, & \text{if } a < 0 \text{ and } ab - c^2 < 0, \end{cases} \quad (\text{C.18})$$

and

$$|ab - c^2| = \frac{|\mathbf{r} - \mathbf{r}_p|^4}{k_0^2 n_1^2 (z + z_p)^2}, \quad (\text{C.19})$$

Since Eq. C.11 is always negative and Eq. C.18 is always positive, σ is $-i$. Substituting Eqs. C.2, C.3, C.18 and C.19 in C.17, then we can get

$$\mathbf{G}_r(\mathbf{r}_\infty, \mathbf{r}_p) \approx -R(k_0 n_1 \sin \theta) \frac{1}{4\pi} \frac{e^{ik_0 n_1 |\mathbf{r}_\infty - \mathbf{r}_p|}}{|\mathbf{r}_\infty - \mathbf{r}_p|}, \quad (\text{C.20})$$

where

$$\sin \theta = \frac{\sqrt{(x - x_p)^2 + (y - y_p)^2}}{|\mathbf{r}_\infty - \mathbf{r}_p|}. \quad (\text{C.21})$$

Curriculum Vitæ

Peiwen Meng

28-07-1990 Born in Zhenjiang, China.

Education

- 2008–2012 B.Sc. in Electronic Information Engineering
Nanjing Forestry University, Nanjing, China
- 2012–2015 M.S. in Instrument Science and Technology
Nanjing Forestry University, Nanjing, China
Thesis: Influence of enclosure holes or slots
on electromagnetic shielding effectiveness
Promotor: Prof. dr. Y. Liu and Prof. dr. K. Yasumoto
- 2015–2020 PhD student in Physics
Optics Research Group, Delft University of Technology, The Netherlands
Thesis: Tightly Focused Spot Shaping and its applications
in optical imaging and trapping
Promotor: Prof. dr. H. P. Urbach and Assoc. Prof. dr. S. F. Pereira

Awards

- 2015 Outstanding Master Thesis, NJFU
- 2014 National Postgraduate Student Scholarship, China
- 2014, 2013 Excellent Postgraduate Student Leader Award, NJFU
- 2014, 2013 First-class Scholarship for Postgraduate, NJFU

List of Publications

13. X. Dou, S. F. Pereira, C. Min, Y. Zhang, **P. Meng**, H. P. Urbach, X. Yuan, *Far-field determination of steep side wall angle with polarization-sensitive asymmetric scattering*, *Measurement*, (2020). (Submitted)
12. Z. Man, **P. Meng**, S. Fu, R. E. Burge, H. P. Urbach, X. Yuan, *asurement Nanoscale control over polarization singularities in nonparaxial field*, *Physical Review A*, (2020). (Under review)
11. **P. Meng**, S. F. Pereira, X. Dou, H. P. Urbach, *Superresolution effect due to a thin dielectric slab for imaging with radially polarized light*, *Optics Express* **28(14)**, 20660 (2020).
10. **P. Meng**, H. Pham, S. F. Pereira, H. P. Urbach, *Demonstration of lateral resolution enhancement by focusing amplitude modulated radially polarized light in a confocal imaging system*, *Journal of Optics* **22**, 045605 (2020).
9. D. Kolenov, **P. Meng**, S. F. Pereira, *Highly-sensitive laser focus positioning method with sub-micrometre accuracy using coherent Fourier scatterometry*, *Measurement Science and Technology* **31**, 064007(2020).
8. Z. Man, **P. Meng**, S. Fu, *Creation of complex nano-interferometric field structures*, *Optics Letters* **45(1)**, 37 (2020).
7. **P. Meng**, Z. Man, A. P. Konijnenberg, H. P. Urbach, *Angular momentum properties of arbitrary cylindrical vector vortex beams in tightly focused optical systems*, *Optics Express* **27(24)**, 35336 (2019).
6. **P. Meng**, S. F. Pereira, H. P. Urbach, *Confocal microscopy with a radially polarized focused beam*, *Optics Express* **26(23)**, 29600 (2018).
5. V. Jandieri, **P. Meng**, K. Yasumoto, Y. Liu, *Scattering of light by gratings of metal-coated circular nanocylinders on a dielectric substrate*, *Journal of the Optical Society of America A* **32(7)**, 1384 (2015).
4. F. Wu, K. Luo, C. Huang, W. Wu, **P. Meng**, Y. Liu, E. Kan, *Theoretical understanding of magnetic and electronic structures of Ti3C2 monolayer and its derivatives*, *Solid State Communications* **222**, 9 (2015).
3. F. Wu, K. Luo, Y. Liu, W. Wu, G. Liu, **P. Meng**, E. Kan, *Magnetic and electronic properties of frustrated spin dimer compound K2Fe2B2O7: A first-principles calculation*, *Solid State Communications* **220**, 77 (2015).
2. F. Wu, **P. Meng**, K. Luo, Y. Liu, E. Kan, *Reduction of defect-induced ferromagnetic stability in passivated ZnO nanowires*, *Chinese Physics B* **24(3)**, 037504 (2015).
1. **P. Meng**, K. Yasumoto, Y. Liu, *Surface plasmon resonant scattering in metal-coated dielectric nanocylinders*, *Optics Communications* **332**, 18 (2014).